Title
Nanoparticle Catalysts for Chemical Valorization of Carbon Dioxide

Author
Kim, Dohyung

Publication Date
2018

Nanoparticle Catalysts for Chemical Valorization of Carbon Dioxide

By

Dohyung Kim

A dissertation submitted in partial satisfaction of the

requirements for the degree of

Doctor of Philosophy

in

Engineering – Materials Science and Engineering

in the

Graduate Division

of the

University of California, Berkeley

Committee in charge:

Professor Peidong Yang, Chair
Professor Ting Xu
Professor Omar Yaghi

Spring 2018

Abstract

Nanoparticle Catalysts for Chemical Valorization of Carbon Dioxide

by

Dohyung Kim

Doctor of Philosophy in Engineering – Materials Science and Engineering

University of California, Berkeley

Professor Peidong Yang, Chair

Human activity in the last two centuries that has revolutionized the way of using resources and brought marked improvements in the quality of our lives has now put us in a position to rethink of the many operations that support our society. We are at a stage where the practices of the past and present cannot be continued due to their severe negative impacts, such as the climate change. At the center of those practices lies our heavy reliance on fossil fuels, for harvesting energy and manufacturing chemical products. We need a disruptive technology that can fundamentally change our common practices and poses minimal threats to our society.

Electrochemical (or photochemical) conversion of carbon dioxide to value-added products is one of the technologies with a potential to make the change. It targets the use of atmospheric carbon dioxide as reagents to generate valuable carbon products, such as hydrocarbons or multicarbon oxygenates, which can be utilized for various purposes. Eventually, it allows creating an artificial carbon cycle, just like the one that nature established, which the carbon compounds that we use are constantly recycled through the system by renewable energy inputs such as solar or wind. In order to realize its potentials, a high-performance catalyst material that can efficiently convert carbon dioxide has to be developed. In this regard, the unique catalytic properties of nanoparticles have brought significant advancements in the field.

Here, numerous structural factors of nanoparticles that are linked to their CO_2 electrocatalytic performance are discussed. With the notion that these factors span over large length scales, studies have been conducted focusing on not only the properties originating from the atomic scale but structural considerations at the micro- or macroscopic scales. The latter is related to the goal of establishing a complete system capable of CO_2 valorization by renewable energy inputs. In addition, a critical factor often neglected, the structural dynamics of nanoparticles have been studied which will shed light into the ways of identifying the true catalytic origin of materials and developing catalysts that will naturally transform into optimized structures during operation.

Bimetallic systems offer a great amount of structural diversity by their change of composition and the physical arrangements of both elements. With regards to CO_2 electroreduction, gold-copper bimetallic nanoparticles were explored as catalysts by changing the composition and the atomic orderedness. The composition-dependent activity of Au-Cu nanoparticles showed that the shift in the composition brought modifications to their surface electronic structure that dictated the intermediate binding strength. Furthermore, evidence of geometric effects to intermediate stabilization could be observed as well. However, even with a fixed composition, it was found that the atomic ordering transformation could enable significant shifts in the catalytic behavior (*i.e.* H_2 active to CO active). Investigations involving atomic resolution imaging and X-ray absorption showed that atomic ordering of Au-Cu systems induced a few-atoms thick gold layer on the surface which was responsible for the NPs becoming active for CO_2 reduction.

Eventually, catalysts developed for CO_2 reduction need to be coupled with other materials or systems to enable CO_2 valorization using renewable energy sources. With solar photons being one of the most attractive options as a renewable energy input, two conceptually different ways of utilizing nanoparticles for light-driven CO_2 reduction have been studied. The first method involves utilizing nanoparticles as CO_2 electrocatalysts and interfacing them with light-absorbing platforms. In this approach, often the issue is how to enable an efficient coupling of the two different materials without compromising their inherent capabilities. Using Si NWs as the light-absorber, we found that the one-dimensional geometry of the NWs guided the colloidal NP assembly process that allowed uniform and controlled assembly of NPs. This integration process led to performance improvements in light-driven CO_2 conversion compared to what can be achieved in other platforms and showed the potential of Si NWs to act as a general platform for interfacing a wide range of electrocatalysts.

The other approach involved the use of nanoparticles as catalytic enhancers. Photoactive rhenium complexes were used as visible light-absorbing CO_2 catalysts. These complexes were covalently attached within a metal-organic framework (MOF) to understand how the molecular environment within the MOF`s pores can affect their catalytic behavior. With the optimized configuration of the MOF structure, Re-complex containing MOFs were coated on silver nanocubes where MOFs spatially concentrated the photoactive complexes in the vicinity of the plasmon-enhanced near surface electric fields of silver nanocubes. The Ag-MOF nanoparticle structure exhibited maximum 7-fold enhancements in catalytic turnover with stability demonstrated for 48 hours. The success of this approach clearly demonstrates the catalytic potential of combining various inorganic and organic materials with each component having discrete functionalities.

An important aspect of nanomaterials is there tendency to readily transform under various conditions due to their increased energetics. This is particularly important for catalytic applications as the nanoscale catalysts can restructure during catalysis, which can make the structure-activity correlation elusive and also lead to changes in activity over time.

This idea has been recently considered for CO_2 electrocatalysts. Using spherical copper nanoparticles as the starting material, structural transformation to cuboidal nanoparticles by their fusion and redistribution was observed under catalytic conditions. This transition led to significant improvements in the multicarbon formation activity from CO_2. The *in-situ* formed catalyst exhibited record low overpotentials for achieving over 50% of C_{2-3} products faradaic efficiency, clearly demonstrating the importance of understanding the materials dynamics under electrochemical conditions. In addition, apart from CO_2 electrocatalysis, a rare phenomenon of disappearing copper nanoparticles on amorphous silica supports under ambient conditions was observed. Structural investigations probing the elemental environment of copper atoms showed that they were migrating into the silica support surrounded by oxygen and silicon atoms. This observation opens up many questions regarding the nature of active sites for oxide-supported metal nanoparticles in catalysis.

Overall, the works discussed here illustrate the structural complexity of catalytic systems. Acknowledging their complexity and having a systematic understanding of its factors will provide the fundamental basis for developing efficient catalyst materials and systems for CO_2 electroreduction. With all these taken into consideration, we may see an expansion of the potentials of nanoparticles used for CO_2 conversion, to the levels where any type of a desired product can be readily and selectively gained.

To my family for their love and unwavering support

Table of Contents

List of Figures

List of Tables

Acknowledgments

First and foremost, I would like to thank my advisor Prof. Peidong Yang for all the support he has given that led me to this point. I have experienced significant growth as a scientific researcher in various aspects through the interactions with him. I can say for certain that the decision to come to UC Berkeley and his group was one of my best choices in life.

My accomplishments in Berkeley would not have been possible without the help of the Yang group members. I would like to thank my dear friend Nigel Becknell for the times spent together in the group. I was very fortunate to join the group in the same year as him and work closely together throughout our years here. I also owe thanks to my peers who joined together: Kelsey Sakimoto, Joaquin Resasco, Dandan Zhang, Fan Cui, and Yude Su. Members in the group who have closely worked with me in a number of works certainly deserve much thanks, who are Yifan Li, Chris Kley, Mike Ross, Yi Yu, Qiao Kong, Sunmoon Yu, Sheena Louisia, Chenlu Xie, Chong Liu, Adam Slabon, Dachao Hong, Yoonkook Son, Zhiqiang Niu, Andrew Wong, Nick Kornienko, Tom Lin, Cindy Zheng, and Jesika Barmanbek. Others in the group, past and present, have influenced my times at Berkeley and I would like to thank them as well, who are Jongwoo Lim, Sarah Brittman, Chris Hahn, Ruoxue Yan, Anthony Fu, Woochul Lee, Woong Kim, and Chen Chen.

I would like to also express my gratitude to the other PIs that I have interacted throughout my PhD for their support of my works, Prof. Omar Yaghi, Prof. Jens Nørskov, and Prof. Chris Chang. Also, thanks to my collaborators in their groups: Kyungmin Choi, Bunyarat Rungtaweevoranit, Chris Trickett, Reza Karamad, Karen Chan, and Zhi Cao.

For all the great times I had as a Molecular Foundry user for 5 years, I would like to thank the staff scientists, Virginia Altoe and Shaul Aloni, for their help that allowed me to make great discoveries.

Sincere thanks to Samsung Scholarship for its support during my PhD. It was a great honor to be one of the Samsung Scholars.

Finally, a big thank you to my parents, Daehyun Kim and Piljae Lee, who have trusted me wholeheartedly in every part of the decision I made throughout my life. They have given me full support for the paths I`ve taken and it was their love and commitment that was essential to all of my successes. I also would like to take this opportunity to thank my younger brother, Junhyung Kim, for his continued support of my dreams.

Chapter 1

Introduction

Reproduced in part with permission from "Kim, D., Sakimoto, K. K., Hong, D. & Yang, P. Artificial Photosynthesis for Sustainable Fuel and Chemical Production. Angew. Chemie Int. Ed. ***54,*** *3259–3266 (2015)." Copyright 2015 WILEY-VCH Verlag GmbH & Co. KGaA, Weinheim.*

1.1. Artificial photosynthesis for a sustainable future

In every aspect of our lives, we rely on fuels and chemicals, whose usefulness is typically exhausted once consumed. With the growing population and technological advances, this unidirectional flow of energy and matter has grown significantly to the extent that we face the threat of a dearth of supply and rising costs. For instance, energy consumption is expected to rise by 56 % worldwide by 2040 with close to 80 % provided by fossil fuels.[1] The growing demand for fertilizers caused by the increased rate of food consumption of our rising population has necessitated the development of alternative routes to produce ammonia.[2] Considering that our average standard of living is likely to rise continuously, we must seek a drastic change in this consumption-oriented trend to maintain the sustainability of our society. The challenges we face require an efficient method to convert raw materials into useful fuels and chemicals, to make the flow of energy and matter bidirectional, and help maintain a balance between production and consumption.

For the efficient and sustainable production of fuels and chemicals, the method to be developed has to utilize energy and resources that are naturally abundant and easily renewable. Artificial photosynthesis uses solar power, which can provide up to 10^5 TW of energy, to convert raw materials like water and CO_2 to useful chemicals, e.g., H_2, CO, and hydrocarbons.[3] Therefore, the success of this approach relies on two aspects; the efficient utilization of solar power and the enhancement of the catalytic conversion of water and carbon dioxide to fuels and chemicals. These two main challenges were the focus of many ongoing scientific efforts and will have to be solved in the near future for the practical application of artificial photosynthesis. If successful, the technology of artificial photosynthesis will be able to fundamentally transform the current economy of fossil fuels into a sustainable economy of "photons".

Artificial photosynthesis, as its name suggests, originated from the desire to mimic nature's unique arsenal of photosynthetic processes to store energy from sunlight in high-energy chemical bonds. Ever since its first demonstration,[4] there have been numerous efforts to split water to H_2 and O_2 with high conversion efficiency.[3] More recently, due to the hope of renewably generating carbon fuels, efforts to reduce CO_2 have gained much attention. The production of carbon-based fuels from CO_2 can help to alleviate the shortage of fossil fuels and reduce our overall contribution to atmospheric CO_2.[5] The development of carbon-based fuels, or so-called "drop-in fuels", also allows us to use renewable sources of energy without the need to modify our current energy infrastructure, alleviating some of the financial and logistical impediments to a fully renewable energy economy. In addition, some of the products generated from CO_2 reduction, such as carbon monoxide and ethylene, are basic synthetic components for a large number of fine chemicals.[6] Artificial photosynthesis has the potential to lie at the center of all chemical reactions implemented in our society and its success will determine whether we can achieve sustainable chemistry for future generations.

Since artificial photosynthesis is an integrated system, which consists of a light harvesting part and a catalytic conversion part, it is important to maximize the performance of each unit and to design a combined system with optimum efficiency, based on a thorough understanding of each component and the interactions between them. There has been much progress in its constituent parts such as light harvesting, charge transport, and catalytic conversion of water. However, carbon dioxide reduction, which is expected to become an essential component of artificial photosynthesis, has proven to be difficult without much progress. It is a much more complex and difficult process compared to its relevant competitor, the hydrogen evolution reaction (HER). First of all, though thermodynamically more favorable compared to HER, CO_2 reduction requires a large overpotential to drive the reaction at a sufficient rate.[7] In addition, its wide range of products and large number of different intermediate species makes the analysis and development of efficient catalysts with high selectivity difficult.[8,9] Below, we discuss in detail the fundamental aspects of carbon dioxide electrochemical reduction in aqueous media.

1.2. Electrochemical reduction of carbon dioxide

1.2.1. Fundamentals of electrochemical CO_2 reduction

Electrochemical reduction of carbon dioxide has the potential to produce a wide range of products, from the simple products such as carbon monoxide or formate to more complex molecules, such as *n*-propanol. Up to now, more than 16 products have been identified[8,9] and they can be categorized depending on the number of carbon-carbon bonds or the number of electron transfers required to produce them (Figure 1.1). The most profoundly studied products are the C_1 compounds,[10] in terms of acquiring the capability to produce them and gaining the understanding behind the reactions involved. The difficulty associated with forming C-C bonds by electrochemical methods has prevented much progress for other products. Facilitating multiple electron transfers (beyond two electrons) along the reaction pathway poses another difficulty, as it requires optimizing the interactions of a large number of intermediates along the reaction pathway.[11] Nonetheless, there have been some progress in forming multicarbon ($C_{2\text{-}3}$) products,[10,12,13] such as ethylene and ethanol, and there are still considerable amount of research efforts to better elucidate the mechanistic pathways to these products.

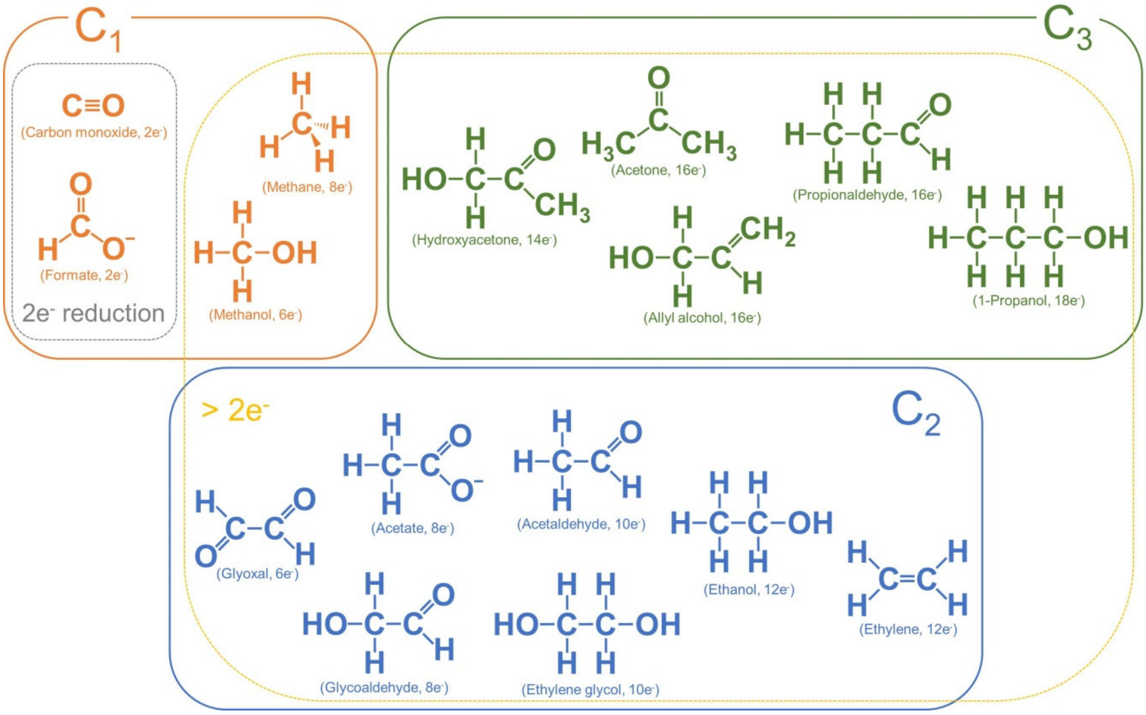

Figure 1.1. Various products generated from electrochemical reduction of carbon dioxide in aqueous media. Electron numbers in the parenthesis indicate the number of electrons required to generate a certain product from CO_2.

In order to produce any useful products from carbon dioxide, the energetic requirements for its conversion to the product molecules need to be understood. Table 1.1 lists the standard reduction potentials of the products. Using the reversible hydrogen electrode (RHE) as a reference, which determines the energy required for protons being reduced to hydrogen gas, the standard reduction potentials of most products lie close to 0 V (vs. RHE, unless otherwise stated). To be more precise, the majority of them are actually above 0 V, which means that the energy needed to convert CO_2 to these products should be less than that required for H_2 formation. Considering the vast amount of previous research efforts in water electrolysis,[14] electrochemical reduction of carbon dioxide seems not only desirable but also technically feasible.

C_1				C_2			
Carbon monoxide	Formate	Methanol	Methane	Glyoxal	Glycoaldehyde	Acetate	Acetaldehyde
-0.11 V	-0.02 V	0.03 V	0.17 V	-0.16 V	-0.03 V	0.14 V	0.05 V

C_2			C_3				
Ethylene glycol	Ethanol	Ethylene	Hydroxyacetone	Acetone	Allyl alcohol	Propionaldehyde	1-Propanol
0.20 V	0.08 V	0.07 V	0.46 V	0.10 V	0.05 V	0.09 V	0.10 V

Table 1.1. Standard reduction potentials of products derived from electrochemical reduction of carbon dioxide. Potentials are referenced to the reversible hydrogen electrode (*i.e.* V vs. RHE).

However, most often, the potentials applied to generate these products are far more negative than their standard reduction potentials. Overpotentials, which is the additional amount of negative bias (for reduction reactions) applied beyond the standard reduction potential, have been more than a couple hundred millivolts to almost a volt just to see the onset of a certain product formation.[8,10,13] It clearly implies that there are large kinetic barriers that need to be overcome for the electrochemical CO_2 transformation. Moreover, not only the sluggish reaction kinetics limit the energy efficiency of the reaction, but it allows the H_2 gas formation from reduction of water to take place more readily as a competing reaction.[8] This eventually results in H_2 consuming for a large fraction of the charge being passed to the electrodes. While there have been some efforts to replace water with other non-aqueous media that also have higher capacity for dissolved CO_2 concentration,[8] the requirement of proton supply to the carbon dioxide transformation pathway makes the H_2 forming side reaction inevitable.

Understanding the reaction pathways is critical in overcoming the kinetic reaction barriers and avoiding the competing H_2 evolution. Moreover, it will provide the means to control the formation of various CO_2 reduced products being generated simultaneously, so that a certain desired product can be gained selectively. While the mechanisms are still being studied, there is a consensus on certain pathways and intermediates that are considered important. Figures 1.2-1.4 illustrate the various pathways involved for converting CO_2 to C_1 and C_2 products. So far, the mechanistic pathways to C_3 products are not well known. A characteristic feature is that the main interaction between the intermediates and a catalyst is based on the binding between the carbon and surface atoms, which results in certain restrictions for controlling intermediate stability as later discussed below.

The pathways to two electron C_1 products (carbon monoxide and formate) are better understood than other products involving multielectron transfers (> $2e^-$) and the formation of C-C bonds (Fig. 1.1). Figure 1.2a shows the pathway to CO formation. The first intermediate suggested is the CO_2^- radical ion formed by a single electron transfer (ET) to CO_2. The sluggish reaction kinetics for CO_2 reduction (and the requirement of high overpotentials) are considered due to this first step generally involved that has a standard reduction potential of -1.9 V vs. NHE (Normal hydrogen electrode).[8] While this may be an equilibrium potential between CO_2 and $CO_2^{\bullet -}$, it illustrates the difficulty in forming $^*CO_2^{\bullet -}$ which is an adsorbed intermediate. Electrokinetic studies have also suggested the $^*CO_2^{\bullet -}$ formation as a rate determining step (RDS) for CO_2-to-CO conversion. Polycrystalline foils of gold and silver, known to be active for CO formation, have exhibited Tafel slopes of ~120mV/dec, which indicates a single electron transfer RDS.[15–19] Therefore, having a catalytic surface that can better stabilize $^*CO_2^{\bullet -}$ would facilitate the reaction moving forward and the subsequent electron and proton transfers would lead to *CO that can readily desorb as a product.

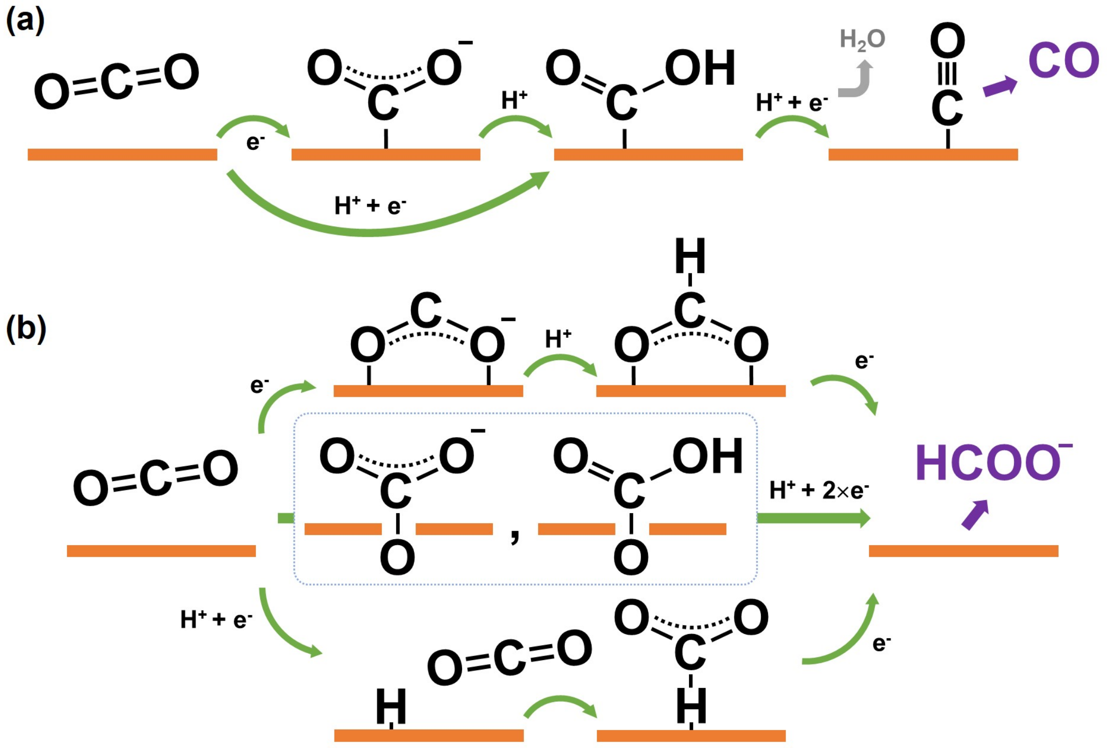

Figure 1.2. Reaction pathways to (a) CO and (b) $HCOO^-$ formation. The intermediates shown inside the blue dotted box are the ones proposed to exist on oxidized metal surfaces acting as a catalyst for formate.

However, there have been reports that suggest a different first step reaction in the pathway to CO.[20,21] The first elementary reaction proposed for CO production on silver surfaces is the concerted-proton electron transfer (CPET) to CO_2 to directly form *COOH.[20] Increased CO formation rates on bulk Ag surfaces by the increased concentration of bicarbonate (HCO_3^-), which can act as a proton donor, supports the proposed step. In contrast, it has been shown that CO formation rates on polycrystalline gold surfaces are not affected by the proton donor concentration.[22,23] Moreover, CPET for CO_2-to-*COOH as a RDS still results in a Tafel slope of 118mV/dec.[16,19,20] A recent study using an operando IR spectroscopic technique on Ag films has shown surface bound intermediates of COOH at low overpotential regions further supporting the CPET pathway to CO.[21] $*CO_2^{\bullet-}$ was observed at more negative potentials suggesting the accessibility of the rate determining ET pathway dependent on the potential applied. Therefore, it may be possible that the reaction mechanisms for CO_2-to-CO conversion differ based on the type of surface used.

Formate producing pathway is more complex,[24] while it is considered distinct from the CO_2-to-CO mechanism. In contrast to the CO forming pathway, carbon dioxide is suggested to bind to the catalyst surface through oxygen atoms (Fig. 1.2b). It was shown theoretically that there is a strong correlation between the $HCOO^-$ activity and the OCHO binding energy to a catalyst surface, instead of that of the COOH.[25,26] Moreover, Tafel slopes on tin foils suggests a chemical rate-determining step (most likely protonation) after a reversible single electron transfer.[27] This may mean that the proton (PT) and electron transfer (ET) steps are separated, with the first ET occurring to form a $*OCO^{\bullet-}$.

But the necessity of surface oxides for formate production[27] and only the partial reduction of the oxidized metal at the catalytically relevant potentials[28,29] suggest a different mechanism. *In situ* attenuated total reflectance infrared spectroscopy (ATR-IR) on tin electrodes have identified tin-carbonate species as an active intermediate for formate production.[29] Spectroscopic observation of metal-carbonate species on some of the *p*-block elements, such as tin and indium,[29–31] rather suggests an alternative mechanism for CO_2 binding to produce formate, where CO_2 binds to the surface through an oxygen atom originating from the surface (Fig. 1.2b).

It seems that not all *p*-block metals behave identical for CO_2 conversion to formate. Formate activity measured on oxide-derived Pb supports a reaction pathway of which the RDS is the first ET to form $*CO_2^{\bullet-}$.[32] Moreover, it is proposed that the metastable Pb oxides are the active species for CO_2 reduction while being inactive for H_2 evolution, which accounts for the significant suppression of the H_2 activity obtained from oxide-derived Pb. However, the catalytic role of metastable Pb oxides is ambiguous. Metastable Pb oxides have been observed during in-situ ATR-IR.[31] However, the lack of metal-carbonate signals on Pb, in contrast to Sn and In, suggests a different mechanism to the production of formate that may not involve Pb oxides. Moreover, because of the enhanced formate production on both types of Pb surfaces, which are the oxide-etched and anodized, the catalytic roles of metallic sites and the metastable oxides in Pb seem to need further investigation. In depth study on bismuth surfaces is required as well, where so far metallic bismuth sites are proposed to be active for formate production.[31]

Outside the *p*-block metals, palladium is often considered as an element useful for $HCOO^-$ production. However, it is also well utilized for CO formation and the relevant potential regions for the production of each are clearly separated. It is due to the fact that the hydrogen absorption properties of Pd make it unique for formate production,[33] allowing it to generate formate very close to its thermodynamic equilibrium potential with unit selectivity.[34] Electrohydrogenation mechanism is proposed for Pd where the surface hydride (PdH) interacts with CO_2 leading to the bond formation between H and C (Fig. 1.2b). While other possibilities cannot be ruled out, this mechanism is suggested based upon the catalytic behavior of palladium hydrides formed from H_2 gas to chemically hydrogenate CO_2.[34]

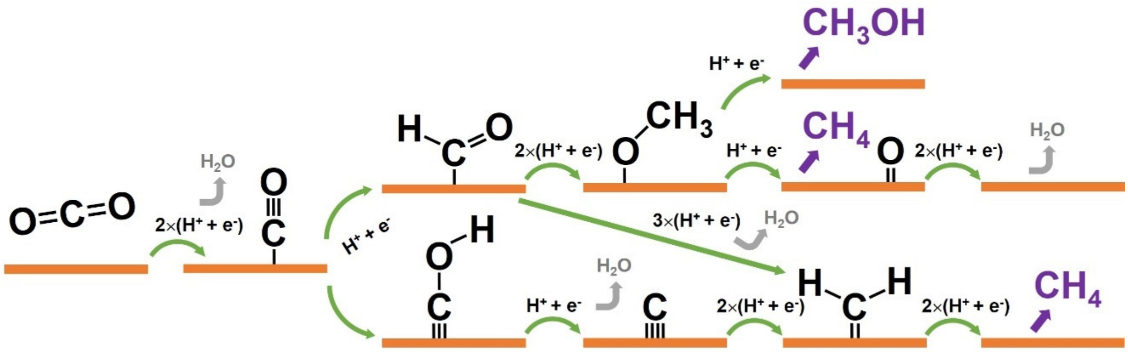

Figure 1.3. Reaction pathways to methane and methanol formation.

Among the C_1 products, production of methane is less understood due to the fact that it requires 8 electron and proton transfers with a large number of individual reaction steps (Fig. 1.3). While it is widely accepted that the CH_4 is produced from an adsorbed CO intermediate,[13] the mechanistic pathways down the *CO is less clear. Understanding the CH_4 formation has largely been driven by theory,[35–39] which have suggested a few possible reaction mechanisms and tried to explain the CH_4 activity trend found for various transition metals.[40] Elementary steps have been studied on model Cu surfaces since copper is the only known element that can produce appreciable amounts of methane.[8,41]

The main question is at which stage does the oxygen dissociate from *CO to be left with only C-H bonds. This question is closely related to the first protonation pathway to the adsorbed carbonyl (Fig. 1.3). Density functional theory calculation performed on a model Cu surface has predicted a pathway that involves a *CHO intermediate.[39] From the adsorbed formyl, subsequent proton and electron transfers occur on the carbon atom to form a methoxy (*OCH_3) intermediate and dissociation of the oxygen atom occurs together with the final step of CH_4 formation. Early experimental works have also suggested *CHO as a key intermediate from the observation of electrochemical conversion of formaldehyde to methane.[38,42,43] However, methanol is the dominant product for formaldehyde reduction on copper surfaces and methanol (as a methoxy intermediate) cannot be further electrochemically reduced to methane.[38] In addition, CO_2 electroreduction on copper exhibits negligible amounts of methanol as a product.[9] All of these observations suggest that a different type of intermediate from *CHO should be present along the pathway to methane.

The other possible configuration that could result from protonating an adsorbed carbonyl is the *COH. By considering the kinetics of each elementary step, a high barrier for $*OCH_3$ to CH_4 was identified which should favor methanol formation from $*OCH_3$.[37] Instead, *CO to *COH is considered as the first step to CH_4 which subsequently produces *C and $*CH_2$ along the reaction pathway (Fig. 1.3).[37,43] Therefore, a distinction could be made between the two pathways for methanol (involving *CHO) and methane (*COH). Furthermore, it was shown that the energetic barrier to a transition state leading to *COH was much lower to that of *CHO which could explain the high selectivity to methane over methanol on copper surfaces.[37]

One possibility that should not be neglected is the formyl (*CHO, or formaldehyde (HCHO)) to carbene ($*CH_2$) transition.[38,42,43] While electroreduction of formaldehyde mostly results in methanol, small amounts of methane have been observed.[38] Therefore, a pathway involving *CHO to CH_4 may exist[35] and occur simultaneously with the *COH pathway during electrochemical reduction of CO_2 (Fig. 1.3). Mechanistic studies have supported this idea by suggesting the formation of *CHOH and the subsequent release of water to lead to $*CH_2$ by multiple protonation steps.[35,36]

Understanding how C-C bonds form is of critical importance in electroreduction of CO_2 to facilitate the formation of multicarbon products. Among these products, ethylene is by far the most well studied product as it can reach up to reasonably high faradaic efficiency (FE) of 40 ~ 50% in certain materials.[44–46] Similar to methane, mechanistic studies for CO_2 to ethylene conversion have been conducted using copper surfaces because of their unique capability to allow C_2-C_3 product formation which is absent in most of the other materials.[8]

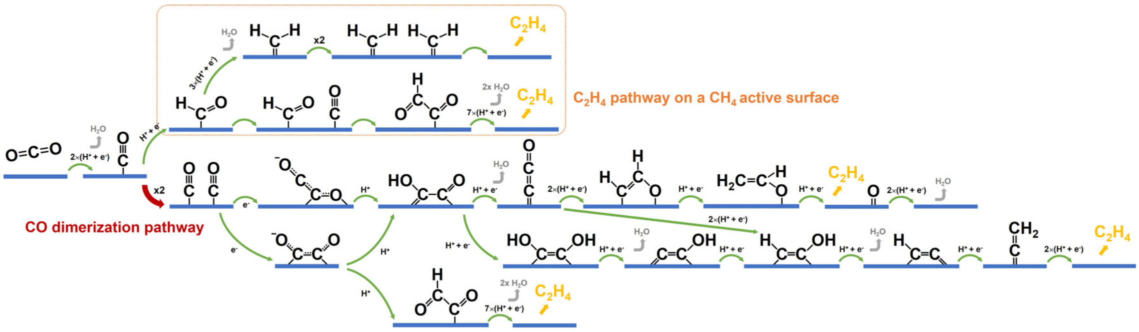

Figure 1.4. Reaction pathways to ethylene formation.

As shown in Figure 1.4, earlier studies that have observed the C_2H_4 formation on copper electrodes have proposed reaction schemes that involve the coupling of carbenes (*CH_2), which have also been suggested as an intermediate for CH_4.[43,47,48] The same dimerization reaction was considered for the reduction of carbon monoxide (CO) to C_2H_4 on copper as well.[49] However, an alternate C-C bond formation pathway by the dimerization of *CO has also been proposed.[7] It was based on a number of experimental observations, such as the difference in the Tafel behavior of CH_4 and C_2H_4 and the C_2H_4 formation occurring at more positive bias compared to that for CH_4, suggesting a different intermediate from *CH_2 that leads to C_2H_4. By the electrokinetic studies indicating a single electron transfer RDS without any pH dependence, electron transfer coupled CO dimerization to *$C_2O_2^-$ was proposed (Fig. 1.4).[7]

Experimental works of electrochemically reducing carbon monoxide on various types of copper surfaces have supported the existence of both pathways. By directly reducing CO, which is a major intermediate for CO_2 reduction to hydrocarbons, on single crystal copper surfaces of (111) and (100), it was shown that two separate pathways exist for C_2H_4.[50] The catalytic pathway to C_2H_4 observed for both surfaces seemed to share a common intermediate with that to CH_4. However, an additional pathway existed for Cu(100) at less negative potentials with high selectivity for C_2H_4/CH_4. This pathway was suggested to be associated with the CO dimerization mechanism. Furthermore, CO reduction experiments on a Cu(110) surface which resulted in a similar activity trend as observed for Cu(111) confirmed that the CO dimerization pathway only exists for Cu(100) type surfaces.[51]

Theoretical studies have supported the CO dimerization pathway. Using the computational hydrogen electrode model to consider the thermodynamic stability of various intermediates,[52] *COCOH was identified as a stable intermediate after CO dimerization. Furthermore, it was shown that this ($H^+ + e^-$) transfer step is decoupled with a RDS of a single ET to *CO + *CO (or CO(g)) to form *$C_2O_2^-$. The stable adsorption geometry of *$C_2O_2^-$ was found in a way that carbon and oxygen atoms bind to the copper surface in a bridging mode (Fig. 1.4). Along the reaction pathway to C_2H_4, intermediates *OCH_2CH_2 and *$OCHCH_2$ have been suggested in the later stages which matches well with the experimental observation of ethylene oxide reduction to ethylene on copper surfaces.[38,51,52] Based on the experimental and theoretical results, mechanistic pathway to C_2H_4 was proposed as shown in Fig. 1.4, with the final step being C_2H_4 dissociated from oxygen bound to the surface.[13,52]

Recently, a more rigorous theoretical approach, with multiple layers of the solvent to better describe the solid-electrolyte interface, was applied to CO reduction on Cu(100) by using ab initio molecular metadynamics simulations (AIMμD).[35] The pathway proposed in the work contains *$C_2O_2^-$ bound to the surface by two carbon atoms and also other intermediates in the same manner throughout the reaction, where both oxygens dissociate early during the process (Fig. 1.4). The previously considered *CCO intermediate[52] was suggested to contribute minorly in C_2H_4 formation by being reduced to *CHCOH.

An alternative pathway after *CO dimerization has been proposed as well. It mainly differs by the protonation site on a *$C_2O_2^-$ dimer to result in a *COCHO as shown in Fig. 1.4.[53–55] The likelihood of *COCHO formation over *COCOH has been supported by the higher stability of *COCHO estimated by theory and the formation glyoxal observed as a minor product for CO_2 electroreduction.[55] Furthermore, instead of the *CH_2, *CHO is suggested as the shared intermediate for both CH_4 and C_2H_4 so that C_2H_4 formation still follows through the pathway involving *COCHO by the interaction of *CO and *CHO in the other pathway mentioned above (Fig. 1.4).[35,54,55]

While most of the understandings for C_2H_4 formation have been developed by theory, spectroscopic methods can support the proposed mechanisms by identifying the intermediates. A recent work using *in situ* Fourier transform infrared spectroscopy (FTIR) for CO reduction on copper surfaces has detected *COCOH as a subsequent intermediate formed by protonation of the *$C_2O_2^-$.[56] Still, a lot of questions remain unsolved for the C-C coupling and the multicarbon product formation in CO_2 electroreduction and further investigations are necessary to develop efficient systems that can realize the full potential of CO_2 valorization by electrochemical methods.

1.2.2. Materials for CO_2 electrocatalysis

Various materials have been tested as electrocatalysts for CO_2 reduction. A broad distinction can be made by the state of the catalysts used which are the homogeneous and heterogeneous catalysts. There have been much research efforts to utilize metal containing molecular complexes as homogeneous CO_2 electrocatalysts.[57] More recently, owing to the advances in nanomaterial synthesis, various kinds of new heterogeneous CO_2 electrocatalysts have appeared.[10] Here, we focus on the materials used for heterogeneous CO_2 electrocatalysis.

The classification of electrocatalysts can be made by the products formed.[8,58] A large number of metal types has been tested and among them, copper is the only element capable of generating useful amount of products in need of more than two electron transfers ($> 2e^-$), such as the hydrocarbons and multicarbon oxygenates. Some studies have shown that other metals can form these complex products, albeit in trace amounts.[40] Thus, other metals are usually categorized based on their major CO_2 reduced products, either CO or formate. CO formation is favored on metals such as gold and silver, while formate production has been largely observed on metals like lead, tin and bismuth. For metals traditionally well explored for H_2 evolution, such as nickel or platinum, H_2 formation dominates even under CO_2 reduction conditions, making them essentially not much useful as CO_2 electrocatalysts.

The CO_2 reduction activity trend observed among various metals has been explained by their characteristic interaction strength towards the CO_2 reduction intermediates. Specifically, the binding energy of CO (or the energetic stability of *CO, where * is the active site) to the surface is used as a guide to interpret the catalytic activity observed.[59–61] It has been explained that metals such as gold or silver that bind CO weakly favor CO as a product, while metals such as platinum or nickel that bind CO strongly is poisoned by the bound CO and mostly generates H_2 gas. Copper is unique in terms of having the optimum binding strength for *CO which allows further electron and proton transfer steps to produce higher order products. A thorough analysis of the reaction products observed from transition metal surfaces could also correlate the methane/methanol formation activity to their CO binding strength.[40] Metals with stronger CO binding (*i.e.* Cu, Ni, Pt, and Fe) were shown to exhibit more positive onset potentials for both products compared to that of the metals with weak CO binding (*i.e.* Au, Ag, and Zn). Though the methane/methanol faradaic efficiency may be low on those strong CO binding metals besides copper due to the competing HER, the work has shown that CO binding strength is an important parameter to consider in CO_2 electroreduction.

For multielectron reactions that involve a larger number of intermediates, the binding energy of each intermediate also needs to be considered to better understand and manipulate the reaction pathway. The ideal case would be a complete control of the interaction strength for each intermediate so that the entire reaction pathway has negligible energy barriers and is mostly comprised of energetically downhill pathways. However, this is not easy to achieve on a catalytic surface composed of a single metallic element due to what is so called the Scaling relation.[59,60] It is about the linear scaling trend observed for binding energies of a large pool of intermediates that share a common surface binding motif. For instance, a metal surface with strong affinity for a CO adsorbate also has strong interactions (and higher binding energies) for *COOH and *CHO, though their absolute strengths could differ. With this constraint, it is very difficult for a single elemental surface to have the optimum interaction strength for all the intermediates observed along the reaction pathway, where, for some intermediates, a weaker interaction may be desirable.

In order to break away from the scaling relationship and add more degrees of freedom to the energetics involved in a catalytic reaction, additional modes of binding need to be introduced on the catalyst surface to either stabilize or destabilize certain intermediates. Decoupling of the binding energies of multiple intermediates in this manner is feasible, as certain intermediates have the potential of allowing additional binding modes due to their molecular configurations, such as having an oxygen atom situated close to the catalyst surface. Therefore, catalyst modification strategies such as metal alloying and surface functionalization using molecular promoters have been proposed that facilitates specific interactions to certain intermediates.[59]

1.2.3. Electrochemical environment factors critical to CO_2 electrocatalysis

Electrochemical environment factors play significant roles in CO_2 electroconversion. While CO_2 reduction studies have been mostly conducted in aqueous electrolyte solutions around neutral pH,[8] there have been some efforts to utilize non-aqueous solvents. The main advantages of using non-aqueous electrolytes are the increased solubility of dissolved carbon dioxide and the suppression of H_2 evolution.[8] For instance, CO_2 saturation levels in acetonitrile and dimethylformamide are 279mM and 199mM, respectively. Compared against the CO_2 solubility in water (33mM), these solvents have about 6 to 8 times the capacity for CO_2 uptake. The characteristic activity and product distribution of electrocatalysts significantly differ from their catalytic behaviors in aqueous media and products such as CO, formate and oxalic acid have been observed on various metal electrodes in organic solvents.[8]

When utilizing aqueous electrolytes, CO_2 equilibrium in water and the resulting buffering capability need to be considered. Dissolved carbon dioxide establishes an equilibrium between carbonic acid, bicarbonate, and carbonate as follows,[8]

$$\mathrm{CO}_{2\,(aq)} + H_2O \leftrightarrow H_2CO_3 \leftrightarrow H^+ + HCO_3^- \; (pK_a = 6.35)$$
$$HCO_3^- \leftrightarrow H^+ + CO_3^{2-} \; (pK_a = 10.33)$$

Carbonic acid (H_2CO_3) formed from dissolved carbon dioxide deprotonates to bicarbonate with a pK_a of 6.35. Then, bicarbonate equilibrates with carbonate with a pK_a of 10.33. The pH values of a CO_2 (1atm) saturated bicarbonate electrolyte range from 6 to 8 depending on the bicarbonate concentration.[7]

However, near the electrode surface, pH drifts away from the equilibrium value in the bulk solution far away from the electrode. This is due to the proton consumption (or hydroxide ion formation) occurring simultaneously with every charge consumed for the reduction reactions. Therefore, local pH near the electrode shifts to higher values compared to the bulk pH and the extent of the shift is determined by the bicarbonate concentration (and the solution buffering capacity), rate of charge consumption, and mass transfer kinetics.[7,62,63] As concentrations of CO_2 and the stability of reaction intermediates are affected by pH, local pH variations need to be taken into account in the development of electrocatalysts and the design of electrochemical reactors.

Electrolyte salt used and its concentration can affect the CO_2 reduction activity/selectivity. The choice of the anion influences the reaction by its buffering capacity in maintaining the local pH close to equilibrium and the capability to act as a proton donor.[8,22] Therefore, product distributions for the CO_2 reduction products and the faradaic efficiency for HER, which is a competing reaction, all varies depending on its type and concentration.

Cationic species also influence the CO_2 reduction reaction at the surface of a catalyst which is observed as a shift in the current density and the production distribution.[8] As the cation size becomes larger (*i.e.* from Li^+ to Cs^+ among alkali metal ions) CO_2 reduction reactions are favored on metal surfaces.[64–66] One explanation provided for this effect is the decreasing pK_a for cation hydrolysis with increasing cation size which leads to a higher buffering capacity near the electrode.[66] It is suggested that larger cations with increased buffer capacity keep the pH relatively lower and as a result the local CO_2 concentration higher, providing a favorable environment for CO_2 reduction.[66,67] In addition, cations have been suggested to play crucial roles in stabilizing surface intermediates. Certain intermediates, such as *COOH, *CHO, and $*C_2O_2$, can be stabilized by either the co-adsorbed cation[68] or the electric field induced by the solvated cation in the vicinity of the catalyst surface.[69,70] Cation-dependent activity in terms of intermediate stabilization was attributed to the varying cation concentration at the outer Helmholtz plane (OHP), with higher concentrations achieved for larger cations due to their stronger driving force to be at the OHP.[69]

Temperature and pressure can also influence the catalytic behavior observed on the electrodes. These two factors mainly alter the concentration of dissolved CO_2 in the electrolyte solution, where low temperatures and high CO_2 pressures allow higher CO_2 concentrations in a saturated solution.[7,71,72] Increased CO_2 concentration allows higher selectivity for CO_2 reduced products, with even some metals that mainly perform HER to be catalytically active for CO_2 reduction.[8]

Another important aspect to consider is the effect of impurity metal ions in the solution that can adversely interfere with the CO_2 catalytic reaction. Small concentrations of metal impurities, such as lead or iron, can form adsorbed monolayers under reductive bias and this type of surface contamination can lead to the enhancement of hydrogen evolution against CO_2 reduction.[8] It has been also shown that anodic stripping of impurity metals can recover the CO_2 electrocatalytic activity and the need of a pre-electrolysis for the solvent system has been emphasized.[73] Metal impurity deposition can also be avoided by extracting metal impurities from electrolyte solutions by other means.[74,75] Some studies have also suggested carbon-based contaminants or adsorbed organic species responsible for catalyst deactivation[43,48,76] and continuous research efforts are needed in this subject for the development of a durable and economical CO_2 electroconversion system.

Chapter 2

Bimetallic nanoparticles for CO_2 electrocatalysis

Reproduced with permission from "Kim, D., Resasco, J., Yu, Y., Asiri, A. M. & Yang, P. Synergistic geometric and electronic effects for electrochemical reduction of carbon dioxide using gold–copper bimetallic nanoparticles. Nat. Commun. ***5,*** *4948 (2014)." Copyright 2014 Macmillan Publishers Limited.*

Reproduced with permission from "Kim, D., Xie, C.*, Becknell, N., Yu, Y., Karamad, M., Chan, K., Crumlin, E. J., Norskov, J. K. & Yang, P. Electrochemical Activation of CO_2 through Atomic Ordering Transformations of AuCu Nanoparticles. J. Am. Chem. Soc.* ***139,*** *8329–8336 (2017)." Copyright 2017 American Chemical Society.*

As mentioned in the introduction, monometallic catalysts are limited by the type of surface constructions that can be utilized for catalytic transformation reactions and the scaling relationship among a large number intermediates. One method to overcome these limitations is to utilize a system composed of more than one element which is a multimetallic material. It diversifies the possible surface structures and the relevant catalytic properties that can be attained compared to a single element material. Furthermore, having additional elements on the surface can introduce specific binding modes for certain intermediates which break the scaling relations (Fig. 2.1).

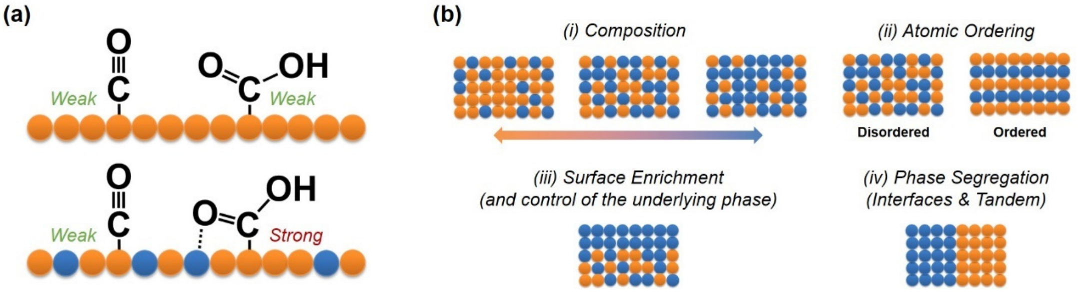

Figure 2.1. Bimetallic surface structures. (a) Decoupling the interaction strength of multiple intermediates with bimetallic surfaces. (b) Structural diversity of bimetallic systems.

In this regard, bimetallic systems have been a popular choice for catalyst exploration. Even with just two elements, widely tunable compositions allow access to a large number of discrete catalytic properties. However, the structural diversity of bimetallic systems is even more immense if one considers the physical arrangements of the two elements at multiple length scales (Fig. 2.1b). Furthermore, by using nanoparticles as catalytic platforms, the material space of accessible catalysts expands even further by the introduction of the nanoparticle related variables such as size and morphology. The structural diversity of bimetallic nanoparticles and their catalytic potential warrants a close study on exploring the various methods of tuning their structure and the related catalytic properties.

Therefore, I have studied gold-copper bimetallic nanoparticles as electrocatalysts for CO_2 reduction. The choice of the two elements was based on the catalytic properties of each single element where both were observed to be catalytically active for CO_2 reduction. CO_2 electrocatalytic properties were explored by systematically tuning the composition and the degree atomic of orderedness of the AuCu nanoparticles. Detailed structural characterizations of the nanoparticles were correlated to their catalytic activity to understand the activity shifts and provide insights to the ways of controlling their catalytic behavior.

2.1. Composition-dependent CO_2 electroreduction of gold-copper bimetallic nanoparticles

Metal alloying has been suggested as one of the approaches to enhance the catalytic activity and selectivity for CO_2 electroreduction.[59,60] By alloying, it is believed that we might be able to tune the binding strength of intermediates on a catalyst surface to enhance its reaction kinetics. In this regard, the Au–Cu bimetallic system has been suggested as a potential CO_2 reduction electrocatalyst in previous reports.[77] However, there has not been a systematic study to precisely understand its activity as function of its composition. Furthermore, Au and Cu have been identified to possess intermediate binding strength favorable for CO_2 reduction;[59,60] hence, they serve as a good starting point to tune the energetics of the intermediate binding to achieve even higher activity.

2.1.1. Synthesis and characterization of gold-copper bimetallic nanoparticles

Figure 2.2a is a transmission electron microscopy (TEM) image of $AuCu_3$ nanocrystals as synthesized. The synthetic procedures were modified from the methods reported previously.[78] Nanoparticles with different stoichiometric ratios of Au-to-Cu (Au, Au_3Cu, AuCu, $AuCu_3$ and Cu) were synthesized in a similar manner with average size all close to 10-11 nm, so that once assembled in a nanoparticle monolayer configuration the catalytically active surface area for each electrode is essentially identical. The composition of each nanoparticle is confirmed using a number of methods. X-ray diffractometry (XRD) shows that the XRD pattern of each particle (Fig. 2.2b) matches with the corresponding characteristic patterns of each phase, although we find Cu to inevitably have a thin oxide shell, as can be seen from its XRD data. In addition, Au and Cu atoms are randomly distributed within the lattice, which is expected considering the synthetic conditions.[79] Ultraviolet-visible spectroscopy (UV-vis) is also a useful way to characterize nanoparticles. Au and Cu nanoparticles in their pure phase exhibit characteristic surface plasmon resonance (SPR) peaks at ~523 and ~570 nm.[77,80,81] As the content of Cu increases in a pure Au nanoparticle by forming an alloy, the SPR peak of Au red-shifts towards the SPR peak of Cu with some broadening (Fig. 2.2c).[77,81] The SPR peaks (λ_{SPR} = 533nm for Au_3Cu, 539nm for AuCu and 549nm for $AuCu_3$) also match well with their composition.[77,81] Energy-dispersive X-ray spectroscopy was further used to confirm the composition of the nanoparticles. All these results confirmed that we have synthesized monodisperse Au–Cu bimetallic nanoparticles with specific stoichiometric ratios of Au-to-Cu.

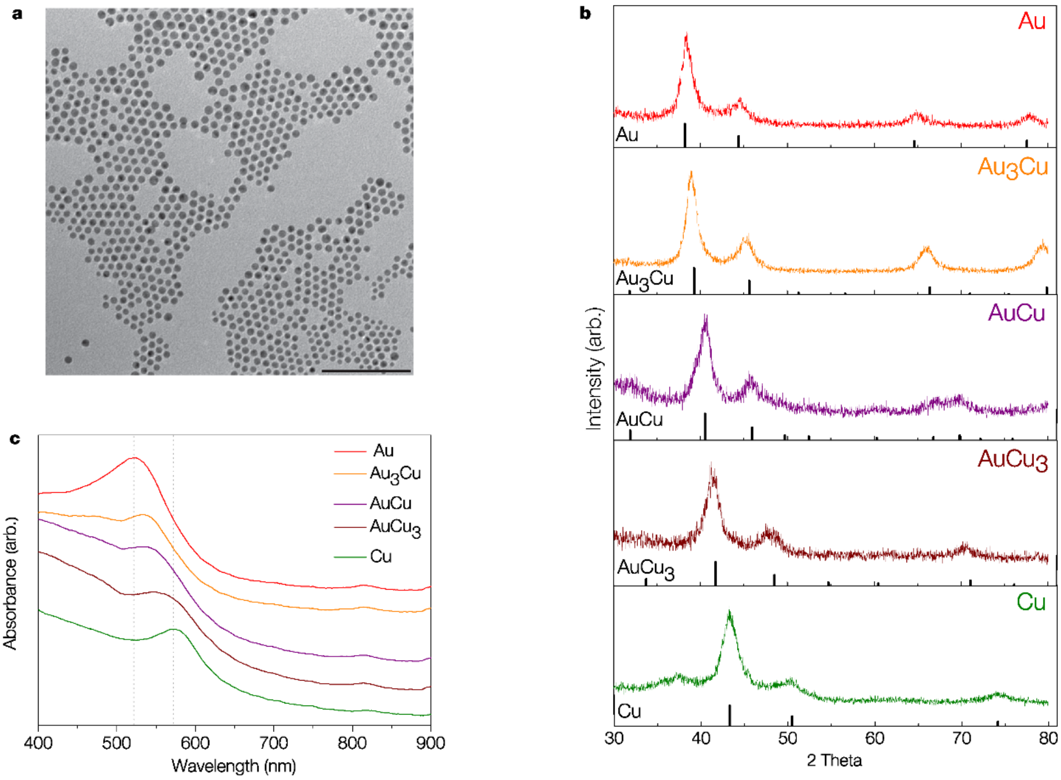

Figure 2.2. Characterization of Au–Cu bimetallic nanoparticles. (a) TEM image of $AuCu_3$ nanoparticles (scale bar, 100 nm). Average size 11.20 ± 1.65 nm. (b) XRD patterns of Au–Cu bimetallic nanoparticles compared with diffraction patterns from the database (Au, JCPDS 03-065-2870; Au_3Cu, JCPDS 01-071-5023; AuCu, JCPDS 00-025-1220; $AuCu_3$, JCPDS 03-065-3249; Cu, JCPDS 00-004-0836). A small peak at 2Θ ~37° in the XRD pattern of Cu indicates the presence of a Cu_2O shell. (c) Ultraviolet–visible spectra of Au–

Cu bimetallic nanoparticles. Dotted lines indicate the SPR peak of pure Au (~523nm) and Cu (~570nm) nanoparticles.

The Au-Cu bimetallic nanoparticles were assembled onto a flat support to be used as an electrode. Nanoparticle assembly (or self-assembly) has been the subject of research for use of these unique structures in a wide variety of applications.[82,83] Among several approaches that lead to monolayer assemblies, we implemented the solvent evaporation-mediated self-assembly approach modified from its original method,[84] to fabricate nanoparticle monolayer platforms. Once assembled, the nanoparticle monolayers were transferred onto a glassy carbon substrate using the Langmuir–Schaefer method and tested in our electrochemical setup for CO_2 reduction. Figure 2.3 shows a scanning electron microscopy image of a $AuCu_3$ monolayer on a substrate. Most of the area is covered with the nanoparticle monolayer with high degree of ordering throughout the substrate, although it also contains some defective spots such as vacancies.

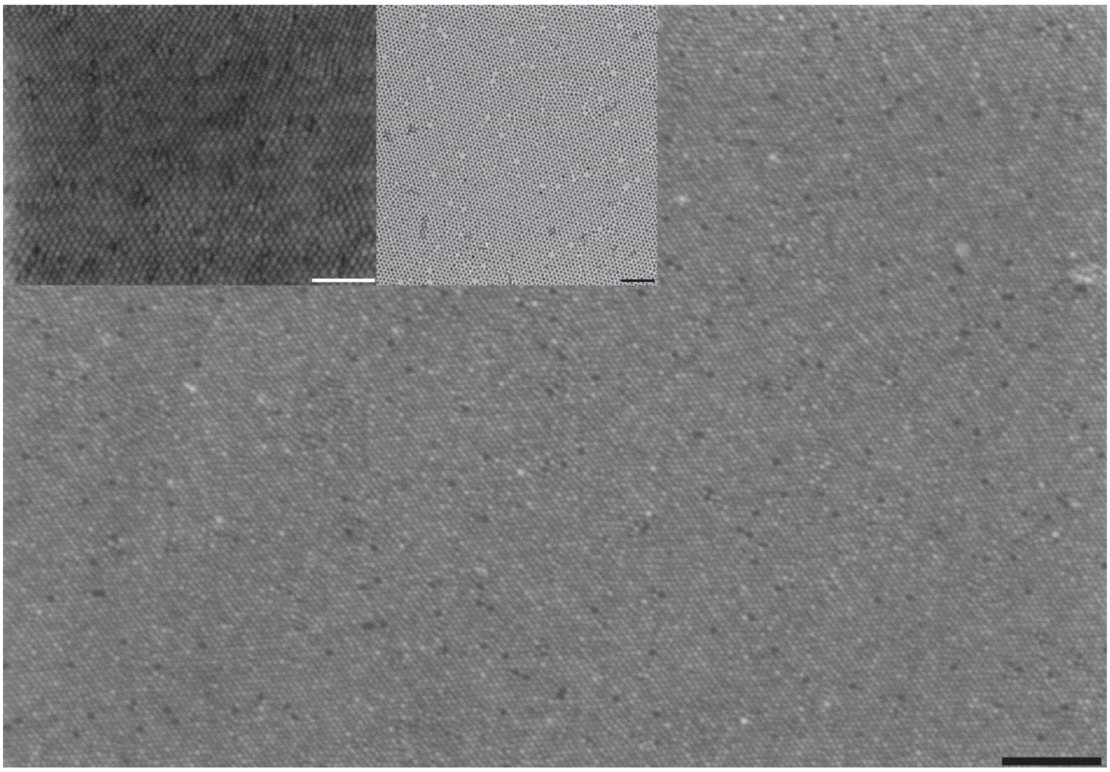

Figure 2.3. Scanning electron microscopy (SEM) image of a $AuCu_3$ nanoparticle monolayer transferred to a substrate using Langmuir–Schaefer technique (scale bar, 200nm). (Left inset) Higher-magnification SEM image of a Au_3Cu nanoparticle monolayer (scale bar, 100 nm). (Right inset) TEM image of a Cu nanoparticle monolayer transferred to a TEM grid (scale bar, 100 nm).

2.1.2. CO_2 reduction activity of gold-copper bimetallic nanoparticles

To quantitatively determine and compare catalytic activity, the monolayered nanoparticles were analyzed in our custom designed electrochemical setup coupled with gas chromatography. The effluent gas from the electrochemical cell went through the sampling system of the gas chromatography and gas products were analyzed in real-time, while the liquid products were analyzed after the reaction by quantitative nuclear magnetic resonance spectroscopy. Electrolysis was performed under standard conditions of 0.1M $KHCO_3$ electrolyte saturated with CO_2.

Figure 2.4a shows the overall activity of the Au–Cu bimetallic nanoparticles under identical reaction conditions. Pure Cu nanoparticles exhibit the lowest overall activity, while increasing the Au content enhances the activity up to the point where Au_3Cu seems to exhibit the highest activity among the series. However, as the overall current density also includes the current from HER, it is difficult to determine which catalyst performs better for CO_2 reduction just from this plot. Furthermore, as electrochemical CO_2 reduction typically leads to a large number of chemical products, the overall current must be divided into individual products to get a quantitative understanding of the activity and selectivity as function of composition. One way of doing this is to examine the Faradaic efficiencies (FE) for each product, which are shown in Fig. 2.4b–f. The results are interesting, as it is generally believed Cu is the only catalyst capable to produce a wide range of products. Not only do the Au–Cu bimetallic nanoparticles make products usually seen on Cu, but the FE of these products shifts as the composition is changed. As the Cu content increases, the total number of products increases and the pure Cu nanoparticles exhibit the largest number in product type. Among the products that require more than two electron transfers, methane and ethylene are considered as major products that can be produced from Cu.[7,9] For methane and ethylene, the FE decreases substantially as more Au gets incorporated into the nanoparticle, eventually leading to a total loss of these products for nanoparticles with high concentrations of Au. Further, Fig. 2.4b–f reveals that the trends in FE for CO and H_2 are opposite as the composition shifts. FE for CO increases with Au content, while FE for H_2 decreases as the Au content increases. For pure Au nanoparticles, the FE for CO is close to ~65%, which is consistent with other reports for Au nanoparticles of similar size.[85] In the case of formate, which is known as the largest molecular liquid product from Cu, the trend seems to follow hydrocarbon species such as methane, although the decrease is not drastic.

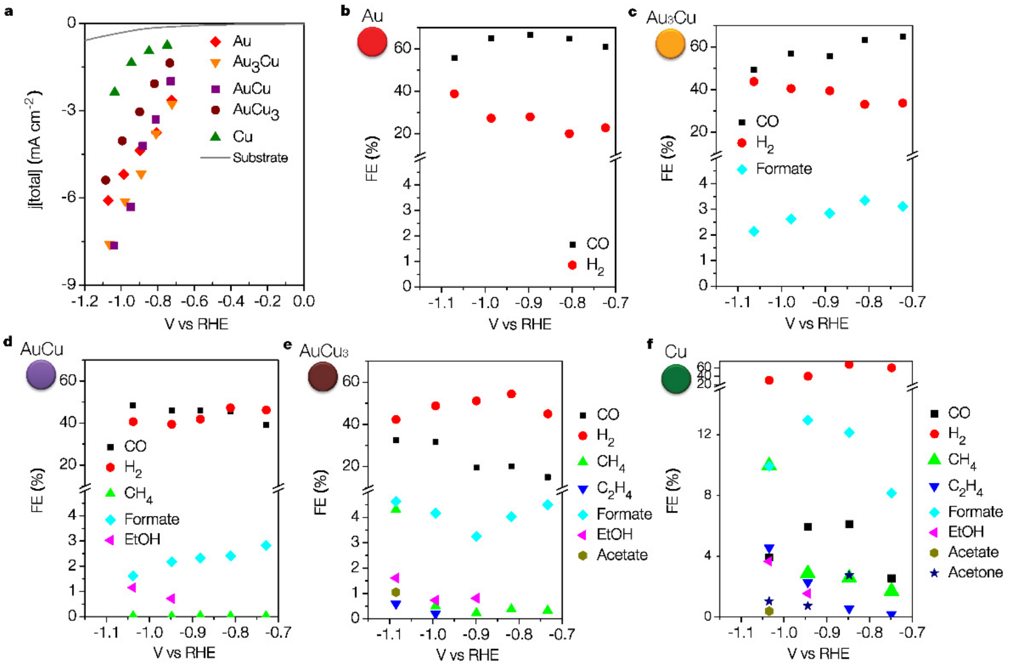

Figure 2.4. Catalytic activities of Au–Cu bimetallic nanoparticles. (a) Total current density plot of Au–Cu bimetallic nanoparticles. Current density is from the geometric area of the electrodes. All measurements were under the same environment of 0.1M $KHCO_3$ (pH 6.8) at 1 atm CO_2 and room temperature. The grey line indicates the activity of the bare substrate from linear sweep voltammetry (50mV/s) stabilized after multiple cycles. On the plot is the average current density of multiple runs at each potential. FE for each product of (b) Au, (c) Au_3Cu, (d) AuCu, (e) $AuCu_3$, and (f) Cu.

Based on this analysis and comparison, the reactions that require a hydrogen atom binding to the carbon along the reaction pathway tend to have decreased in FE for their final products following the same trend for H_2, while FE of CO shows the opposite trend where protonation happens at the hydroxyl end group of a carboxyl intermediate stabilized on the surface.[39,59,60] To protonate the carbon atom, a surface-stabilized proton has to be near the active site and this indicates that the product distribution in CO_2 reduction might be related to the binding strength of hydrogen on the surface of a catalyst. In principle, we could expect that the binding strength of all the intermediates that occur along the reaction pathway would govern the activity/selectivity, as it determines the interaction of the intermediates with the catalyst and lead into different reactions pathways and final chemical products. Therefore, at this point, it is reasonable to assume that by tuning the composition of Au–Cu bimetallic nanoparticles, we are tuning the degree of stabilization of the intermediates on these nanoparticle surfaces, and consequently, different final chemical product profiles were observed.

Figure 2.5a compares the relative TOR for CO at -0.73V versus reversible hydrogen electrode (RHE) for these nanoparticles with different compositions. We found that the activity follows a volcano shape with a peak activity for Au_3Cu (Au_3Cu ~93.1 times, Au ~83.7 times and AuCu ~40.4 times higher relative to Cu). This trend can be understood by considering the elementary reaction steps from CO_2 to CO.[60] In this reaction, CO_2 is adsorbed onto the surface as COOH and further reduced to CO. Therefore, the binding strength of COOH and CO essentially governs CO TOR. To enhance the CO production kinetics, a catalyst has to stabilize COOH more strongly relative to CO, so that CO_2 readily activates to COOH and desorbs as CO. However, this is difficult to achieve with a monometallic catalyst because of the scaling relation, which shows that the binding strengths of different intermediates scale together.[59] Alloy catalysts, on the other hand, could potentially stabilize COOH relative to CO by forming an additional bond at the oxygen end with an oxophilic element (that is, Cu) on the catalyst surface.[59,60] Based on this observation, the CO activity of Au–Cu bimetallic nanoparticles can be explained in terms of (1) the electronic effect where the binding of intermediates can be tuned using different surface composition and (2) the geometric effect that has to do with the local atomic arrangement at the active site, which allows the catalyst to deviate from the scaling relation.

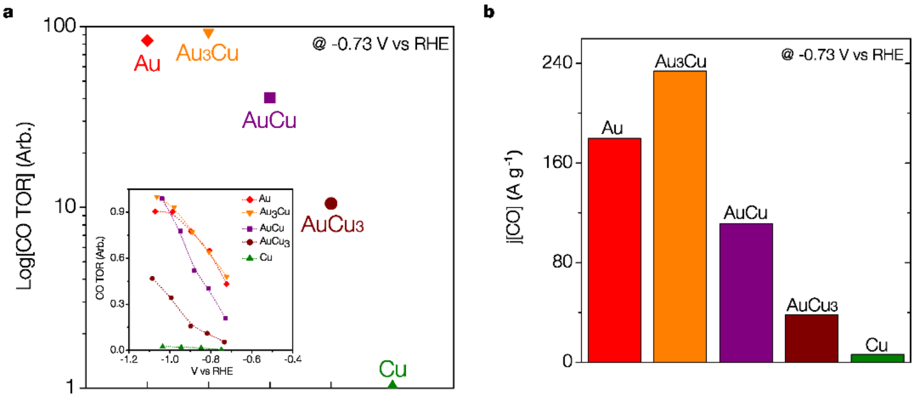

Figure 2.5. Trends in TORs of Au–Cu bimetallic nanoparticles and their mass activity. (a) Relative TORs for carbon monoxide compared at -0.73V vs RHE. TOR calculations are based on the partial current density and the TOR of Cu is set to one. Each data point is spaced equally apart on the x axis and the TORs are plotted in log scale. Inset shows relative CO TOR (where all the data are normalized to the highest value) as a function of potential. (b) CO mass activity of Au–Cu bimetallic nanoparticles at -0.73V vs RHE. Mass activity is based on the overall mass of Au and Cu.

The electronic effect on the binding strength of intermediates is due to the change in the electronic structure of a catalyst. For transition metals, the way their *d*-band interacts with the adsorbate determines the binding strength. The trend is that the more low lying (relative to the Fermi level) the *d*-band, the weaker the binding due to the occupancy of anti-bonding states.[86] Figure 2.6a is the surface valance band spectra of Au–Cu bimetallic nanoparticles collected by high-resolution X-ray photoemission spectroscopy (XPS) on the nanoparticle monolayers. Using Al Ka source, the binding energy was scanned from 0 to 20 eV and each spectrum was collected over ~1,000 scans. The spectra reveal that the *d*-band and its centre of gravity gradually shift downwards from Cu to Au.[87] According to this trend, the binding strength for COOH and CO, which is mainly from the bond between the active site and the carbon, should decrease as Au content increases. Then the binding strength to Au–Cu bimetallic nanoparticles would lie in between Au and Cu following the scaling trend, which can also be estimated from the interpolation principle.[86] It is known that Au has the optimum binding strength for COOH and CO to reach peak activity among the transition metal catalysts for CO_2 to CO conversion.[60] Therefore, from the electronic effect, Au is expected to be at the peak of the volcano, while the activity scales down linearly to Cu as the composition shifts. However, we observe peak activity for Au_3Cu and also activities higher for AuCu and $AuCu_3$ than predicted from a trendline between Au and Cu. In addition to the interesting trend in CO activity, the shift in selectivity and the presence of formate produced from Au_3Cu but not pure Au needs to be understood from more than the electronic effect, considering the similar electronic structures of Au and Au_3Cu. These observations indicate that the activity is not solely determined from the electronic effect.

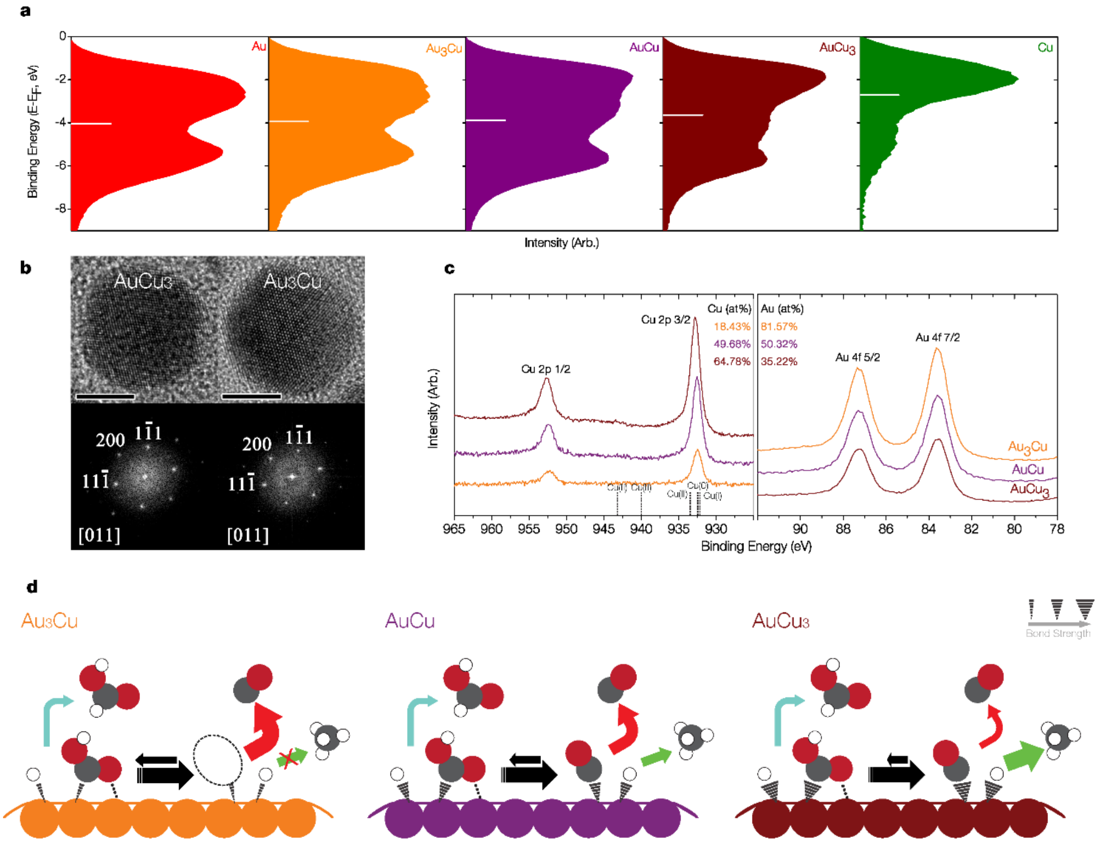

Figure 2.6. Structural characterization of Au–Cu bimetallic nanoparticles. (a) Surface valence band photoemission spectra of Au–Cu bimetallic nanoparticles. All the spectra are background corrected. The white bar indicates its centre of gravity. (b) High-resolution transmission electron microscopy image of $AuCu_3$ and Au_3Cu, and their fast fourier transform. Scale bar, 5 nm. (c) X-ray photoemission spectra at grazing angle (85°) on Au–Cu bimetallic nanoparticle monolayers. (d) Schematic showing the proposed mechanism for CO_2 reduction on the catalyst surface of Au–Cu bimetallic nanoparticles. Filled circles with grey is C, red is O and white is H. The relative intermediate binding strength is indicated by the stroke weight (on the top right corner). Additional binding between the COOH and the catalyst surface is presented as a dotted line. Arrows between the adsorbed COOH and adsorbed CO is to show the difference in probability of having COOH adsorbed on different types of surfaces. Colored arrows indicate the pathway to each product: red for CO, blue for formate and green for hydrocarbons. Larger arrows indicate higher turnover.

The geometric effect also plays an important role in determining catalytic activity, as it has to do with the atomic arrangement at the active site. The way the active site is configured can have a large effect on the binding strength of intermediates.[88] In the case of Au–Cu bimetallic nanoparticles, further stabilization of COOH becomes possible by having a Cu atom adjacent to a Au-C primary bond, where it can form a bond with the oxygen end of COOH. As can be seen from high resolution TEM images and their fast fourier transform (Fig. 2.6b), the nanoparticles have a uniform phase with d-spacings corresponding to their compositions and the lack of complete Au/Cu atomic ordering, which is in agreement with other characterization methods discussed above. Further, the surface compositions of Au–Cu bimetallic nanoparticles also follow the trend of their bulk compositions, evidenced from XPS spectra (Fig. 2.6c) at a grazing angle, which is highly surface sensitive. Thus, it is reasonable to assume that both elements are uniformly distributed throughout the particle according to their compositions and that these bimetallic nanoparticles are capable of providing active sites with further COOH stabilization. The electronic effect and geometric effect, operating synergistically here, lead to the observed volcano activity correlation with nanoparticle composition.

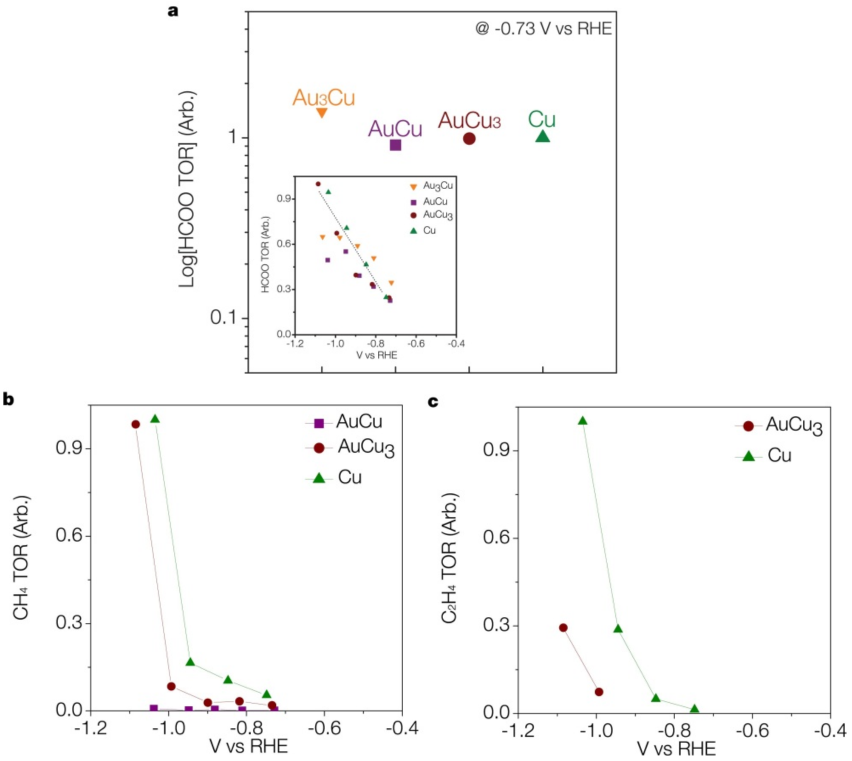

Figure 2.7. Formate and hydrocarbon TOR of Au-Cu bimetallic nanoparticles. (a) Relative turnover rates for formate compared at -0.73 V vs RHE. The TOR of Cu is set to one. Inset shows relative formate TOR (where all the data are normalized to the highest value) as a function of potential. (b) Relative methane TOR as a function of potential. (c) Relative ethylene TOR as a function of potential.

However, we did not observe a clear trend with the TOR for formate. Formate TOR was rather close in value among the different catalysts (Fig. 2.7). This can also be understood in terms of the change in the binding energy of the intermediates. To produce formate, the active site should be capable of stabilizing both COOH and H, so that there is a high probability of forming a bond between the carbon and the adsorbed proton. However, the relative free energy of adsorbed CO is lower than adsorbed COOH.[39,59,60] Therefore, COOH is more likely to be converted into CO rather than staying adsorbed as it is. As more Au gets incorporated into Cu, the relative free energy difference between adsorbed COOH and CO narrows.[59] Further, alloy nanoparticles have the capability of further stabilizing COOH due to the geometric effect. Hence, there is higher probability for being adsorbed as COOH. In contrast, the binding strength for H gets weaker as the Au content rises.[89] These two opposing effects lead to $HCOO^-$ TOR being relatively unaffected by the compositional shift.

Products that require larger number of reaction steps, such as methane or ethylene, diminish significantly even with a slight shift in composition from pure Cu. This might be due to the fact that these products require stabilization of both CO and H. Adsorbed CO is protonated successively to evolve as hydrocarbon species.[39] Cu seems to have the optimum binding strength for both of the adsorbed intermediates to facilitate the conversion. However, as the Au content increases, both intermediates bind weaker, which reduces the TOR and leads to total loss of these products.

The use of our unique nanoparticle monolayer not only allows us to carry out the quantitative comparison of the CO_2 reduction activity/selectivity as a function of composition, it also leads to high efficiencies by significantly enhancing mass activities. Au_3Cu, which has the highest mass activity for CO, outperforms conventional Au nanoparticle catalysts[85] by more than an order of magnitude (Fig. 2.5b). There also have been efforts to reduce metal loading by using organometallic catalysts with large enhancements in mass activity.[90] The idea is to significantly reduce the metal loading by having a single metal atom coordinated to organic ligands that can perform the reduction of CO_2. In the case of Ag, widely known as an efficient catalyst for CO production, this approach led to more than an order-of-magnitude increase in mass activity compared with pure Ag nanoparticles. Our nanoparticle catalyst monolayers, characteristic of efficient loading, can operate at comparable activities to these organometallic catalysts for CO production (even considering the fact that Au is much heavier).

2.1.3. Discussion and Conclusion

The complexity of the reaction is clearly evidenced from the activity trends of Au–Cu bimetallic nanoparticles. The TOR and the product distribution are governed by various intermediates that occur along the reaction pathway. However, we were able to show that this multi-parameter reaction could be described in terms of two effects (as shown in Fig. 2.6d), the electronic effect and the geometric effect. From these two factors, one can deduce how the intermediates will interact with the surface of a specific catalyst and hence tune its catalytic activity. To achieve high selectivity towards only CO_2-reduced products, one should try to mitigate the proton–catalyst interaction (to suppress HER) and at the same time optimize the binding strength of the first few intermediates (COOH and CO) in the pathway by using both effects. However, if the emphasis is on producing products with larger number of electron and proton transfers (that is, methane), the catalyst should be able to stabilize CO even further and allow coupling with the adsorbed proton or hydroxyl groups more efficiently. This might inevitably lead to higher production rates of H_2, but if the atomic configuration on the active site prohibits proton–proton coupling, one might be able to achieve higher selectivity even for more complex products as well. In the design of a CO_2 reduction catalyst, one should carefully balance how these two effects determine the interaction of intermediates with the catalyst so as to achieve better activity and selectivity.

We have used monodisperse Au–Cu bimetallic nanoparticles in a unique platform to understand the trends of their fundamental activity for CO_2 reduction. With its connection to the electronic structure and the local atomic environment, we could understand their catalytic activity systematically and have determined the factors that allow us to simplify the picture of the overall CO_2 reduction. Further, our unique monolayer platform enabled us to measure mass activities significantly higher than catalysts structured by more conventional means. With the principles of catalyst design established, coupled with exceptional structuring of active sites, we believe unprecedented improvements in electrochemical CO_2 reduction will be eventually fulfilled that will allow our goals of a sustainable energy society to finally become a reality.

2.2. Electrochemical activation of CO_2 through atomic ordering transformations of AuCu nanoparticles

Beyond simply controlling the ratio between the elements in a bimetallic system where each is randomly distributed, precise positioning of atoms in a crystal lattice becomes possible when there exists a thermodynamically accessible phase. This results in a distinction between a disordered alloy and an ordered intermetallic structure, and the transition between the two different phases is the so-called order−disorder transformation.[91]

Recent works on ordered intermetallic NPs have focused on developing synthetic strategies to promote ordering transformations from the initial alloy and investigating their structure and properties for applications in magnetism and catalysis.[92–99] Structurally ordered Pt-based (with Fe, Co, Cu, etc.) NPs have been under investigation in the past few years, as the ordered structure has been known to offer enhanced activity and durability for the oxygen reduction reaction (ORR).[93–96,99] On the other hand, for the other well-known bimetallic system of Au−Cu, discovery and use of its enhanced properties, attributable to its having an ordered lattice, have not been well studied, with only a few reports present regarding the synthetic approach to create ordered NPs.[92,97,98,100,101]

Here, we investigate the effects of order−disorder transformation in AuCu NPs on electrochemical CO_2 reduction. We show that the ordering transformation of a disordered AuCu (1:1 atomic ratio) NP turns an inactive catalyst, which mainly generates hydrogen gas, to an active catalyst for reducing CO_2. This was found through systematic control of the ordering degree of AuCu NPs and observation of its effect on the catalytic behavior. We performed detailed structural investigations of ordered AuCu NPs down to the atomic level to find ordered lattice configurations, together with a few-atoms-thick Au layer on the outer surface. Furthermore, thermochemical DFT calculations suggest that the enhanced CO_2 reduction activities observed for ordered intermetallic AuCu NPs arise from the formation of compressively strained Au overlayers.

2.2.1. Atomic ordering transformation of AuCu nanoparticles

AuCu bimetallic nanoparticles with varying degrees of atomic ordering were realized by synthetic procedures modified from earlier work.[92] Mainly, temperature and time were controlled during the incorporation of elemental copper into the gold NP seed, where higher temperatures and longer times promote the formation of ordered lattices. Since we start from identical seed particles, AuCu bimetallic NPs with similar sizes (~7 nm) could be produced that look identical in their morphologies (Figure 2.8a). Au-to-Cu ratios, identified from ICP-AES (Figure 2.8b), are all around 1, confirming their compositional invariance.

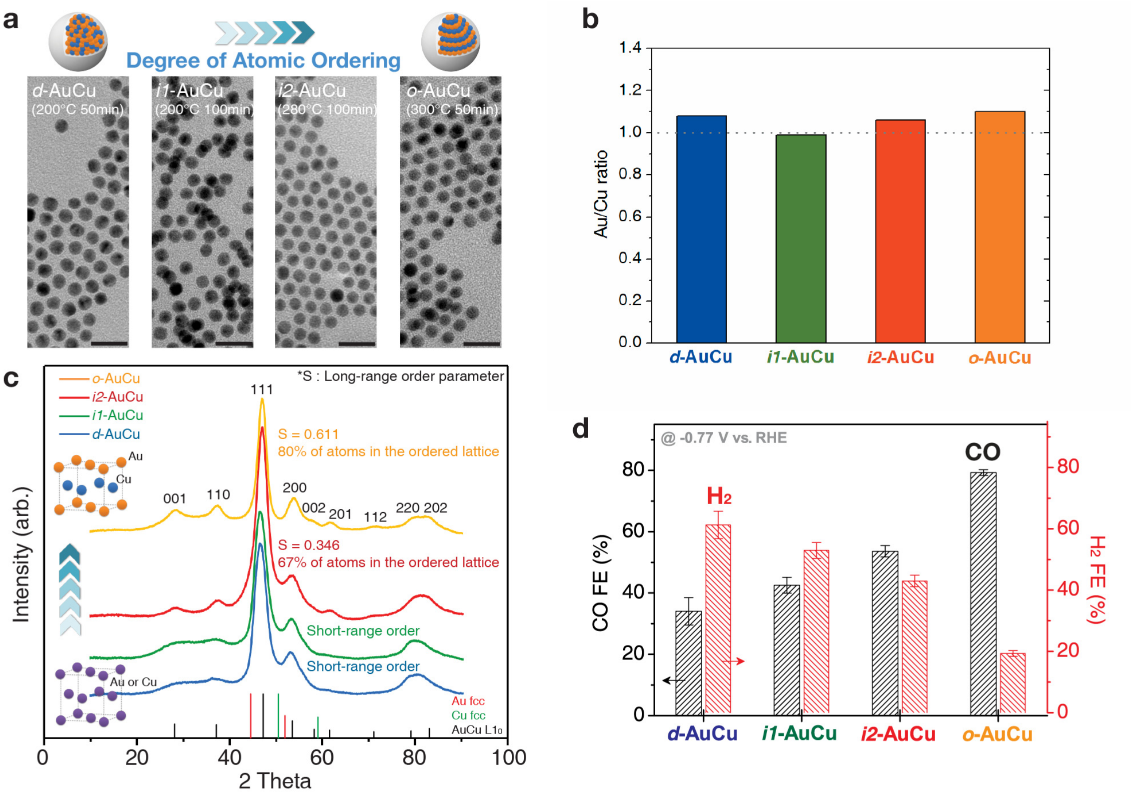

Figure 2.8. Atomic ordering transformation of AuCu bimetallic nanoparticles. (a) TEM images of AuCu bimetallic NPs synthesized at various conditions allowing for systematic tuning of the degree of ordering. Scale bar, 20 nm. (b) ICP-AES analysis of AuCu bimetallic nanoparticles. (c) XRD of AuCu bimetallic NPs. Diffractograms were recorded using Co Kα radiation ($\lambda_{\text{Co K}\alpha}$ = 1.79 Å). (d) Electrochemical CO_2 reduction activities of AuCu bimetallic NPs evaluated by faradaic efficiencies of CO and H_2. Measurements were conducted at −0.77 V vs RHE with 0.1 M $KHCO_3$ solution (pH 6.8) at 1 atm CO_2 and room temperature.

The structural difference between AuCu NPs could be identified from XRD. As shown in Figure 2.8c, the peak positions of 111 and 200 diffractions further confirmed the formation of a bimetallic system, as they lie between those of pure Au and Cu. However, there was a trend where the superlattice peaks, which should be absent in a disordered face-centered cubic (FCC) structure of an alloy, became more evident in the NPs synthesized at higher temperatures for extended periods. Moreover, peak splitting became clearer as well at the 200 and 220 positions, indicating that the crystal structure was transitioning from FCC to face-centered tetragonal. All of these indicated an increase in the degree of atomic ordering following greater input of energy (controlled with temperature and time) during Cu diffusion into Au NP.

The degree of ordering was further quantified by the long-range order parameter (S), estimated from the relative intensity ratio between the superlattice peak and the fundamental peak.[102] The AuCu NP synthesized at 300 °C had the highest S value of 0.611, which corresponded to ~80% of atoms in the ordered lattice positions. After the second most ordered AuCu NP (synthesized at 280 °C 100 min), the degree of ordering could not be quantified by S for the other two NPs, which had only short-range order. Combining the qualitative and quantitative comparisons of degree of ordering among the four AuCu NPs, we could conclude that the AuCu NP synthesized at 200 °C for 50 min (hereafter *d*-AuCu) was disordered (or the least ordered) and the one synthesized at 300 °C for 50 min (hereafter *o*-AuCu) was ordered (or the most ordered). The AuCu NPs at intermediate stages of ordering were named as *i1*-AuCu and *i2*-AuCu.

To study their activity toward electrochemical reduction of CO_2, identical numbers of each type of AuCu NP (mass of 4 μg total) were loaded on carbon paper electrodes. Each NP sample was washed multiple times to the point just before the NP solution became unstable, and the mass fraction of ligands in each sample was kept similar. Any thermal or chemical treatments were avoided so as not to alter their inherent structure produced. Each electrode was then tested in a customized electrochemical setup under conditions of 0.1 M $KHCO_3$ (pH 6.8) at 1 atm CO_2 and room temperature. Linear sweep voltammetry of AuCu NPs resulted in similar current densities from utilizing same number of NPs with identical morphology for each and providing equal surface area. During chronoamperometry, gas products were measured *in situ* using gas chromatography, and liquid products were analyzed from quantitative nuclear magnetic resonance (qNMR) spectroscopy.

The major products formed were CO and H_2, and their faradaic efficiencies (FE) were measured at −0.77 V vs RHE (Figure 2.8d). The only liquid product found was formate at relatively low FE < 5%. For the *d*-AuCu NP, H_2 was the dominant product (H_2 FE ≈ 61% and CO FE ≈ 34%), which meant it was considered rather inactive for electrochemical CO_2 reduction. However, a continuous rise was observed in CO FE with increase in the ordering degree of AuCu NPs, where *o*-AuCu NP exhibited the highest CO selectivity. CO became the major product for *o*-AuCu NP, with FE ≈ 80%. Previous study on the effects of composition in Au-Cu alloys for electrocatalytic CO_2 reduction has shown that H_2 is the major product for AuCu (1:1 ratio), consistent with what we observe from *d*-AuCu or *i1*-AuCu.[103] Surprisingly, without altering composition, we found that the ordering transformation could enhance CO formation, transitioning a CO_2 inactive catalyst to an active catalyst with high CO selectivity. The CO FEs measured at a range of potentials for *d*-AuCu and *o*-AuCu NP further confirmed the activity enhancement following disorder-to-order transformation, where CO formation could be obtained at ~200 mV lower overpotentials (Figure 2.9).

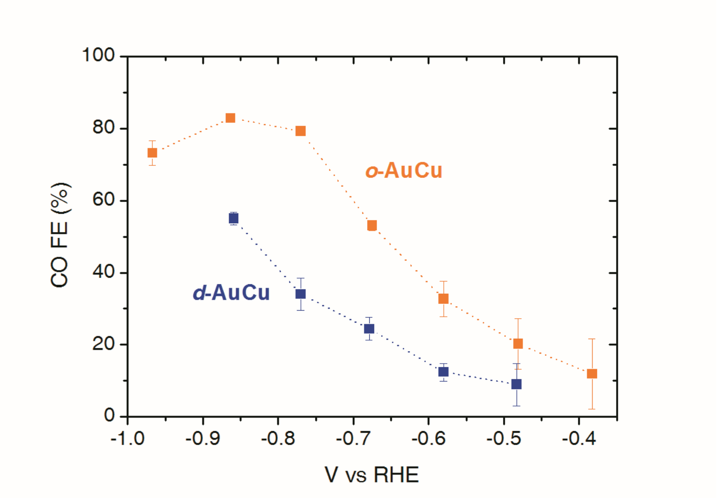

Figure 2.9. CO FE at various potentials for *d*-AuCu and *o*-AuCu NP catalysts.

2.2.2. Structural investigation of ordered AuCu nanoparticles

In order to understand this drastic change in activity that arises from the ordering transformation of AuCu bimetallic NPs, we probed the structure of *d*-AuCu and *o*-AuCu NPs using various methods. Elemental analysis mapping of the distribution of Au and Cu showed that both elements were uniformly distributed in a single NP for both *d*-AuCu and *o*-AuCu NPs (Figure 2.10).

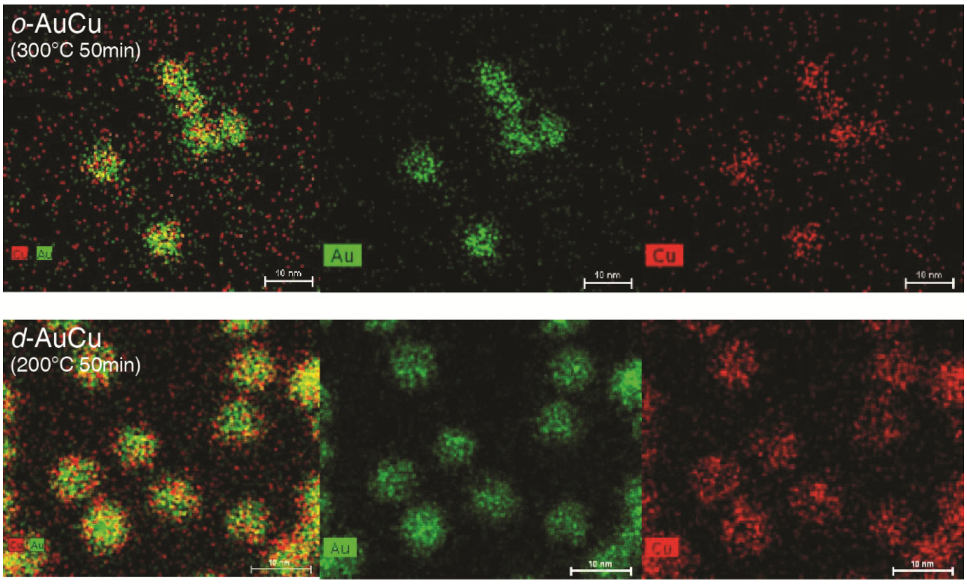

Figure 2.10. Elemental maps of Au and Cu for *d*-AuCu and *o*-AuCu NPs.

In order to investigate down to the atomic level, aberration-corrected HAADF-STEM was implemented. Figures 2.11a and b show aberration-corrected HAADF-STEM images of *o*-AuCu NPs in two different orientations. From the images, a periodic oscillation of intensity was observed, which can be attributed to the Z-contrast differences between different elements that should be present in an ordered lattice. As Au (Z = 79) and Cu (Z = 29) differ greatly in atomic number, a column of Au atoms should appear much brighter than that of Cu atoms in an ordered structure. By measuring the distance between the planes and distinguishing elements by their contrast, certain unit cell orientations of the AuCu $L1_0$ structure were found (Figures 2.11c and d).

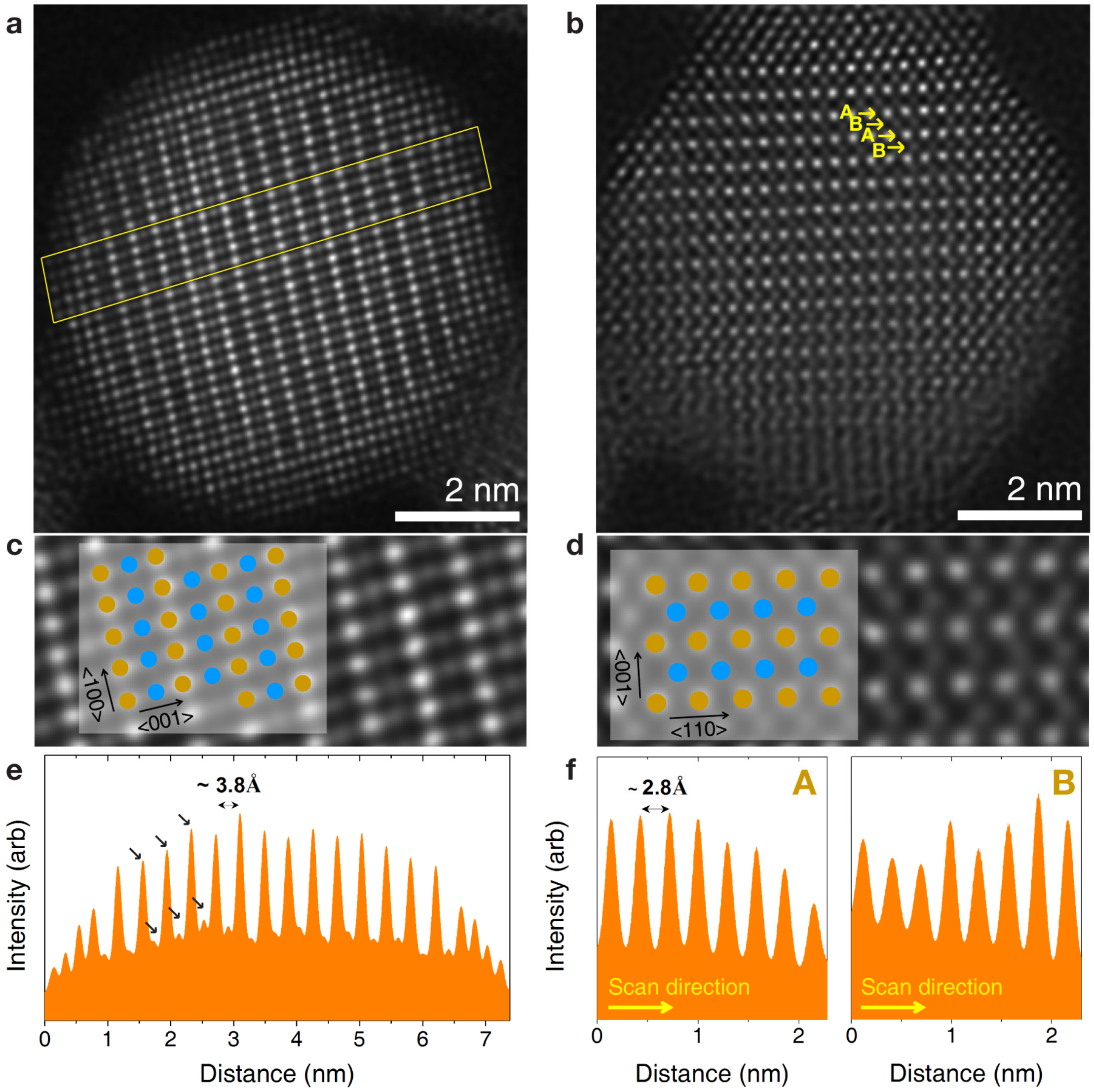

Figure 2.11. Structural investigation of *o*-AuCu at atomic resolution. Aberration-corrected HAADF-STEM images of *o*-AuCu (a,b) and magnified STEM images of the center of the particle together with the overlapping schematics of structure projections (c,d). Atoms in orange and blue color represent gold and copper, respectively. (e) Intensity profile across the particle measured from the yellow box shown in (a). The distance between the strong intensities matches with the separation between gold atoms. Arrows indicate alternating high and low intensities, which represent gold and copper atoms, respectively. (f) Average intensity profile from the interior to the outer surface of the particle along rows A and B shown in (b). The distance between the peaks shown in A matches with the known separation between gold atoms.

In addition to the atomically ordered structures that were verified, certain elemental characteristics at the surface were also observed. As can be directly seen from the images, atoms near the NP surface contained only brighter intensities of gold, in contrast to the alternating intensities at the core. This suggested a few-atoms-thick gold layer over the structurally ordered core. With the intensity profile measured across the particle (Figure 2.11e), a three-atoms-thick gold layer could be identified. Intensities were also measured along the rows of atoms which should contain only one element (Figure 2.11f). While the intensity along the row of gold atoms decayed to the surface (from the thickness decreasing), the intensity profile along what is supposed to be only copper atoms had spiking intensities starting from three atoms beneath the surface. All of these pointed to the fact that *o*-AuCu NPs contained around three-atoms-thick gold layers grown directly over the ordered lattice. This could be observed in multiple images as well (Figure 2.12). In contrast, aberration-corrected HAADF-STEM images of *d*-AuCu NPs exhibited uniform intensities (Figure 2.12e) from the random distribution of both elements, as expected. From atomically resolved imaging of *o*-AuCu NPs, we could conclude that the ordering transformation of a AuCu NP induced three-atoms-thick gold layers at its surface, in addition to the crystal structure transition to intermetallic ordered phase throughout its interior.

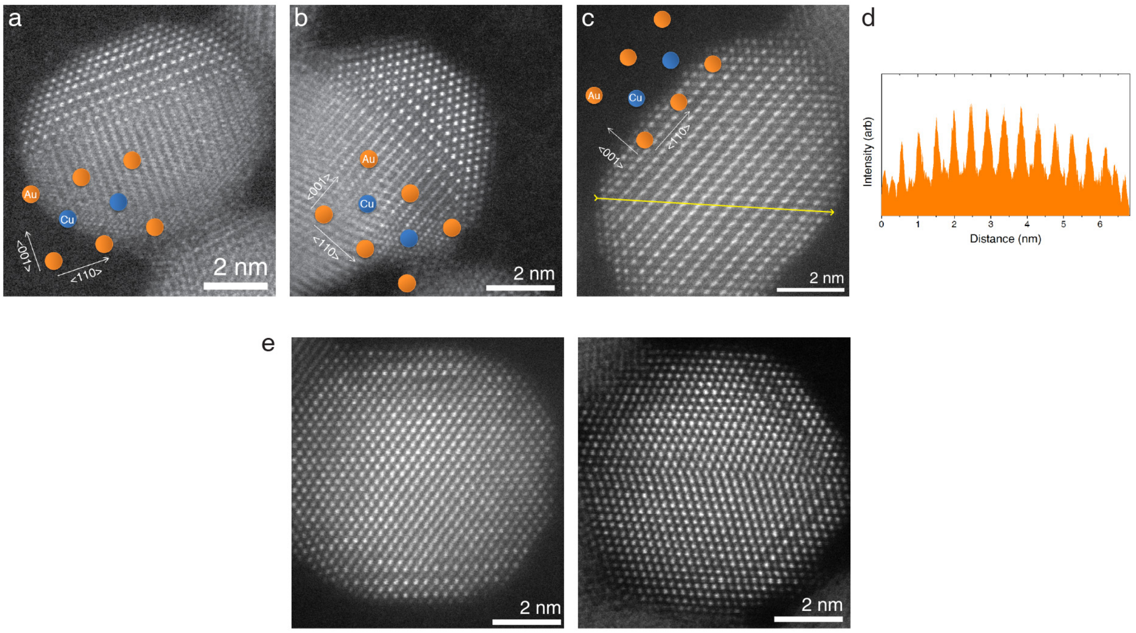

Figure 2.12. Aberration-corrected HAADF-STEM images of AuCu NPs. Aberration-corrected HAADF-STEM images of *o*-AuCu NPs (a, b, c) and an intensity profile along yellow line shown in **c** (d). Aberration-corrected HAADF-STEM images of *d*-AuCu NPs (e).

XAS was used to further probe the structure of AuCu NPs. Absorption spectra at the gold *L_3*-edge and copper *K*-edge were collected from *o*-AuCu NPs and *d*-AuCu NPs. Figure 2.13 presents extended X-ray absorption fine structure (EXAFS) data for both NPs, where the coordination environment surrounding Au and Cu for each NP can be observed. At the Au *L_3*-edge (Figure 2.13a), *o*-AuCu NP exhibits a larger first-shell scattering amplitude, which can be attributed to the stronger constructive interference of photoelectron scattering in the ordered structure. The atomic order is more evident at the Cu *K*-edge (Figure 2.13b), where third and fourth shell scattering (at radial distances from 4 to 6 Å) can be clearly observed due to the unique multiple scattering paths present in the ordered structure. On the other hand, *d*-AuCu NP at the Cu *K*-edge shows many variations of scattering paths at various lengths, together with destructive interference from the disordered structure, which lowers the amplitude.

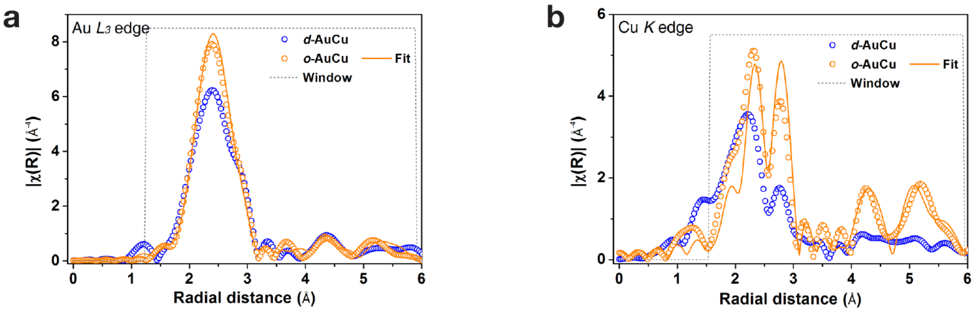

Figure 2.13. X-ray absorption spectroscopy of AuCu NPs. EXAFS spectra at the Au *L_3*-edge (a) and Cu *K*-edge (b) of *o*-AuCu NPs (orange circles) and *d*-AuCu NPs (blue circles). Orange solid lines are the results of fitting to *o*-AuCu NPs.

By fitting the Au *L_3*-edge and Cu *K*-edge of the *o*-AuCu NPs simultaneously to an ordered face-centered tetragonal (L1$_0$) model, information regarding the coordination environment surrounding gold and copper atoms in *o*-AuCu NPs could be extracted (Table 2.1). When comparing the number of nearest neighbor atoms to gold and copper, copper had a coordination number (CN) of 9.0 ± 1.2, while gold had a CN of only 6.9 ± 1.1. The lower first shell CN for gold indicated that gold atoms are relatively undercoordinated compared to copper, which resulted from gold being enriched at the surface[104] as observed from HAADF-STEM. Therefore, from STEM imaging and XAS analysis, we could conclude that the *o*-AuCu NP surface contains a three-atoms-thick gold layer over the ordered AuCu intermetallic core. Furthermore, we speculate NPs at intermediate stages of ordering to have gold overlayers partially covering their surface. Rise in the degree of ordering may lead to increased coverage of gold overlayers associated with the ordered phase. XPS (Figure 2.14a) and UV−vis spectroscopy (Figure 2.14b) were used to further prove that the gold overlayer is only a few atoms thick and not significant enough to be detected by these techniques.[105]

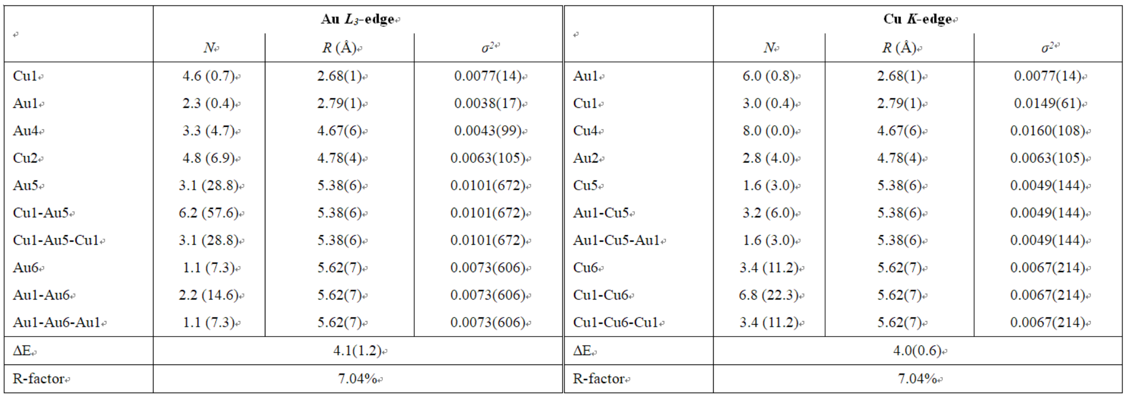

	Au L_3-edge				Cu K-edge		
	N	R (Å)	σ^2		N	R (Å)	σ^2
Cu1	4.6 (0.7)	2.68(1)	0.0077(14)	Au1	6.0 (0.8)	2.68(1)	0.0077(14)
Au1	2.3 (0.4)	2.79(1)	0.0038(17)	Cu1	3.0 (0.4)	2.79(1)	0.0149(61)
Au4	3.3 (4.7)	4.67(6)	0.0043(99)	Cu4	8.0 (0.0)	4.67(6)	0.0160(108)
Cu2	4.8 (6.9)	4.78(4)	0.0063(105)	Au2	2.8 (4.0)	4.78(4)	0.0063(105)
Au5	3.1 (28.8)	5.38(6)	0.0101(672)	Cu5	1.6 (3.0)	5.38(6)	0.0049(144)
Cu1-Au5	6.2 (57.6)	5.38(6)	0.0101(672)	Au1-Cu5	3.2 (6.0)	5.38(6)	0.0049(144)
Cu1-Au5-Cu1	3.1 (28.8)	5.38(6)	0.0101(672)	Au1-Cu5-Au1	1.6 (3.0)	5.38(6)	0.0049(144)
Au6	1.1 (7.3)	5.62(7)	0.0073(606)	Cu6	3.4 (11.2)	5.62(7)	0.0067(214)
Au1-Au6	2.2 (14.6)	5.62(7)	0.0073(606)	Cu1-Cu6	6.8 (22.3)	5.62(7)	0.0067(214)
Au1-Au6-Au1	1.1 (7.3)	5.62(7)	0.0073(606)	Cu1-Cu6-Cu1	3.4 (11.2)	5.62(7)	0.0067(214)
ΔE	4.1(1.2)			ΔE	4.0(0.6)		
R-factor	7.04%			R-factor	7.04%		

Table 2.1. EXAFS fitting parameters for the fit to the *o*-AuCu NP.

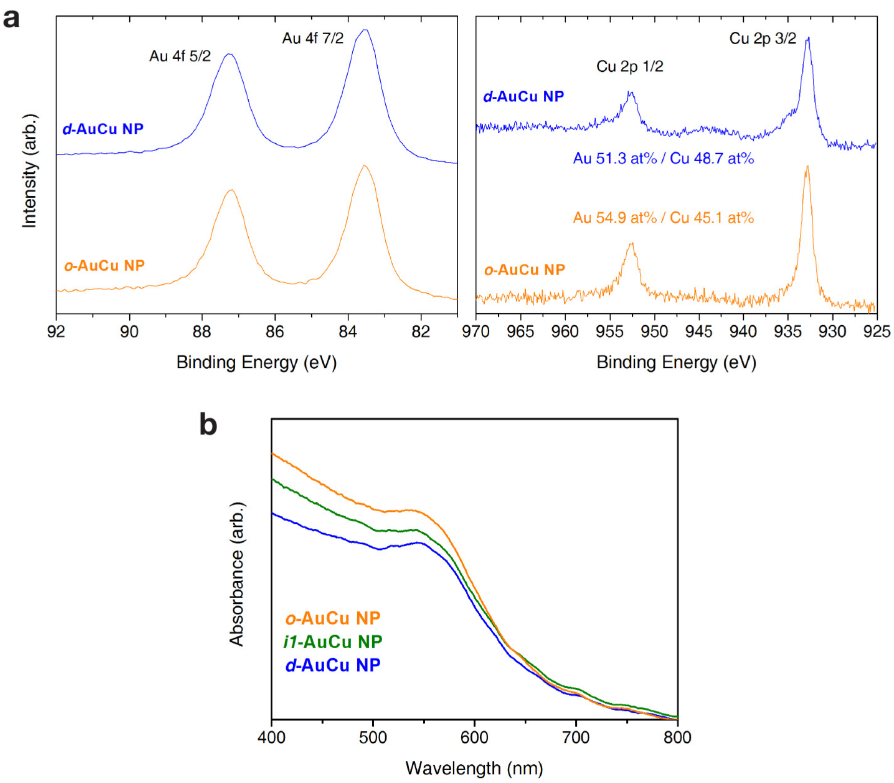

Figure 2.14. XPS and UV-vis of AuCu NPs. (a) Au 4f and Cu 2p XPS spectra of AuCu NPs. Both exhibit Au-to-Cu atomic ratio close to 1. *d*-AuCu NP shows weak signals (~935eV and ~943.5eV) from oxidized copper (Cu^{2+}), which indicates that there is more likelihood of copper atoms being exposed to the surface of *d*-AuCu NP. (b) UV-Vis absorption spectra of AuCu NPs. Surface plasmonic resonance (SPR) results in an absorption peak at ~540nm for Au-Cu bimetallic NP of 1:1 atomic ratio. Degree of atomic ordering does not shift the SPR peak (also expected from their same visual appearance in

color) and this indicates that the gold overlayer formed on *o*-AuCu NP is only few atoms thick. If the thickness of the overlayer becomes significant (beyond ~1nm), the original SPR characteristic decays and the new features from the overlayer appear.

From the structural investigation of *o*-AuCu NPs, we found the formation of a three-atoms-thick gold overlayer following ordering transformation. This suggests that surface enrichment of gold at atomic levels may be the origin of enhanced catalytic behavior. Identifying the precise structures of surface active sites is necessary to gain catalytic insights. Here, we have identified the catalytically active surface structure of a ordered AuCu NP and this may well be extended to other ordered bimetallic systems involving noble and non-noble element mixtures, such as the Cu−Pd system recently demonstrated for CO_2 reduction.[106]

2.2.3. Mechanistic studies of ordered AuCu surfaces

To further investigate electrocatalytic activities for reducing carbon dioxide, CO production rates measured in terms of specific current density (mA/cm^2) and mass activity (A/g$_{Au}$) were probed for AuCu bimetallic NPs, in addition to the FE (Figure 2.15). Catalytic activity of pure Au NPs of same size was compared as well to assess the effects of having a few-atoms-thick Au layer directly over the ordered core. Beyond having NPs of the same dimension with identical numbers to match active surface areas, surface areas were estimated using electrochemical methods. With *o*-AuCu NPs having a three-atoms-thick gold layer on the surface, underpotential deposition of copper in acidic media could be stably performed to estimate their surface area. The same procedure was conducted on Au NPs as well and yielded comparable surface areas.

Figure 2.15a shows CO FEs at −0.77 V vs RHE, where atomic ordering drastically converts AuCu NPs to be selective for CO production as mentioned above. Indeed, this trend is accompanied by rise in the specific CO current density from 0.43 mA/cm^2 for *d*-AuCu NP to 1.39 mA/cm^2 for *o*-AuCu NP (Figure 2.15b). Therefore, we find that atomic ordering in a AuCu bimetallic NP enhanced the intrinsic activity for CO_2-to-CO conversion by 3.2-fold, suggesting the importance of precise control of atomic arrangements in bimetallic NPs for catalytic purposes.

Interestingly, when *o*-AuCu NPs were compared to Au NPs, Au NPs exhibited higher CO selectivity, while *o*-AuCu NPs showed higher activity. Au NPs had a CO FE of 87% and a specific current density of 1.01 mA/cm^2. A similar trend in CO FE and specific current density was observed at other potentials as well. This indicated that a three-atoms-thick gold layer over the intermetallic core possesses different catalytic properties, such as the intermediate binding strength, to a pure gold lattice.

Here, we also probed mass activities (A/g$_{Au}$) for CO formation and, as shown in Figure 2.15c, AuCu NPs are clearly advantageous for CO production with even NPs at intermediate ordering, such as *i1*-AuCu NP, reaching comparable activities to Au NP at ~

320 A/g$_{Au}$. For the *o*-AuCu NP, CO mass activity reaches up to ~830 A/g$_{Au}$, which is 2.6-fold over that of Au NP. For electrochemically producing carbon monoxide, which is considered as the most economically viable so far among various CO_2 reduction products for downstream processing to useful chemicals,[107] various types of gold-based nanostructures have been demonstrated.[15,85,108–110] We find that creating a Au−Cu bimetallic system with induced atomic ordering could be an effective strategy for promoting efficient processing of CO_2, where the structural motifs found here can also be translated to other Au-based morphologies that provide higher current output.[111] Certainly, further efforts are needed to ensure catalytic stability of the motifs found here to the levels required for industrially relevant applications.

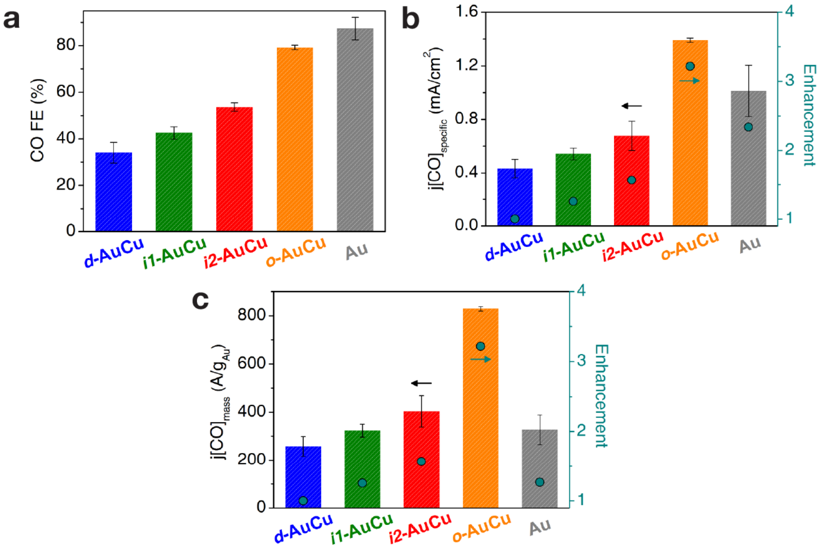

Figure 2.15. Electrocatalytic CO_2 reduction activity of AuCu NPs. CO faradaic efficiencies (a), CO partial current densities (b), and CO mass activities (c) of *d*-AuCu NP, *i1*-AuCu NP, *i2*-AuCu NP, *o*-AuCu NP, and Au NP for electrochemical reduction of CO_2 at −0.77 V vs RHE. CO partial current densities are specific current densities based on actual surface area of NP catalysts measured by Cu underpotential deposition on *o*-AuCu NP and Au NP. Electrochemically active surface areas of *d*-AuCu NP, *i1*-AuCu NP and *i2*-AuCu NP were estimated from the value measured of *o*-AuCu NP. CO mass activities are based on the actual mass of gold (g$_{Au}$) loaded for each catalyst. Green circles in (b) and (c) indicate enhancements over the activity of *d*-AuCu NP, which is set to 1.

The origin of enhanced CO_2 reduction activity by atomic ordering transformations and the resulting three-atoms-thick gold overlayer of AuCu NPs was investigated using DFT calculations. Here, we modeled a (211) facet, since it has been shown that step sites are considerably more energetically favorable for the reactions involved than terrace sites[61] and catalytic activity should be dominated by the step sites.[85] Figure 2.16a shows the model systems considered for AuCu NPs. *o*-AuCu NP was modeled as a strained Au(211) surface, since the underlying intermetallic AuCu lattice compressively strains (~6%) the few-atoms-thick Au layer from its original lattice parameter. In principle, the underlying AuCu phase could also have an electronic effect on the Au overlayers. However, previous theoretical studies have shown that the electronic effect is essentially negligible at transition metal overlayers that are approximately three monolayers thick.[112–115] For the *d*-AuCu NPs, surface stability of various site motifs was investigated and here, we assumed that the surface of *d*-AuCu NPs would be in a metastable state with mixed Au/Cu elemental configuration that has local, short-range order. Of the various (211) facets, the Au-rich (211) step had the lowest surface energy. A model Au(211) surface in its original lattice configuration was also investigated as a comparison.

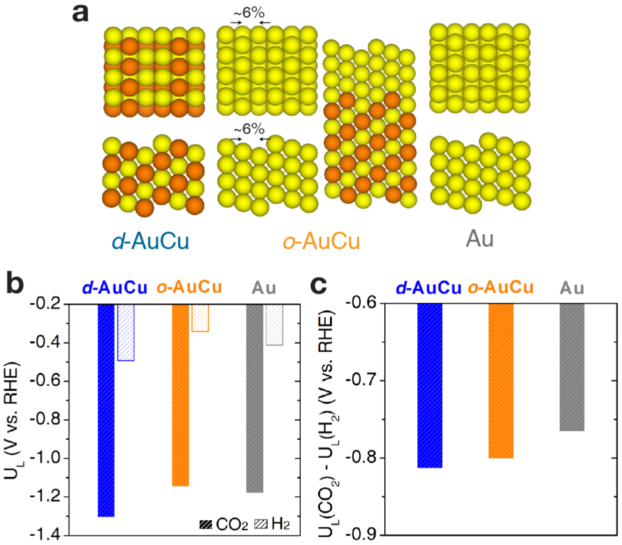

Figure 2.16. Computational results of CO_2 reduction on AuCu surfaces. (a) Top and side views of model 211 slabs for *d*-AuCu NP, *o*-AuCu NP, and Au NP. (b) Calculated limiting potentials for CO_2 reduction and H_2 evolution on model systems. (c) The difference in limiting potentials for CO_2 reduction and H_2 evolution on model systems.

The reduction of CO_2 to CO occurs through a COOH intermediate bound to the active site. For the metals that bind CO weakly, desorption of CO readily occurs, and the formation of *COOH is the potential-limiting step, where * represents a surface site. On the other hand, hydrogen evolution involves *H as the only adsorbed intermediate, and the binding energy of *H has been shown to be a reasonable descriptor of hydrogen evolution activity.[116,117]

Figure 2.16b compares the thermodynamic limiting potentials $U_L(CO_2)$ and $U_L(H_2)$ for the three model systems. Since activation barriers scale linearly with binding energies, trends in limiting potentials reflect trends in catalytic turnover.[118] Based on this analysis, $U_L(CO_2)$ of *o*-AuCu NP is most positive followed by Au NP and *d*-AuCu NP and therefore CO_2-to-CO conversion activity would decrease in the order of *o*-AuCu NP > Au NP > *d*-AuCu NP, which is in agreement to the trend observed experimentally. Recent DFT calculations on transition metals have suggested that the difference between the limiting potentials for CO_2 reduction and H_2 evolution (*i.e.*, $U_L(CO_2) - U_L(H_2)$) can be linked to the trends in experimentally observed CO_2 reduction selectivity.[61] With $U_L(CO_2)$ being more negative than $U_L(H_2)$ for all transition metals, more positive $U_L(CO_2) - U_L(H_2)$ corresponds to higher selectivity toward CO_2 reduction. The trend observed for $U_L(CO_2) - U_L(H_2)$, as shown in Figure 2.16c, suggests that selectivity toward CO_2 reduction decreases in the order of Au NP > *o*-AuCu NP > *d*-AuCu NP, consistent with the experimental trends.

From the thermochemical DFT analysis, we find that the activity of *o*-AuCu NP originates from the compressively strained three-atoms-thick gold layers formed over the AuCu intermetallic core. We note that, while the differences in energetics appear to be only ~0.1 eV, such shifts can provide order of magnitude changes in activity, since the turnover frequencies vary exponentially with activation barriers, which scale linearly with binding energies. Furthermore, projected density of states of the model systems predict a similar trend as well, which shows that the ordering transformation in AuCu should favor CO_2 reduction.

2.2.4. Conclusion

The exquisite control of atomic arrangements in unit cells of bimetallic systems to an individual nanoparticle level could be a promising approach to induce interesting properties and understand their structural origin. The effect of ordering transformations in AuCu bimetallic NPs on their electrocatalytic activity for CO_2 reduction was studied, where ordered AuCu NPs selectively reduced CO_2, in contrast to disordered AuCu NPs that favored hydrogen evolution. With structure probing techniques down to the atomic level, the enhanced activity was attributed to compressively strained three-atoms-thick gold overlayers that formed over the intermetallic core, resulting from the disorder-to-order transformation. With a large number of multimetallic systems accessible, we expect the method of regulating phase transformation between disordered alloys and ordered intermetallics in nanomaterials to have great potential in areas where control over the level of atomic precision is desired.

Chapter 3

Light-driven CO_2 reduction using nanoparticle catalysts

Reproduced with permission from "Kong, Q., Kim, D.*, Liu, C., Yu, Y., Su, Y., Li, Y. & Yang, P. Directed Assembly of Nanoparticle Catalysts on Nanowire Photoelectrodes for Photoelectrochemical CO_2 Reduction. Nano Lett.* ***16,*** *5675–5680 (2016)." Copyright 2016 American Chemical Society.*

Reproduced with permission from "Choi, K. M., Kim, D.*, Rungtaweevoranit, B., Trickett, C. A., Barmanbek, J. T. D., Alshammari, A. S., Yang, P. & Yaghi, O. M. Plasmon-Enhanced Photocatalytic CO_2 Conversion within Metal–Organic Frameworks under Visible Light. J. Am. Chem. Soc.* ***139,*** *356–362 (2017)." Copyright 2017 American Chemical Society.*

In the context of artificial photosynthesis, it is important to pursue efforts in developing a system that can extract charge carriers from absorbed photons and use that charge to drive catalytic reactions. As the entire process involves a number of discrete steps of energy conversion and transfer, the system requires multiple components that have unique functions, such as light absorption and catalytic conversion. Therefore, efforts in this direction require consideration of the ways of interfacing multiple materials without compromising their inherent performance and even allowing synergistic effects to occur. Below, two works that combine nanoparticles with other inorganic and molecular materials for light-driven CO_2 reduction applications will be discussed.

3.1. Directed assembly of nanoparticle catalysts on nanowire photoelectrodes for photoelectrochemical CO_2 reduction

In order to assemble an efficient photosynthetic system, the utmost performance of the individual components is required as well as the optimized spatial arrangement between the components. Recently, a few studies have been reported for photoelectrochemical CO_2 reduction by integrating catalytic components using various methods including photoelectrodeposition, atomic layer deposition, and so forth.[119–122] With the latest advances in discovering efficient CO_2 reducing NP electrocatalysts that have the potential to be light-driven,[85,103,123] it is necessary to develop an effective process for integrating these nanocatalysts with well-studied light absorbers.

Directed assembly of NP catalysts on NW light absorbers is demonstrated here to create an integrated photoelectrode for photoelectrochemical reduction of CO_2. TiO_2-protected n^+p-Si NW arrays were fabricated, in parallel with a Au_3Cu NP catalyst featuring high turnover and mass activity for CO_2-to-CO conversion. Photoelectrochemical production of CO in aqueous environments is demonstrated with the two materials combined as a single device.

3.1.1. Nanoparticle assembly on nanowire arrays

A simple drop-casting process is employed to interface the two materials, where the NW geometry allows the NP solutions to dry in a unidirectional manner with a receding meniscus along the wires (Figure 3.1). As a result the NPs can be uniformly decorated onto the NW surface. This feature is in stark contrast to what is typically observed on planar substrates, where the entire NP solution breaks up into individual droplets to form ring patterns or islands upon drying.[124] SEM images confirm the controllable uniform assembly of individual NPs with varying loading amounts (Figure 3.1c). The uniformity can be maintained even for very large surface coverage (Figure 3.1d). This is particularly important as it allows effective utilization of their nanoscale surface for catalysis. STEM and elemental mapping (Figure 3.1e) further confirm the presence of uniformly distributed Au_3Cu NPs. In contrast, NP assembly on planar substrates with identical procedures typically resulted in the formation of islands where nanoparticles were aggregated.

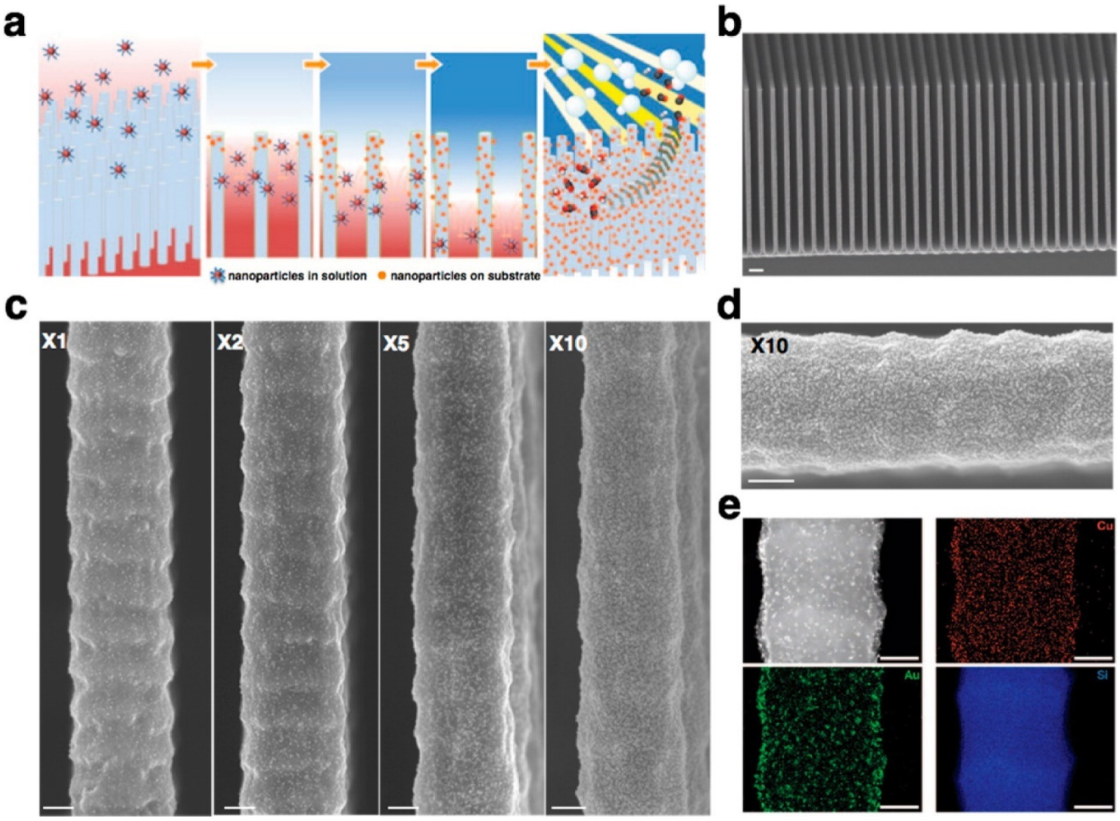

Figure 3.1. Au_3Cu NP assembly on Si NW arrays. (a) Schematic of the nanoparticle assembly process and the use of the integrated system for light-driven CO_2 reduction. (b) SEM image (scale bar 2 μm) of Au_3Cu NP assembled Si NW arrays. (c) SEM images (scale bar 200 nm) demonstrating uniform and tunable NP assembly on Si NW arrays. Numbers indicate loading amounts that have been proportionally varied. (d) Zoom-in image (scale bar 200 nm) of a Si NW with ×10 loading of Au_3Cu NPs uniformly assembled. (e) STEM image and elemental mapping of Au (green), Cu (red), and Si (blue). Though the thick diameter of the Si NW suppresses the contrast of Au and Cu signals to background, we can clearly see the signals originating from the NPs at the edge of the NW. Scale bars are 200 nm.

Quantitative analysis of NP coverage on NW arrays indeed shows a close match between the experimental value and the theoretical estimate assuming NPs are well-dispersed across the NW surface (Figure 3.2a). The detailed analysis of different segments along the NW reveals that the NP distribution exhibits a relatively higher coverage at the top (Figure 3.2b), which could be explained by the unidirectional drying process of the NP solution guided by the NW geometry where the top section of the wires would have been exposed to a relative higher concentration of NPs.[125,126] Our hypothesis of particle deposition with a receding meniscus along the NW surface suggests that the aspect ratio of the nanowires needs to be large enough to accommodate all the NPs in solution before the liquid front reaches the bottom part of the wires. With lower aspect ratio NWs, nearly half of the NPs settled to the base of the substrate (Figure 3.2c). This observation indicates that high surface area (relative to the NPs to be deposited) of the NWs alone is not the determining factor to guarantee a well-dispersed loading. Directed assembly process mediated by NW one-dimensionality with a sufficient aspect ratio is what allows this simple drop-casting method to be useful.

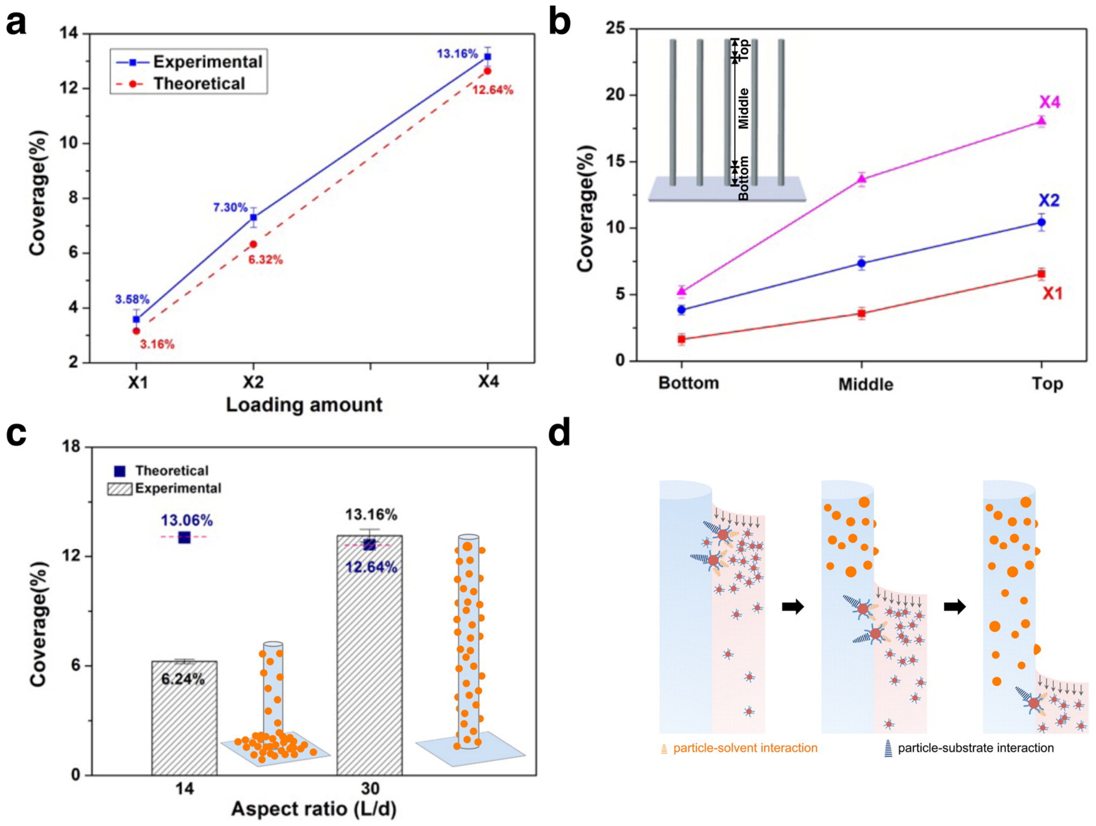

Figure 3.2. Quantitative analysis of NP assembly on NWs. Quantitative analysis of Au_3Cu NP assembly on (a,b) NW substrates with ×1, ×2 and ×4 loading amounts. Experimental determination of NP coverage (area fraction out of the total area provided) on NW surface is compared to the theoretical estimate assuming NPs are isolated and well-dispersed. The

numbers in (a) illustrate the overall coverage of Au_3Cu NPs on NW surface. Experimentally determined coverage is an average of multiple wires with each wire measured along its entire length. For (b), NP assembly was quantitatively analyzed by dividing each nanowire into multiple sections along its length. (c) Effect of NW aspect ratio on NP assembly. Aspect ratio is defined as the ratio of the NW length (L) to the diameter (d). In this case, length is the only variable while the diameter is kept the same. Error bars are from quantitative analysis of multiple wires throughout each substrate. (d) Schematic of directed NP assembly under NW geometry-guided solution drying and balanced interactions.

NPs being deposited onto the NWs while the liquid front moving implies an attractive interaction between the substrate surface (stationary phase) and the metal nanoparticles.[127] At the same time, a counteracting particle−solvent interaction should be present allowing NPs to stay in the solution (mobile phase). While the solution drying process is mediated by the NW substrate, a balance between these interactions at the microscopic level may also be critical.[128] To test this hypothesis, amount of surface ligands was tuned where less ligand would allow stronger interactions between the NP and the NW and vice versa. When the NPs were deprived of the ligands, identical loading procedure resulted in clustering and dense coverage at the top part of the wires with only few NPs from the middle to the bottom segment (Figure 3.3). In contrast, if more ligands were introduced, a large portion of the particles was found at the base of the substrate (Figure 3.3). These results indicate that with the balanced interactions present, one-dimensionality of the NW geometry facilitates the directed NP assembly by simply drop-casting a NP solution and letting it dry spontaneously (Figure 3.2d).

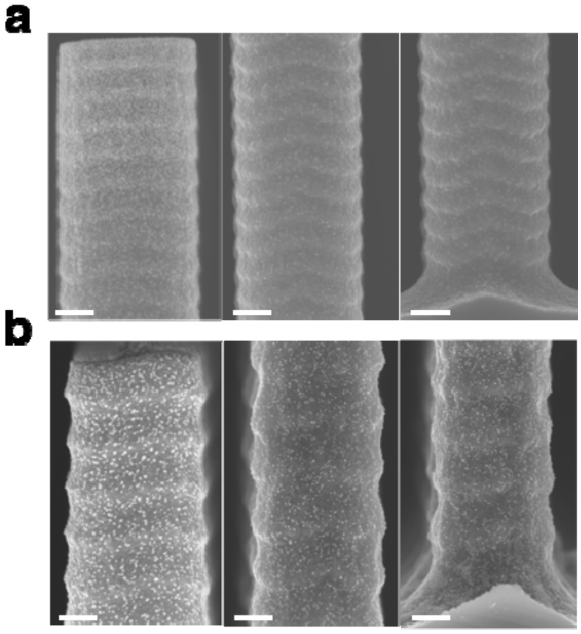

Figure 3.3. SEM images of Au$_3$Cu NP assembly on Si NW array substrate from top (left) to bottom (right) when ligand amount is varied. (a) Less ligand containing Au$_3$Cu NP solution drop-casted onto Si NW array. (b) More ligand containing Au$_3$Cu NP solution drop-casted onto Si NW array. The ligand amount is controlled by adding more washing steps or adding additional ligands without disturbing NP dispersion in solution. Scale bar is 200 nm.

3.1.2. Photoelectrochemical CO$_2$ reduction using NP/NW photoelectrodes

Light-driven CO$_2$ reduction on NP decorated PL and NW substrates was performed under 20 mW/cm^2 of 740 nm illumination to take into account CO$_2$ mass-transport limitations in CO$_2$-saturated 0.1 M KHCO$_3$ under standard conditions (Figure 3.4a). Under dark, both electrodes showed negligible current output. In contrast, greatly enhanced photocurrents were observed under illumination with both photoelectrodes exhibiting similar open-circuit voltage at around 0.25 V vs RHE, implying comparable photovoltage output. However, compared to the planar counterpart, NW substrate exhibited higher total current, which could be an indication of enhanced photoelectrochemical CO$_2$ reduction with lowered overpotentials (~130 mV difference at 1 mA/cm^2 compared with the planar counterpart). Detailed investigation of steady-state current densities (blue and red square symbols in Figure 3.4a for planar and NW photoelectrodes, respectively) also shows improved photocurrents of NW photoelectrodes compared to the planar counterpart.

As CO$_2$ reduction typically leads to various different products, the rate of individual product formation needs to be quantified to evaluate performance. Examination through gas chromatography and quantitative nuclear magnetic resonance spectroscopy on both types of photoelectrodes reveals CO as a major product. H$_2$ and a small amount of formate are detected as well. As shown in Figure 3.4a, NW photocathode exhibited faradaic efficiency (FE) of CO reaching close to 80% at only −0.20 V vs RHE (90 mV from the equilibrium potential for CO$_2$/CO), indicating 80% of the photogenerated charge extracted was used to selectively drive CO$_2$-to-CO conversion at the catalyst end. We also observed the FE reaching a peak and declining at moderate overpotentials, likely due to the limitations of CO$_2$ mass transport.[40] Partial current densities for CO (j_{CO}) were observed in the range from 2.2 to 3.8 mA/cm^2 for the NW photoelectrodes in between −0.20 V to −0.37 V vs RHE (Figure 3.4b), exhibiting an average enhancement factor of 2.8 compared to the planar counterpart showing j_{CO} from 0.6 to 1.8 mA/cm^2 within the same potential range. In other words, when evaluated in terms of additional bias (overpotential) needed to drive CO$_2$-to-CO conversion, NW photoelectrodes required less overpotentials (~120 mV lower) compared to the planar photoelectrodes. The NW geometry allows decreasing the photogenerated electron flux (Flux$_{e-}$) over its large surface area (Figure 3.4c), alleviating the turnover requirement of the loaded catalyst and consequently reducing the necessary overpotential.[129] Compared to the planar substrate, NW array with high roughness factor in this work allows Flux$_{e-}$ dilution by 14.25 times, when considering its entire surface area, as presented by the dotted lines in Figure 3.4c.

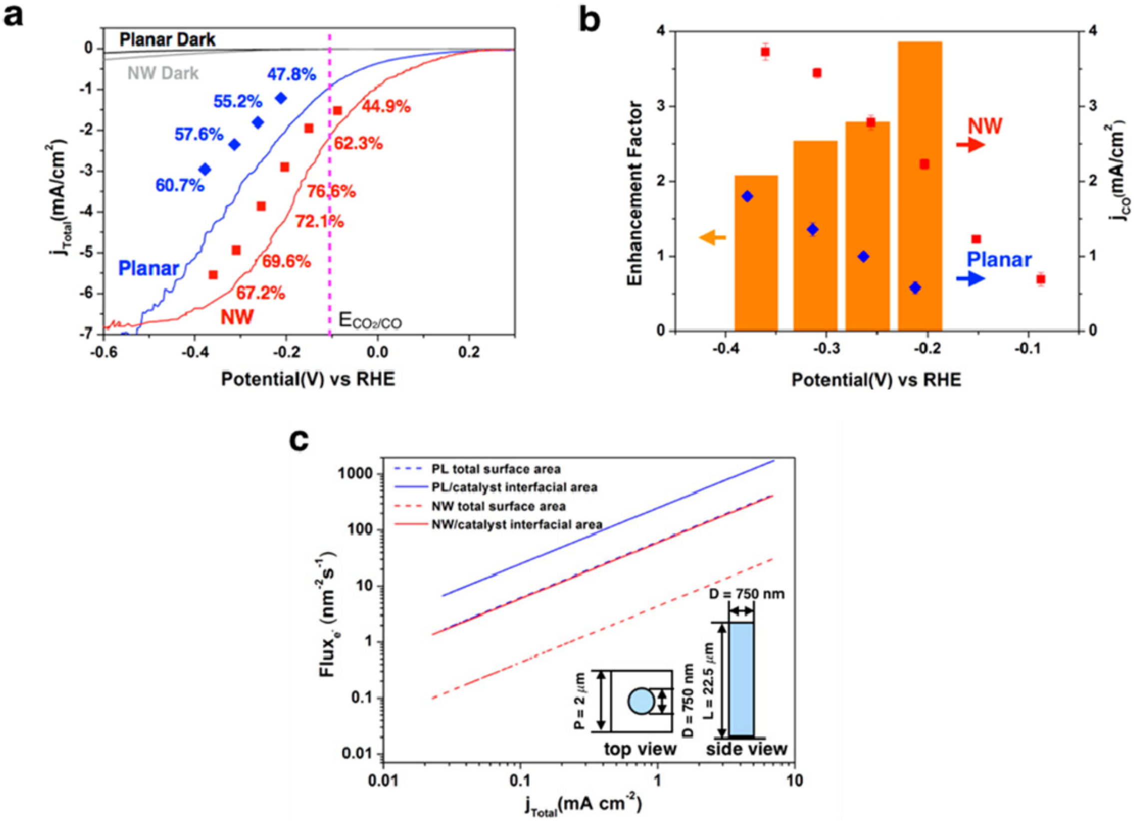

Figure 3.4. Photoelectrochemical reduction of CO_2 using integrated photoelectrodes. (a) Comparison between Au_3Cu NP assembled Si PL and NW photoelectrodes in catalytic activity and FE for CO_2 conversion to CO. Solid lines present linear sweep voltammetry (10 mV/s) of both substrates under dark and under illumination. Each point represents total current density from the geometric area of the photoelectrodes during chronoamperometry and the numbers indicate faradaic efficiency toward CO. (b) Partial current density for CO generation of Au_3Cu NP assembled substrates and enhancement of NW over PL for comparison. All the measurements were under 20 mW/cm^2 of 740 nm illumination (calibrated with standard Si photodiode) with photon flux above silicon band gap comparable to one-third of that obtained from 100 mW/cm^2, air mass 1.5 solar illumination to take into account CO_2 mass-transport limitations in 0.1 M $KHCO_3$ (pH = 6.8) at 1 atm CO_2 and room temperature. Error bars at each potential are based on multiple measurements. (c) Estimation of photogenerated electron fluxes (Flux$_{e-}$) over the output current range on both substrates. Flux$_{e-}$ considering substrate total surface area (dashed line) and substrate/catalyst interfacial area (solid line) are both calculated. The flux$_{e-}$ considering PL total surface area around the saturated photocurrent (～430 electrons/(nm^2·s)) matches well with the typical value of planar n$^+$p-Si (～1200 electrons/(nm^2·s) under one-sun illumination and corrected by photon flux used in this work.). When considering the real interfacial area determined by NP assembly on both substrates, quantitative analysis of NP coverage (7.30% and 24.9% on NW and PL, respectively) is used. The inset shows NW substrate dimensions used for calculation.

This is, however, the idealized case, and to benefit the most from having a high surface area light-harvesting support when catalysts are spatially coupled, the interfaced catalysts have to be well-dispersed across the entire surface so that a large contact area is formed to distribute the electron flux, together with a large number of active sites exposed for catalytic turnover. When the real interfacial area determined by NP assembly on both photoelectrodes (with coverage values 7.30% and 24.9% on the NW and PL, respectively) is considered, it is also clear that NWs were favorable in this aspect by directing uniform assembly of nanoparticle catalysts from its one dimensionality, which resulted in a consistently reduced Flux_{e-} by a factor of 4 with catalytic sites exposed to the largest degree in comparison to that of the planar (solid lines in Figure 3.4c). To be specific, in the case of maximal photogenerated electron extraction, the NP assembled NW photoelectrode exhibited reduced Flux_{e-} of 414 electrons/($\mathrm{nm}^2\cdot\mathrm{s}$) compared to that of the PL substrate with 1753 electrons/($\mathrm{nm}^2\cdot\mathrm{s}$). In addition, the effect of reduced overpotentials from electron flux dilution is further enhanced when the reaction under interest is sluggish with slow turnover and the relative increase in turnover is less per added overpotential. This is indeed the case for CO_2 reduction that requires greater amount of overpotential for turnover increase, especially in the operational current region for solar-to-fuel conversion to be practical. Therefore, NW photoelectrodes are clearly advantageous in reducing overpotential for CO_2 reduction compared to the well-known proton reduction, by allowing each catalyst to operate at a diluted electron flux. From the performance observed, we could see that the NW, as a light absorber, has allowed effective charge transport to the assembled NPs for CO_2 reduction without disturbing their inherent catalytic activity. More importantly, by utilizing the unique value of one-dimensionality present in the NW system that allowed uniform assembly, target products could be effectively gained with decrease of electrocatalysis losses in the form of kinetic overpotentials.[130]

The integrated system was tested for an extended period of 18 hours (Figure 3.5a). As shown, with minimal change in current density, CO was maintained as a major product during continuous operation exhibiting long-term capability for photoelectrochemical CO_2 reduction. Furthermore, we tried to see if a third component could be incorporated to enhance the photoelectrochemical performance. Using the identical drop-casting approach, the addition of 1-butyl-3-methylimidazolium tetrafluoroborate (BMIM-BF_4)[85] can further enhance the CO selectivity in the low overpotential region, with FE rising from 44.9% to 64.2% at −0.09 V vs RHE (Figure 3.5b). The adsorption of BMIM-BF_4 on NP catalyst surface allows lowering the energy barriers for CO_2 reduction by complexation with the CO_2 reduction intermediate, thereby leading to favorable charge transport toward CO_2 reduction rather than competing hydrogen evolution. This further illustrates how combining multiple components using the simple method described here could be effective for artificial photosynthesis.

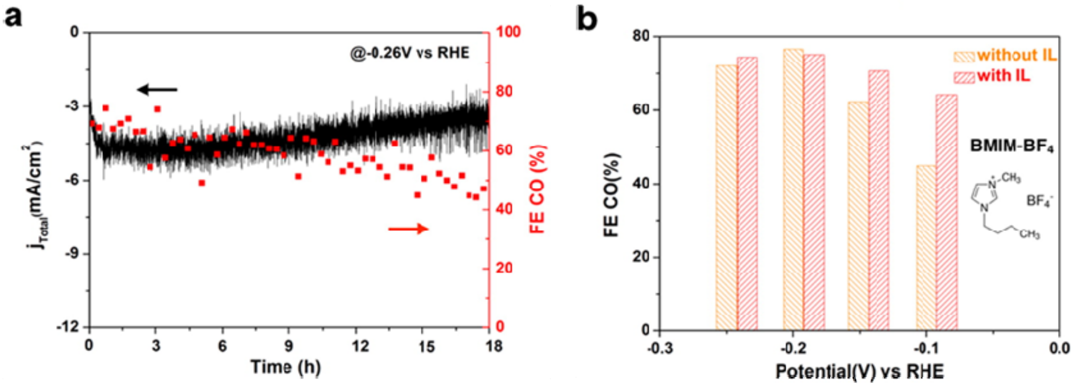

Figure 3.5. Photoelectrochemical performance in the long term and incorporating ionic liquid as a third component. (a) CO_2 reduction activity of Au_3Cu NP/Si NW photoelectrode for 18 h. Total current density and FE for CO at −0.26 V vs RHE. (b) Potential-dependent CO FEs of Au_3Cu NP/Si NW photoelectrode incorporating ionic liquid BMIM-BF_4. All the data were obtained in CO_2-saturated 0.1 M $KHCO_3$ under standard conditions (pH = 6.8).

3.1.3. Conclusions

Beyond the already proven benefits of Si NWs as an attractive material for photoelectrochemical applications, here, we have shown an additional advantage of the one-dimensional geometry allowing a simple and effective integration process for photoelectrochemical reduction of CO_2. The assembly process demonstrated shows that Si NWs have the potential to perform as a general platform for interfacing a wide range of CO_2 reducing NP catalysts for light-driven applications. As part of the process in constructing a sophisticated system of optimized components, this approach will facilitate the advances of artificial photosynthesis combining synthetic nanoparticle catalysts.

3.2. Plasmon-enhanced photocatalytic CO_2 conversion using Ag-MOF nanoparticles

Besides having the direct role of providing surface sites for catalytic transformation reactions, nanoparticles can also be used for secondary effects such as enhancing the catalytic activity of other materials. Here, a metal−organic framework (MOF)-coated nanoparticle photocatalyst with enhanced CO_2 reduction activity and stability is discussed. This composite structure contains multiple functional units where the molecular Re complexes inside the MOF are the active sites for CO_2 photoreduction and the Ag nanoparticles enhance their catalytic activity by the plasmonic effects. In addition, the MOF provides a molecular environment that can optimize the catalytic behavior of the photoactive complexes. The catalysts' unique performance is attributed to the precision and systematic variation applied in their design and the high spatial resolution at which multiple materials are interfaced.

3.2.1. Synthesis of the photoactive Re complex containing MOFs

Specifically, we covalently attached $Re^{I}(CO)_3(BPYDC)(Cl)$, BPYDC = 2,2′-bipyridine-5,5′-dicarboxylate [hereafter referred to as ReTC], within a zirconium MOF based on the UiO-67-type structure[131] (hereafter, this Re-containing MOF is termed Re_n-MOF) and controlled its density in the pores in successive increments of n (n =0, 1, 2, 3, 5, 11, 16, and 24 complexes per unit cell). To determine the general structure of Re_n-MOFs, single-crystal X-ray diffraction was employed on Re_3-MOF. Single crystals of Re_3-MOF were prepared by dissolving the protonated form of H_2ReTC (20 mol %), H_2BPDC (80 mol %, BPDC = 4,4′-biphenyldicarboxylate), and $ZrOCl_2·8H_2O$ in a solution mixture of DEF/formic acid in a 20 mL screw-capped vial and heating at 140 °C for 12 h. The analysis of single-crystal X-ray diffraction data reveals that Re_3-MOF crystallizes in the cubic Fm-3m space group with a unit cell parameter a = 26.7213(8) Å (Figure 3.6). Each Zr secondary building unit, $Zr_6O_4(OH)_4(-CO_2)_{12}$, is coordinated to a total of 12 linkers (ReTC and BPDC), resulting in a three-dimensional fcu network. Inductively coupled plasma atomic emission spectroscopy (ICP-AES) analysis performed on these crystals gave a molar ratio of 0.12 mol of Re to 1 mol Zr. This corresponds to 3 ReTCs per unit cell (*i.e.*, Re_3-MOF), as confirmed by the X-ray structure of single-crystalline $Zr_6O_4(OH)_4[Re(CO)_3(Cl)\text{-}BPYDC]_{0.72}(BPDC)_{5.28}$, where covalently bound ReTCs are found in octahedral cavities of face-centered cubic arrangement. Moreover, chloride occupies the axial position and was refined from the Fourier difference map, indicating *fac*-arrangement of the ReTC in Re_3-MOF, which is an identical geometry compared to that of the mononuclear Re complex in solution.[132]

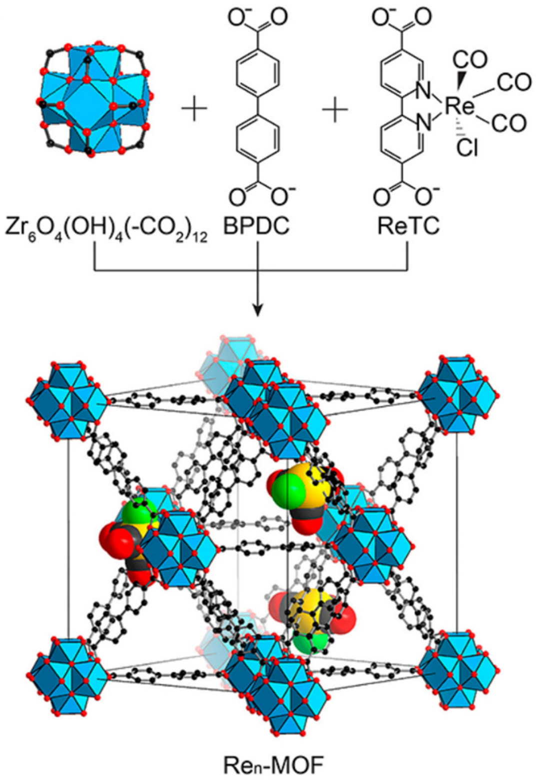

Compound	Re3-MOF
chemical formula	$C_{92.88}H_{28}Cl_{0.72}N_{5.52}O_{36}Re_{0.78}Zr_6$
formula mass	2515.13
crystal system	cubic
space group	*Fm-3m*
λ (Å)	0.7749(1)
a (Å)	26.7213(8)
Z	4
V (Å^3)	19079.8(17)
temperature (K)	100(2)
size /mm	0.020 x 0.020 x 0.020
density (g/cm^{-3})	0.876
measured reflections	51150
unique reflections	782
parameters	70
restraints	4
R_{int}	0.1671
θ range (deg)	2.35-25.91
R_1, wR_2	0.0631, 0.2292
S (GOF)	1.185
max/min res. dens. (e/Å^3)	1.38/-0.65

Figure 3.6. Structures of Re_n-MOF determined from single-crystal X-ray diffraction of Re_3-MOF. $Zr_6O_4(OH)_4(-CO_2)_{12}$ secondary building units are combined with BPDC and ReTC linkers to form Re_n-MOF. The 12-coordinated Zr-based metal clusters are interconnected by 21 BPDC and 3 ReTC linkers in a face-centered cubic array. Atom labeling scheme: C, black; O, red; Zr, blue polyhedra; Re, yellow; Cl, green; H atoms are omitted for clarity.

The *fac*-arrangement of ReTC in Re_3-MOF is also supported by infrared (IR) spectroscopy, UV-vis spectroscopy, and ^1H nuclear magnetic resonance (NMR) spectra (Figure 3.7). The IR spectrum of Re_3-MOF was measured in powder form, and *v*(CO) bands were observed at 2022, 1920, and 1910 cm^{-1}, consistent with the *fac*-isomer of molecular ReTC.[132] The UV-vis spectrum, measured as a powder mixed with KBr, has a metal-to-ligand charge transfer (MLCT) absorption band at 400 nm, indicative of the *fac*-isomer of ReTC.[132] The amount of ReTC in the MOF and its molecular configuration were further confirmed from ^1H NMR of a HF-digested solution of Re_3-MOF (Figure 3.7c).

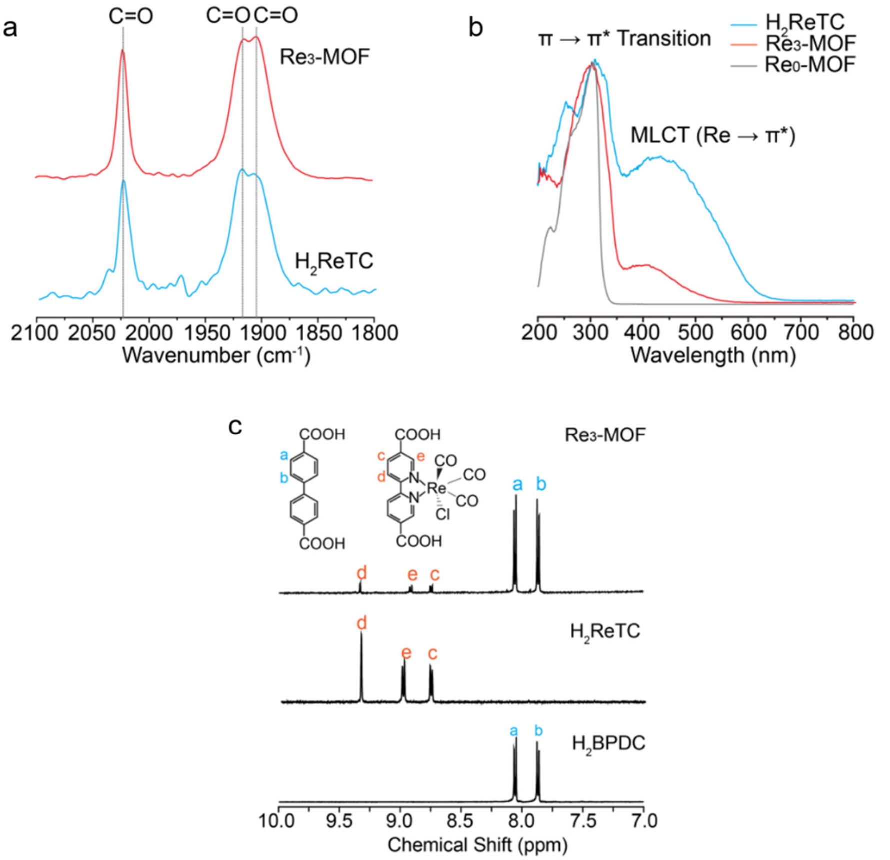

Figure 3.7. *fac*-arrangement of ReTC in Re_3-MOF. (a) Infrared (IR) spectra of Re_3-MOF and H_2ReTC. (b) Ultraviolet-visible (UV-Vis) spectra of Re_3-MOF, Re_0-MOF and H_2ReTC. (c) ^{1}H NMR spectra of Re_3-MOF (top), H_2ReTC (middle), and H_2BPDC (bottom).

With the crystal structure confirmed, the ReTC density was varied in the range from Re_0-MOF (ReTC free MOF) to Re_{24}-MOF (ReTC at maximal loading). This was done by adding increasing amounts of H_2ReTC to the total amount of organic linkers during MOF synthesis, which resulted in Re_n-MOFs (n = 0, 1, 2, 3, 5, 11, 16, and 24) identified from ICP-AES (Figure 3.8a). Representative SEM images (Figure 3.8b) of Re_n-MOFs show great size uniformity and identical octahedral geometry of particles regardless of the amount of ReTC incorporated. The crystallinity of Re_n-MOFs was examined by PXRD (Figure 3.8c), which gave sharp diffraction lines matching those of the simulated pattern obtained from experimental single-crystal X-ray diffraction data of Re_3-MOF. This clearly indicates preservation of the single-crystalline Re_3-MOF structure upon introduction of different density of ReTC in Re_n-MOFs. The permanent porosity of all Re_n-MOF samples was confirmed by measurement of their N_2 sorption isotherms (Figure 3.8d). UV−vis spectroscopy for all Re_n-MOFs (Figure 3.8e) showed that the MLCT absorption band intensities increase as more ReTCs are incorporated into the framework, further confirming the varied density of the photoactive units in Re$_n$-MOFs.

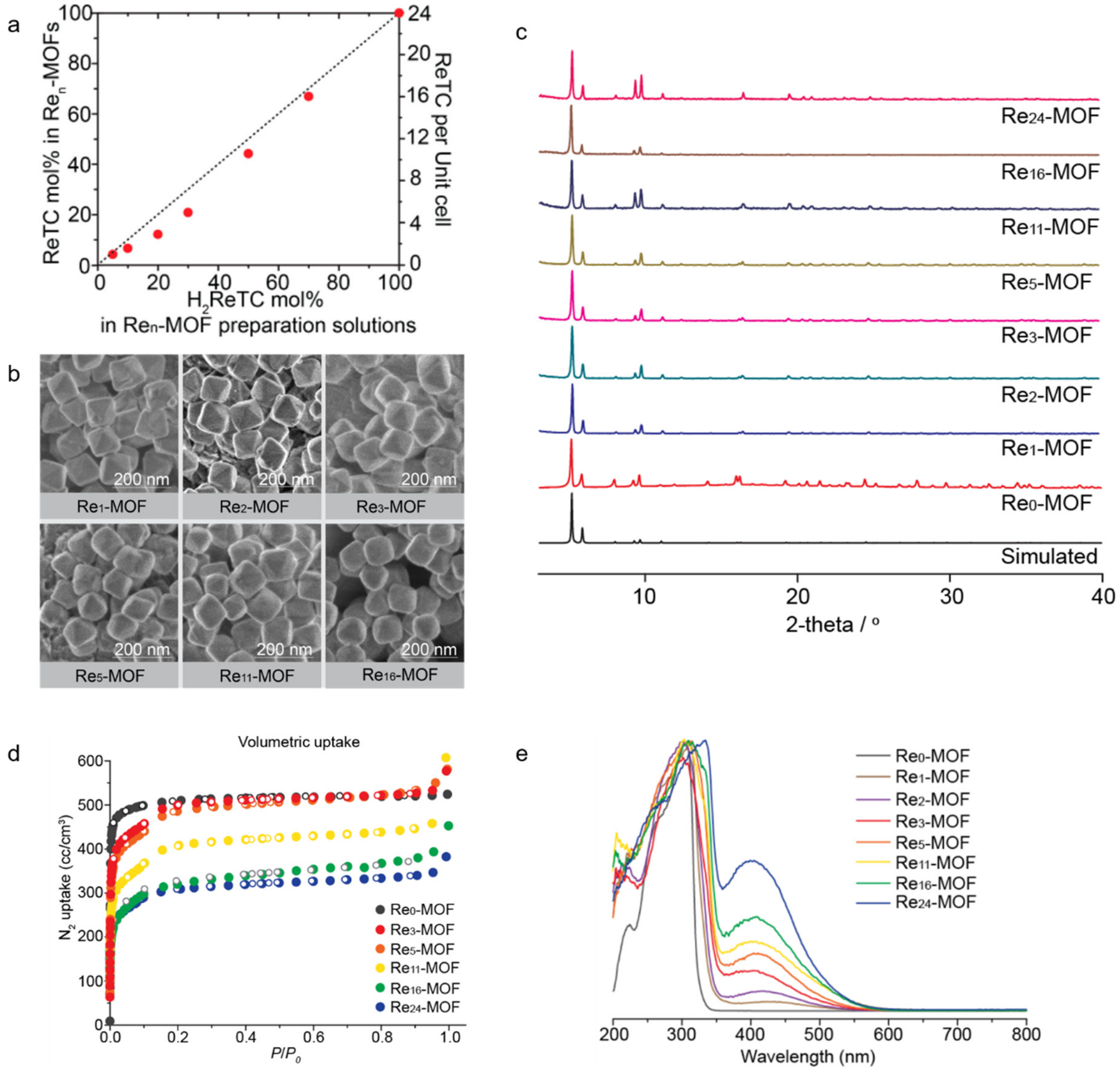

Figure 3.8. Characterization of Re$_n$-MOFs. (a) Percent incorporation of ReTCs in Re$_n$-MOFs. (b) SEM images for Re$_n$-MOFs. (c) PXRD of Re$_n$-MOFs. (d) N_2 sorption isotherms for Re$_n$-MOFs at 77 K with adsorption and desorption points represented by closed and open circles, respectively (*P*/*P*$_0$, relative pressure). (e) UV-Vis spectra of Re$_n$-MOFs.

3.2.2. Photocatalytic CO_2 conversion of Re_n-MOFs

All Re_n-MOFs used for photocatalytic CO_2 conversion were dispersed in an acetonitrile/triethylamine mixture (MeCN/TEA = 20:1) saturated with CO_2, where TEA served as a sacrificial electron donor. Measurements were conducted under visible light (300W Xe lamp, visible band-pass = 400-700 nm) to utilize the visible light absorption feature of ReTC. We note this is in contrast to previous work where it relied on the intense absorption at the UV region (300−350 nm) associated with π−π* energy transition of the bipyridine linker.[133,134] The products were analyzed and quantified using gas chromatography and normalized to the number of ReTC in Re_n-MOFs to get the turnover number (TON). Photocatalytic CO_2-to-CO conversion behavior of Re_n-MOFs is shown in Figure 3.9, reaching peak activity with Re_3-MOF. In the absence of CO_2 (under Ar atmosphere) or with no ReTC, there was no CO generation observed. The performance of Re_n-MOFs was stable at least up to 4 h compared to the molecular counterpart,[135] which deactivates within the first hour. The enhanced stability of Re_n-MOFs is from the covalent attachment of Re centers in ReTC, which prevents the prevailing deactivation pathway of dimerization commonly observed with photoactive molecular complexes. IR spectra of Re_3-MOF before and after the reaction (Fig. 3.9b) show that Re_n-MOFs preserve the molecular configuration of *fac*-ReTC after photocatalysis, while, in comparison, the ν(CO) bands for molecular H_2ReTC are shifted because of dimerization. This clearly indicates the inability of ReTC to dimerize due to its covalent bonding to the MOF in Re_n-MOFs.

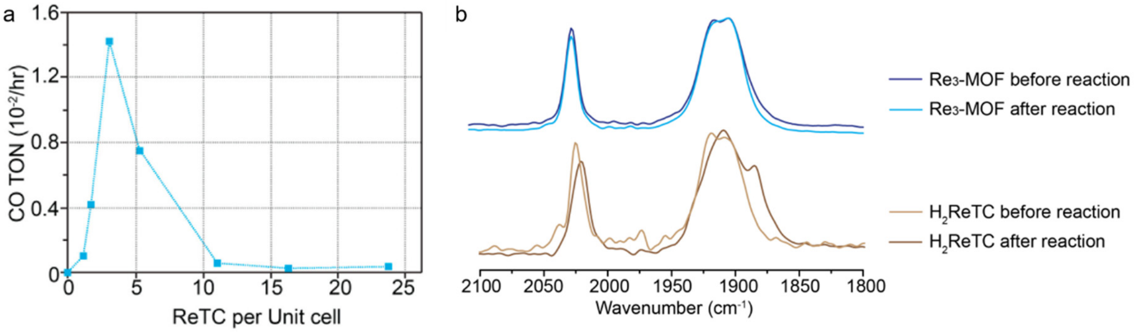

Figure 3.9. Photocatalytic activity of Re_n-MOFs. (a) CO turnovers under visible light (400−700 nm). (b) IR spectra of Re_3-MOF and H_2ReTC before and after photocatalysis.

The photocatalytic trend observed for Re_n-MOFs should be closely related to the configuration of ReTC and its surrounding environment. The vibrational stretching modes of ReTC carbonyl ligands in Re_n-MOFs were probed by IR spectroscopy and compared with those of the molecular H_2ReTC (Figure 3.10). In the cases of Re_1-, Re_2-, and Re_3-MOFs, ν(CO) bands were observed at 2022, 1920, and 1910 cm^{-1}, which are identical to the IR spectra of H_2ReTC dispersed in solution. On the other hand, the ν(CO) bands at lower wavenumbers were shifted to lower frequency for Re_5-, Re_{11}-, Re_{16}-, and Re_{24}-MOFs. This indicated that there is electron back-donation to the carbonyl ligand from Re of other ReTCs, weakening the CO bond strength.[136] This effect is possibly due to weak interactions between contiguous overlapping ReTCs. This was also observed when H_2ReTC molecules are tightly packed as powder and moistened with acetonitrile, where *v*(CO) bands are shifted to 1900 and 1880 cm^{-1}.

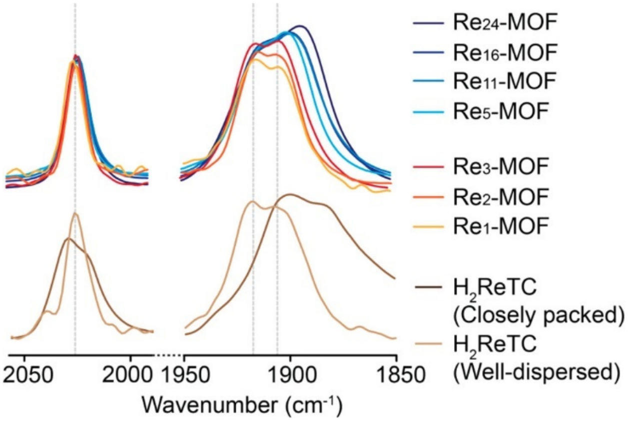

Figure 3.10. IR spectra of Re_n-MOFs and H_2ReTC.

Considering that ReTCs are observed within the octahedral cavity of Re_3-MOF from single-crystal X-ray diffraction and the axial rotation of the ReTC linker backbone, the maximum number of ReTC units that can be incorporated into Re_n-MOF without overlapping is 4 per unit cell, with each octahedral cavity being occupied with a single ReTC complex (Figure 3.11a). We believe a statistically variable distribution of ReTCs within the framework is most reasonable to expect. Beyond this point, the likelihood of ReTCs occupying adjacent linkers and hence overlapping increases. Indeed, if the linkers can rotate 180° into adjacent octahedral cavities, beyond 4 per unit cell, there will unavoidably be some ReTCs clashing from this rotation (Figure 3.11b). The IR spectra are consistent with the unit cell structure considerations where Re_5-MOF is just beyond the limit of ReTC being undisturbed. Therefore, the excessive occupation of ReTCs in Re_n-MOFs appear to cause a change in their vibrational state,[137] which may not be favorable for reducing CO_2 and decreases activity for Re_n-MOFs with n greater than 4. Another aspect to note is the accessible pore volume of Re_n-MOFs: N_2 uptake on a volumetric scale (Figure 3.8d) is lower for frameworks with more than 4 ReTC per unit cell. This indicates that substrate and product diffusion may also be limited within Re_n-MOFs with n greater than 4, further resulting in the observed lowering of activity.

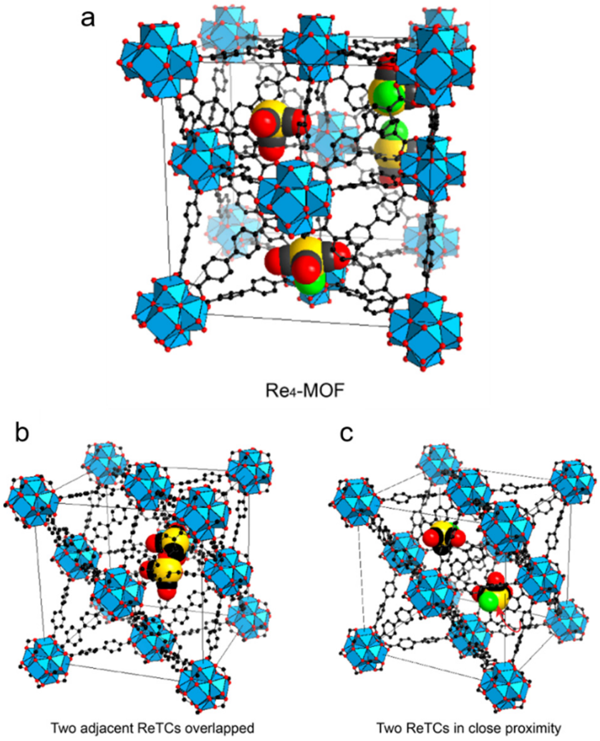

Two adjacent ReTCs overlapped

Two ReTCs in close proximity

Figure 3.11. Unit cell structures of Re$_n$-MOFs. (a) Structural model of Re$_4$-MOF with each octahedron pore being occupied with a single ReTC complex (4 ReTCs per unit cell). Structural models showing ReTCs (b) overlapping when $n > 4$ on adjacent linkers and (c) in close proximity by their free rotation allowing a bimolecular reaction pathway to occur when $n < 4$, with ReTCs on opposite linkers but in the same octahedral cavity. Other ReTCs beside those presented in (b) are omitted for clarity.

However, we see an increase in activity in the lower regime of ReTC incorporation, from Re$_1$ to Re$_3$. Though a unimolecular pathway has been reported to exist for molecular ReTC,[138] the observed rise in photocatalytic activity with more ReTC units within Re$_n$-MOF ($n < 4$) implies that the bimolecular reaction pathway (bridging or outer-sphere electron transfer) is the source of the higher turnover,[137–141] which is expected for a reaction involving 2 electrons (Figures 3.11c). Therefore, a fine balance of proximity between photoactive centers is needed for such cooperatively enhanced activity. Furthermore, reduced activity compared to the molecular ReTC in solution indicates that restricting the free motion of the molecular complex may limit its activity though it is protected from rapid deactivation. The present study of Re$_n$-MOFs not only elucidates the effect of the molecular environment within MOFs for photocatalytic CO_2 reduction but also provides further insights into the photocatalytic reaction pathway of molecular ReTC.

3.2.3. Plasmon-enhanced photocatalytic activity of Re$_n$-MOFs coated on plasmonic Ag nanocubes

Coupling Re$_3$-MOF to a plasmonic Ag nanoparticle was performed to demonstrate an effective strategy in creating a bifunctional catalyst with enhanced activity and long-term stability. The optimal Re$_3$-MOF structure with the highest turnover was coated on Ag nanocubes (Ag$\subset$Re$_3$-MOF). Once irradiated with light, the Ag nanocubes generate intensified near-surface electric fields at their surface plasmon resonance frequency that can be orders of magnitude higher in intensity than the incident electromagnetic field.[142] Therefore, it is expected that Re$_3$-MOF coating on the Ag nanocubes can spatially localize photoactive Re centers to the intensified electric fields with enhanced photocatalytic activity. Ag nanocubes prepared by the polyol process[143] were used in the synthesis procedure of Re$_n$-MOF to give Ag$\subset$Re$_3$-MOF. Figure 3.12a shows a TEM image of Ag$\subset$Re$_3$-MOFs. The dark area in the core is the Ag nanocube (98 nm in size), and the brighter outer part is the Re$_3$-MOF with a thickness of 33 nm. The magnified image of the outer part (Figure 3.12b) shows lattice fringes from the crystalline Re$_3$-MOF layer. ICP-AES analysis revealed that the Re$_3$-MOF layer contains the expected three ReTCs per unit cell. The crystallinity of Ag$\subset$Re$_3$-MOF was examined by PXRD, confirming the Re$_3$-MOF structure on the surface of Ag (Fig. 3.12c). The permanent porosity of Ag$\subset$Re$_3$-MOF was confirmed by N_2 sorption and IR spectroscopy showed ν(CO) consistent with those of molecular H_2ReTC and Re$_3$-MOF (Fig. 3.12d). From the UV−vis spectrum (Fig. 3.12e), the Ag nanocube exhibits a strong quadrupolar localized surface plasmon resonance (LSPR) scattering peak (λ_{max} ~480 nm),[143,144] which overlaps with the absorption range of ReTC (400 nm < λ < 550 nm) in the visible region. Furthermore, the Ag$\subset$Re$_3$-MOF structure retains the characteristic LSPR features of the Ag core after being coated with the Re$_3$-MOF. Therefore, it is expected that the intensified near-field created at the surface of Ag nanocubes can be absorbed by ReTCs incorporated into the Re$_3$-MOF layer for photocatalytic enhancement.

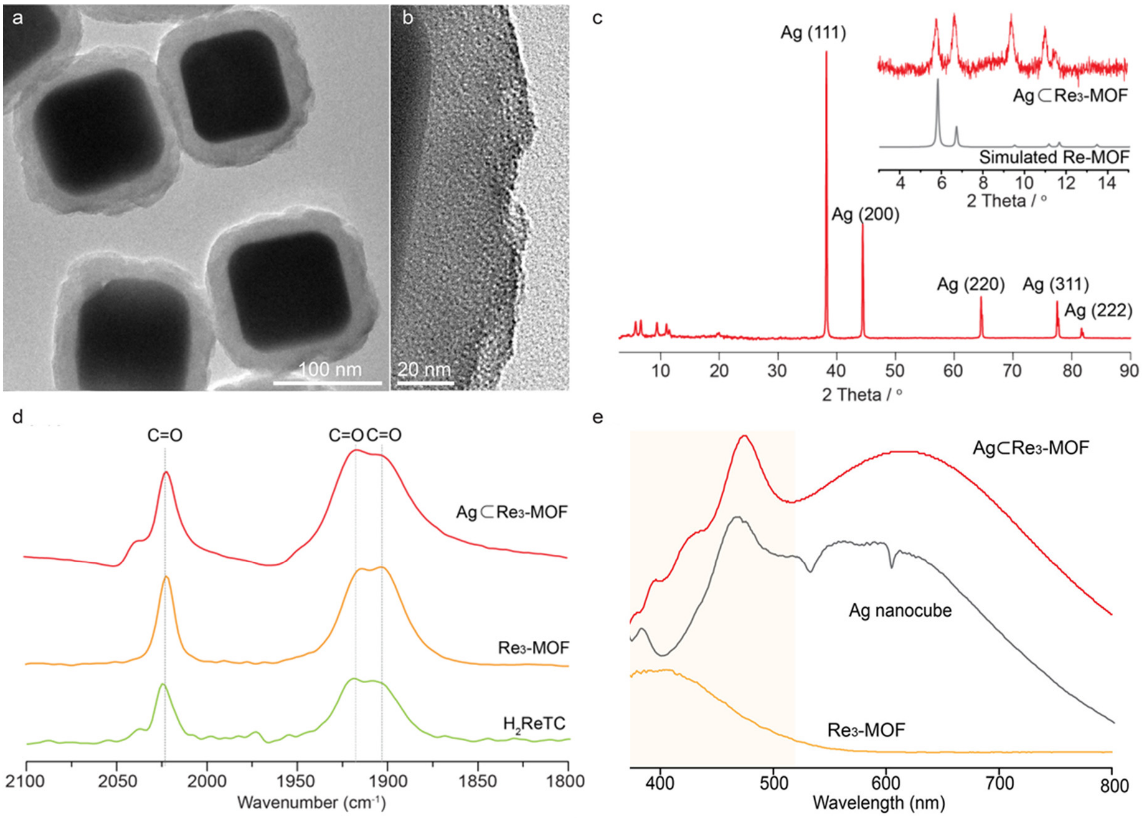

Figure 3.12. Characterization of Ag$\subset$Re$_3$-MOF. (a) TEM image of Ag$\subset$Re$_3$-MOF showing Re$_3$-MOF constructed on the surface of Ag nanocubes. (b) Magnified image of Re$_3$-MOF. (c) PXRD of Ag$\subset$Re$_3$-MOF. (d) IR spectra of Ag$\subset$Re$_3$-MOF, Re$_3$-MOF and H$_2$ReTC. (e) UV−vis spectra of Re$_3$-MOF, Ag nanocube, and Ag$\subset$Re$_3$-MOF.

Photocatalytic CO$_2$-to-CO conversion activity of Ag$\subset$Re$_3$-MOF was performed under conditions identical to those expressed above (Figure 3.13a). As expected, Ag$\subset$Re$_3$-MOF exhibits 5-fold enhancement of activity over Re$_3$-MOF under visible light. Since the intensity of the near-field from LSPR decays exponentially with the distance from the surface of the nanoparticle,[145] ReTCs in a thinner MOF layer will be under the influence of a stronger electric field on average, leading to superior turnover. A thinner Re$_3$-MOF layer (16 nm) was coated on Ag nanocubes by controlling the synthetic conditions, and this structure provided 7-fold enhancement of photocatalytic activity (Figure 3.13a). When there was no ReTC in the MOF layer (*i.e.*, Ag$\subset$Re$_0$-MOF), there was no activity observed, ruling out the possibility of Ag being responsible for CO production. Additionally, when Re$_2$-MOF was coated on Cu nanoparticles of similar size (~100 nm), activity enhancement was not observed (Figure 3.13a) as the Cu nanoparticles do not have LSPR characteristics that match the absorption features of ReTC.

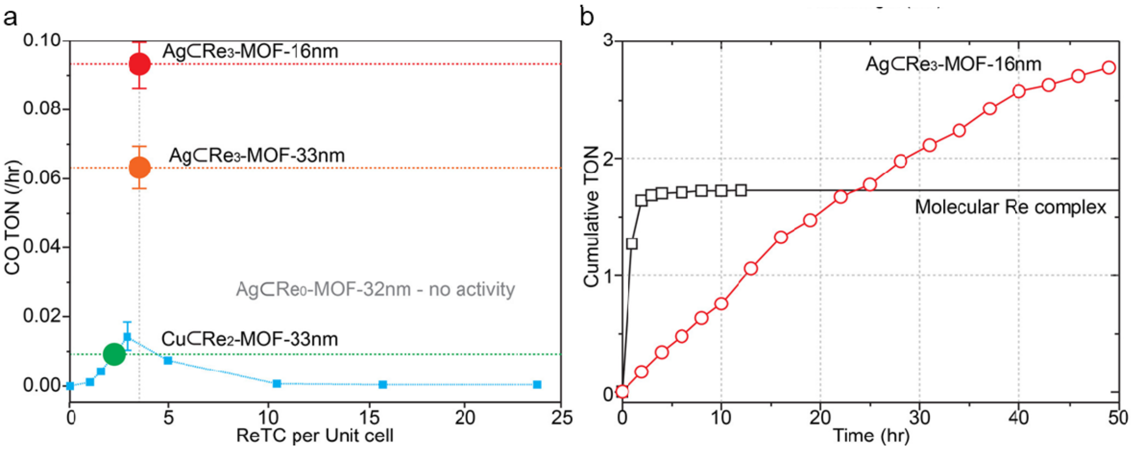

Figure 3.13. Photocatalytic activity of Ag⊂Re$_3$-MOF. (a) Photocatalytic CO$_2$-to-CO conversion activity of Re$_n$-MOFs (blue line), Ag⊂Re$_0$-MOF, Cu⊂Re$_2$-MOF, and Ag⊂Re$_3$-MOFs with MOF thickness of 16 and 33 nm. (b) Stable performance of Ag⊂Re$_3$-MOF compared to molecular H$_2$ReTC.

The Ag nanocube coated with Re-MOF should exhibit not only enhanced photocatalytic activity but long-term stability as well from having ReTCs covalently bound within the MOF. The stability of the Ag⊂Re$_3$-MOF structure was tested by measuring its activity up to 48 h under visible light (Figure 3.13b). Compared to molecular H$_2$ReTC, which rapidly deactivates within the first hour possibly from dimerization as previously reported,[135] Ag⊂Re$_3$-MOF shows stable photocatalytic performance throughout the entire period, and its cumulative TON exceeds that of H$_2$ReTC after 24 h. The stability of the structure was confirmed with TEM and IR spectroscopy following the long-term measurement. The CO produced from Ag⊂Re$_3$-MOF almost doubled from that of H$_2$ReTC after 48 h, demonstrating the combined effects gained from this bifunctional catalyst construct.

3.2.4. Summary

We show how covalently attached photoactive centers within MOF interior can be spatially localized and subjected to the enhanced electromagnetic field surrounding plasmonic silver nanocubes to significantly increase their photocatalytic activity. We covalently attached Re$^{\mathrm{I}}$(CO)$_3$(BPYDC)Cl, BPYDC = 2,2′-bipyridine-5,5′-dicarboxylate, into a zirconium MOF, UiO-67, and controlled its density in the pores in increments (0, 1, 2, 3, 5, 11, 16, and 24 complexes per unit cell), which led to observing the highest activity for three complexes. This activity trend resulted from the molecular environment within MOFs that varied with ReTC density. Placing the optimal Re$_3$-MOF structure with the highest turnover on silver nanocubes resulted in 7-fold enhancement of photocatalytic activity under visible light.

Chapter 4

Structural dynamics of nanoparticle catalysts

Reproduced with permission from "Kim, D., Becknell, N., Yu, Y. & Yang, P. Room-Temperature Dynamics of Vanishing Copper Nanoparticles Supported on Silica. Nano Lett. ***17,*** *2732–2737 (2017)." Copyright 2017 American Chemical Society.*

Reproduced with permission from "Kim, D., Kley, C. S., Li, Y., & Yang, P. Copper Nanoparticle Ensembles for Selective Electroreduction of CO_2 *to* C_2*-*C_3 *products. Proc. Natl. Acad. Sci. U. S. A.* ***114,*** *10560-10565 (2017).".*

One important aspect that often has not been thoroughly considered in catalysis is the dynamic behavior of nanomaterials induced from their increased energetics, especially under operating conditions. It can result in unexpected changes to the nanoparticle morphology or atomic structure and interactions between nanoparticle and support that the commonly perceived static view of nanoparticle systems to describe their properties may be far from accurate. Here, the recent discoveries related to the nanoparticle-support interactions under ambient conditions and the dynamic structural transformation of nanoparticles favorable for CO_2 electrocatalysis will be discussed.

4.1. Room-temperature dynamics of vanishing copper nanoparticles supported on silica

Supported nanoparticles are the basis of heterogeneous catalysis, where a wide range of essential processes, such as fuel/chemical production and pollutant mitigation, are conducted.[146] The use of nanoparticles requires high surface supports to finely disperse them to take advantage of their nanoscale dimensions. However, it has also been suggested that supports can play a more active role in dictating catalytic properties of a nanoparticle system by creating a functional interface. For instance, the catalytically active sites could be mainly located at the interface between the nanoparticle and support, where both participate at the junction to favorably bind the reactants and intermediates for catalytic conversion.[147–149] Furthermore, supports can strongly anchor nanoparticles to resist sintering[150] and catalytic behavior can also be tuned by charge transfer between nanoparticle and support.[151] Therefore, both the nanoparticle and support need to be considered together to evaluate the state and properties of the system for its primary function.

In this regard, dynamic atomic interactions between the nanoparticle and support that could result from the increased energetics at the nanoscale[152] need to be considered. The interactions within a supported nanoparticle system could be significant enough to drastically change the state of the system from what is expected.[153] Because nanoscale matter possesses far different energetics from its bulk counterpart, the atomic interactions between the nanoparticle and support may take place even under ambient conditions as well. Understanding these interactions will be critical in identifying new types of materials and solving unresolved issues at a more fundamental level that will allow nanomaterials to reach their utmost potential in the relevant fields.

In this work, we have studied the dynamic behavior of copper nanoparticles on silica which is a well-known support for nanoparticle loading, under ambient conditions. This study identifies for the first time the dynamic interaction between nanoparticle and support at room temperature, which led to a surprising discovery: complete disappearance of the silica-supported copper nanoparticles under ambient conditions.

4.1.1. Observation and kinetic analysis of disappearing copper nanoparticles

The vanishing of copper nanoparticles was accidentally discovered when we attempted to load ligand-removed copper nanoparticles onto uniform, amorphous silica submicrospheres (loading amount 0.74 $\mathrm{mg_{Cu}/g_{Silica}}$). The shrinkage and ultimate disappearance of Cu nanoparticles (6−7 nm) was observed at room temperature and ambient atmosphere. Ten days after the nanoparticles were initially loaded, only small traces of them could be observed using TEM (Figure 4.1a). Three weeks after loading, Cu nanoparticles could no longer be found. HAADF-STEM images of as-loaded Cu nanoparticles on silica (Figure 4.1b) showed bright intensity originating from Cu nanoparticles over a less-intense background of a silica sphere. However, the bright signal from the nanoparticles was no longer there after 3 weeks and aberration-corrected HAADF-STEM confirmed the complete loss of the nanoparticles (Figure 4.2). With increased loadings of Cu nanoparticles on silica, a similar trend was observed as well. In addition, elemental analysis of Cu before and after NP disappearance confirmed that the amount of Cu on silica has not changed throughout the process. All of this evidence implied that somehow the copper nanoparticles disappeared on the support at room temperature in ambient conditions, possibly by the migration of Cu atoms constituting each particle into the underlying support. This observation of spontaneous loss of copper nanoparticles on silica is quite surprising as it is very much against conventional wisdom, considering the many previous efforts to construct supported nanoparticle systems for heterogeneous catalysis.

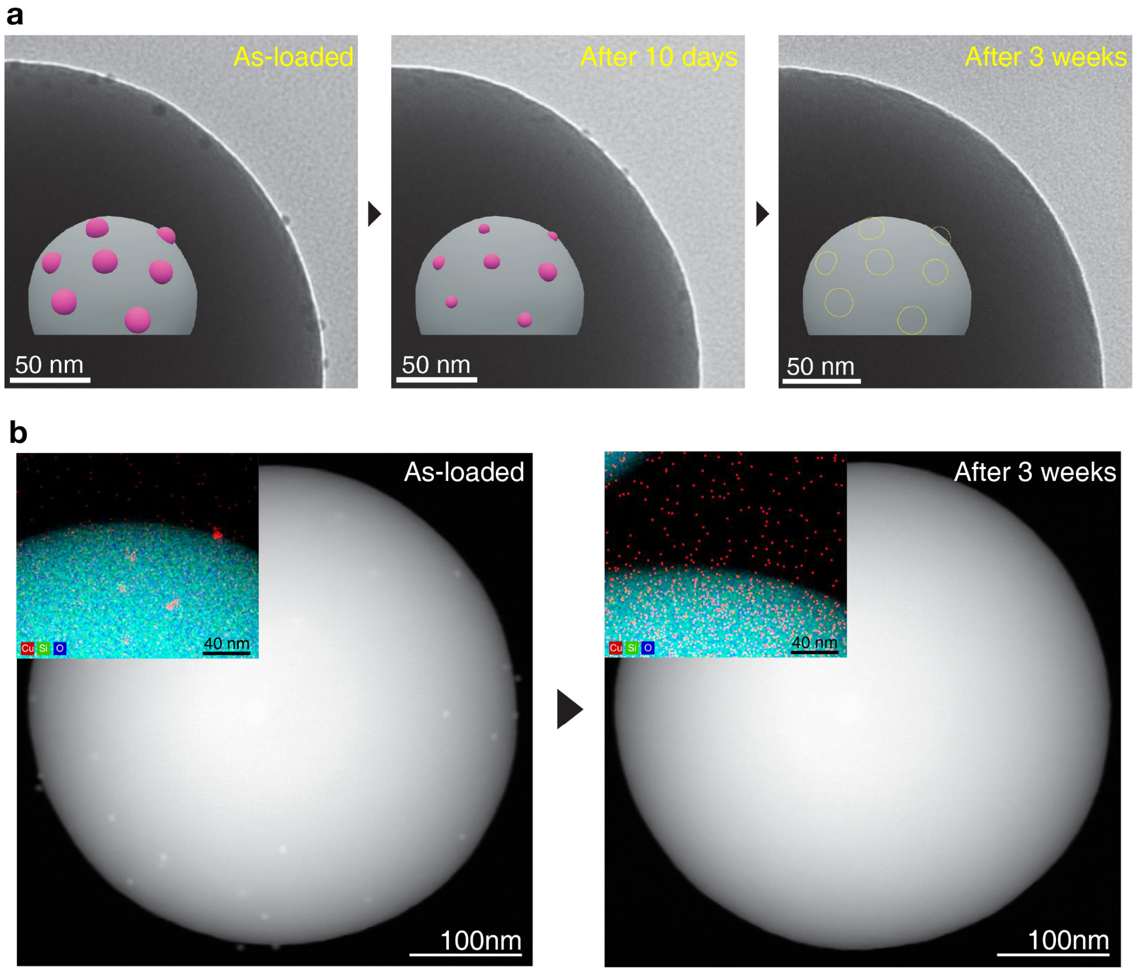

Figure 4.1. Vanishing of copper nanoparticles on silica. (a) TEM images of copper nanoparticles (with sizes from 6 to 7 nm) shrinking and disappearing within 3 weeks at room temperature and ambient atmosphere, when supported on amorphous silica. (b) STEM images of Cu nanoparticles on silica spheres and 3 weeks after loading, where initially loaded particles disappeared. Insets are elemental maps showing Cu (red), Si (green) and O (blue).

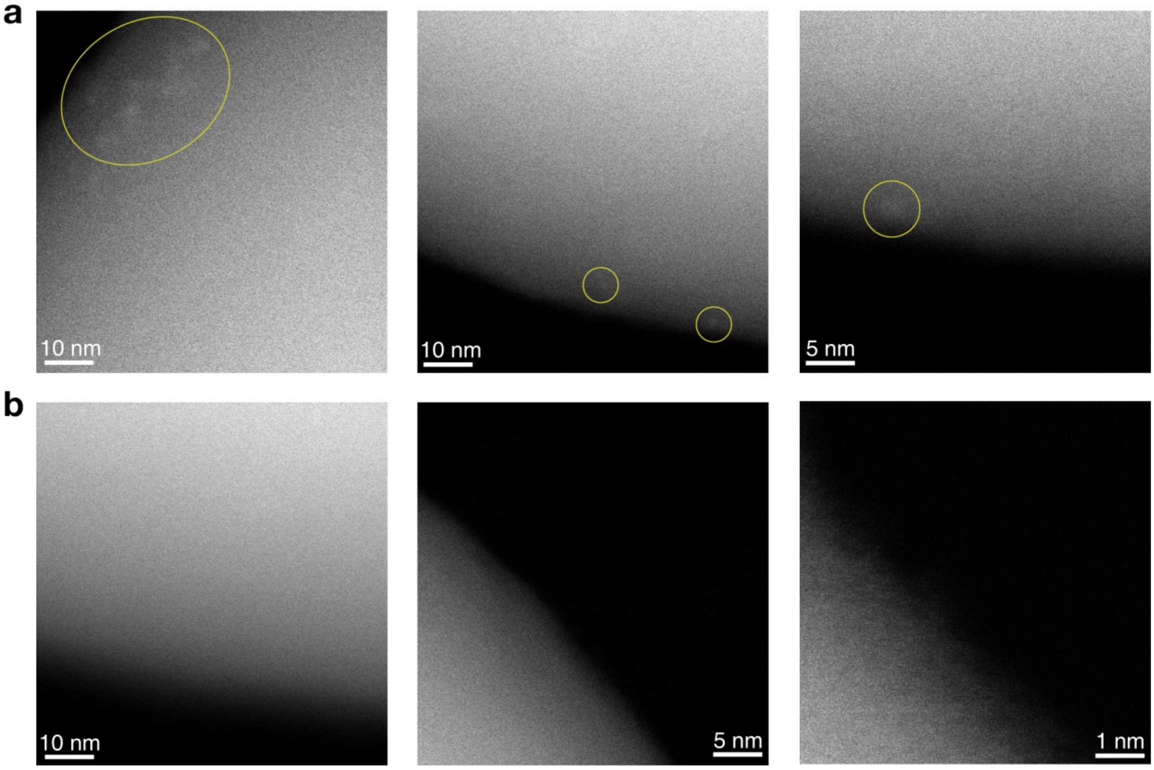

Figure 4.2. Aberration-corrected HAADF-STEM conducted for Cu NPs on silica spheres where NPs have partially (a) and fully (b) disappeared. While (b) shows uniform intensity (with a gradient from the center to the outer edge due to its thickness) originating from the silica support, bright spots can be observed in (a) which are the remaining NPs that have shrunk in size. Cu atoms that have been incorporated into the silica matrix (b) could not be imaged because of the low Z contrast of Cu relative to silica and the amorphous silica background.

In order to quantitatively understand this unexpected phenomenon, Cu nanoparticles were loaded onto amorphous silicon monoxide support grids in a well dispersed manner, allowing for quantitative tracking of the size of individual particles using TEM. The as-synthesized nanoparticles were loaded on the support grid (Figure 4.3a) and the grid was heated at 300 °C in air to remove the surface ligands and allow direct contact with the underlying silica support. As expected, the naked copper nanoparticles are typically oxidized partially or completely into Cu_2O upon surface ligand removal. The projected area (in nm^2) of the nanoparticles, assuming a spherical shape, was measured and tracked (Figure 4.3b) to estimate their size change. Interestingly, we found that the nanoparticles shrank rapidly within a 2 week time period under ambient conditions as shown in Figure 4.3a. For the case of 8 nm particles, a size decrease of ～1.5 nm was observed (Figure 4.3b). In contrast, the particles that were not heat treated (*i.e.*, with surface ligands attached and not in contact with the underlying support) maintained their shapes and actually slightly increased in their size, due to spontaneous oxidation of the metallic copper phase.

We hypothesized that this phenomenon of vanishing Cu nanoparticles could be related to the size-dependent energetics of nanoparticles. Cu nanoparticles with average sizes ranging from 6 to 17 nm (Figure 4.3) were tracked in the same manner with the ligands removed, allowing direct contact with an oxide support that led to all the particles being partially or completely oxidized. However, the behavior was quite different for the largest particle in that a size decrease was not observed during the same time period. Plotting the change in radius against time for all the particles (Figure 4.3c and 4.4) demonstrated a clear trend where the smaller particles declined in size more rapidly. The estimated radial decrease rates are ～0.12, ～0.06, and ～0.04 nm per day for 6, 8, and 11 nm-sized particles, respectively. In other words, the smaller particles exhibited a faster rate of diffusion of the copper atoms into the underlying silica support. For the 6 nm particles, the majority of them disappeared after 2 weeks (Figure 4.3a). This particle disappearance was measured by tracking the decreasing particle density (number of particles per micron square) over time (Figure 4.5). The quantitative analysis of how particles of various size regimes evolve revealed not only the possible trigger of this phenomenon, which is the increased energetic state at the nanoscale but also the effect of size-dependent energetics of nanoscale matter on the rate of the dynamic response of the constituent atoms to the support. Size-dependent energetics of nanoparticles and their constituent atoms are key elements explaining various properties of supported nanoparticles for catalytic applications.[152,154,155] For example, recently, nanoparticle size-dependent chemical potential of Cu atoms on CeO_2 has been reported[156] and control of nanoparticle sintering at high temperature has been demonstrated.[157,158] Importantly, the current observation reveals interesting aspects of nanoparticle thermodynamics even at ambient conditions.

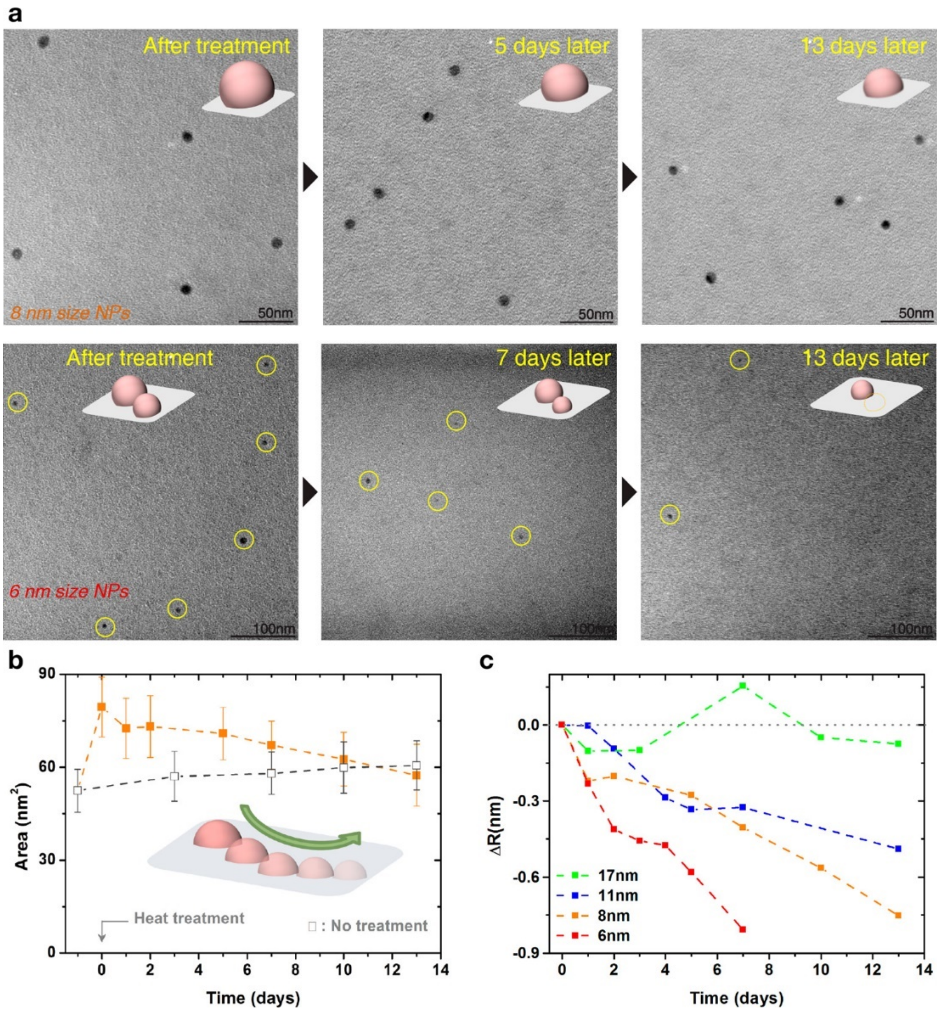

Figure 4.3. Quantitative analysis of vanishing copper nanoparticles. (a) TEM images showing copper nanoparticles shrinking and disappearing within the 2 week time period on an amorphous silicon monoxide support grid. Smaller particles are highlighted with yellow circles for clarity. (b) Average size, as presented by the projected area (nm^2), of the copper nanoparticles (8 nm) tracked within the 2 week time period after surface ligand removal (closed squares). In comparison, nanoparticles that have not been heat treated (*i.e.*, with the surface ligands remaining) are shown with open squares. Error bars represent one standard deviation. (c) Change in the radius (nm) of copper nanoparticles (average size ranging from 6 to 17 nm) over time on the support grid.

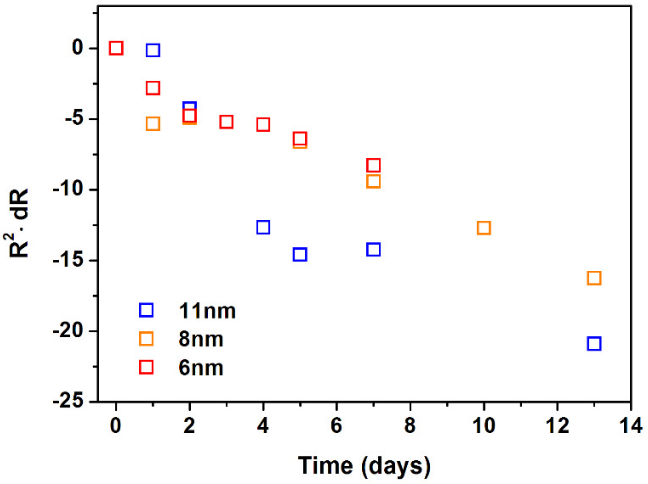

Figure 4.4. R^2dR versus time plotted for Cu nanoparticles of different size. The slope, which is the rate of change in nanoparticle volume indicative of the rate of loss of Cu atoms, between nanoparticles of different size is quite similar. This is plausible as migration of Cu atoms should happen across the surface of the particle (proportional to its dimension, R^2), so that though larger particles had a slower movement of Cu atoms, the associated area was larger.

$$\frac{dV}{dt} \propto R^2 \cdot \frac{dR}{dt}, \qquad \frac{dV}{dt} \propto \frac{dN}{dt} \propto R^2 \cdot J, \qquad \therefore \frac{dR}{dt} \propto J$$
$$V : volume, \quad R : radius, \quad N : number\ of\ atoms, \quad J : flux\ of\ atoms$$

Therefore, the rate of change in radius can serve as a representation for the rate of the phenomenon observed in this work. In other words, the particles that were smaller in size had a faster diffusive motion of their components, likely due to their increasing energetics. Here, it is assumed that each particle is isolated from the effect of other particles being present and this process is not limited by the silica support`s capability to accommodate Cu atoms (both possible by keeping a very low coverage of nanoparticles on the silica grid membrane).

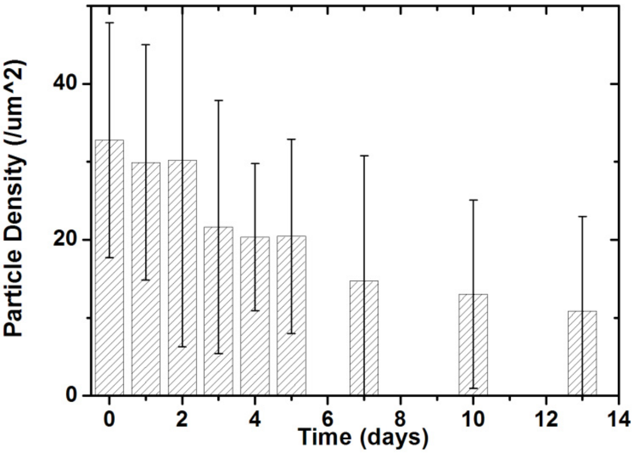

Figure 4.5. Quantitative analysis of particle density on the support grid for 6nm Cu nanoparticles.

4.1.2. Mechanistic understanding of disappearing copper nanoparticles

Having observed that the copper nanoparticles can disappear on silica support under ambient conditions, it is important to find out the nature of the copper sites within the silica. X-ray absorption spectroscopy (XAS) was used to specifically probe the copper *K*-edge of the Cu nanoparticles loaded onto silica spheres, where atomic level information could be obtained in order to elucidate the underlying process of the phenomenon observed. Figure 4.6a presents extended X-ray absorption fine structure (EXAFS) data from the Cu nanoparticle itself and after being loaded onto silica spheres. Cu nanoparticles exhibit their strongest feature at 2.2 Å corresponding to nearest Cu neighbors of Cu FCC metal at a bond distance around 2.52 Å. The second strongest peak, below 2 Å, is from the nearest oxygen scattering atoms, indicating that these nanoparticles contain native oxide layers due to the tendency of copper to oxidize. The fit was generated from multiple shells of pure Cu and Cu_2O models and the X-ray absorption near- edge structure (XANES) spectra also revealed that the as-made particles contained both phases. Cu nanoparticles were further oxidized while loading onto silica spheres as evidenced by the loss of the Cu−Cu interactions and the increase in the first oxygen shell scattering (Figure 4.6a). Furthermore, the loaded particles had a slightly higher oxidation state compared to Cu_2O nanoparticles, which may have resulted from direct contact to the relatively oxygen-rich silica support.[146] All of this indicated that an oxidized copper nanoparticle/silica interface was formed, which is a typical scenario during the preparation of oxide supported copper nanoparticles.

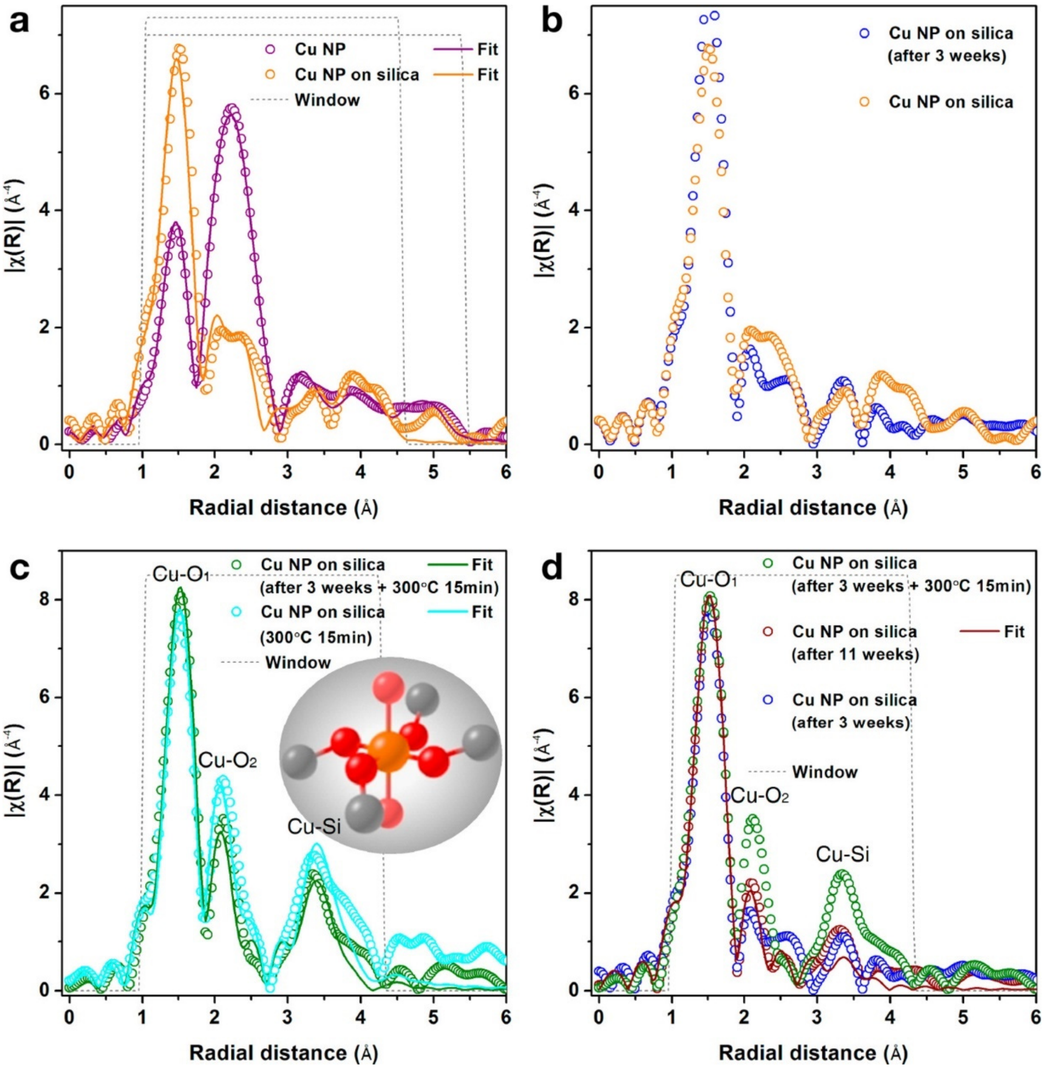

Figure 4.6. XAS study of vanishing copper nanoparticles on silica support. EXAFS spectra at the Cu *K*-edge comparing Cu nanoparticles as loaded on silica spheres to as-synthesized nanoparticles (a) and 3 weeks after loading (b) in which Cu nanoparticles have completely disappeared. (c) The 3 weeks after and the as-loaded samples were thermally treated under identical conditions and their EXAFS spectra were compared to show the local coordination environment of elemental copper within the matrix. Inset shown is a representation of the coordination environment surrounding Cu identified from the fit with Cu (orange), O1 (dark red), O2 (light red), and Si (gray). (d) EXAFS of Cu nanoparticles which were given 11 weeks on silica spheres at room temperature.

After particle disappearance (after 3 weeks), the EXAFS spectra only displayed a prominent feature for the first oxygen shell (Figure 4.6b), which increased in amplitude. Any characteristic features of outer shells were very weak and we attribute this to the amorphous nature of the matrix surrounding elemental copper. Cu atoms that migrated away from the original nanoparticle are mainly surrounded by a first shell of oxygen. We hypothesized that there might be an energetically favorable coordination environment for copper within the silica matrix, and the observed disordered structure around copper (Figure 4.6b) may very well be a kinetically limited transient state before reaching its final configuration. In order to probe whether the coordination environment for Cu atoms would continue to evolve beyond the state we observed after 3 weeks, the 3 weeks old samples were heat treated (300 °C for 15 min) to accelerate such a transition. The EXAFS spectra (Figure 4.6c) clearly presented a local structure that extended to at least three shells around copper, where the first two shells (with radial distances of 1.5 and 2.1 Å, respectively) were identified as oxygen at different bond distances and the third shell at 3.4 Å as silicon (Table 4.1 and inset of Figure 4.6c). Attributing the first three shells around the Cu absorber to other possible combinations of the elements besides the model used here did not provide a successful fit. Furthermore, when the Cu nanoparticles were heat treated under the same conditions but directly after loading onto silica spheres, we found the coordination environment around elemental copper to exhibit the same features (Figure 4.6c). This indicated that when given enough energy input, copper atoms were being structured to their energetically favorable state within silica. This also meant that copper atoms should eventually reach this final state, though it may be far slower under ambient conditions. Indeed, EXAFS spectra taken after 11 weeks also exhibited the three peaks at the position of the two oxygen shells and the third silicon shell (Figure 4.6d). When fitted to the model structure, however, the coordination number of the second oxygen shell was only around one (Table 4.1) most likely due to the fact that copper atoms have not fully transitioned to the final state. This was evident when fitting the third shell, where the Debye−Waller factor was relatively large (σ^2 ~ 0.04) due to the still amorphous nature of the surrounding elements.[159]

	Cu NP on silica 3 weeks + 300°C 15 min			**Cu NP on silica 300°C 15 min**			**Cu NP on silica 11 weeks**		
	N	*R* (Å)	σ^2	*N*	*R* (Å)	σ^2	*N*	*R* (Å)	σ^2
Cu-O1	3.6(0.4)	1.94(1)	0.004(2)	3.3(0.4)	1.94(1)	0.004(2)	3.9(0.3)	1.95(1)	0.005(1)
Cu-O2	2.8(0.8)	2.56(2)	0.005(5)	2.6(0.8)	2.54(2)	0.001(3)	1.2(0.6)	2.57(2)	0.005(7)
Cu-Si1	5.9(2.1)	3.91(3)	0.008(5)	4.6(1.7)	3.88(2)	0.004(4)	15.9(9.9)	4.00(4)	0.043(19)
ΔE	0.2(1.2)			-0.3(1.4)			1.2(0.8)		
R-factor	2.4%			3.3%			1.2%		

Table 4.1. EXAFS fitting parameters for the fits displayed in Figure 4.6.

Among the various potential causes of the phenomenon observed, it is possible that the Cu atoms are stabilized by impurities present in silica, considering the low loading conditions of Cu NPs (0.74 mg_{Cu}/g_{Silica}) and the limitation of EXAFS in distinguishing elements of similar atomic number. Therefore, while there is a possibility that the nearest neighbors surrounding Cu may not be purely oxygen, we emphasize that our prediction of the model structure is reasonable, based on previous studies that have identified oxygen-based octahedron motifs for metal ions (including Cu) in silica glass and silicate minerals.[160–163] Another possibility is that the energetically favorable configuration of Cu identified in this work may be induced by naturally present defects in silica, as these sites have been considered to be responsible for metal atom diffusion within the matrix.[164] Furthermore, entropic and enthalpic contributions to the change in total free energy have been considered together. From this view, it is important to note that the increased energetics associated with decreasing size of the nanoparticles could facilitate Cu atoms to energetically favor the identified local configuration of Cu within the silica matrix.

We have also conducted initial simulations of the Cu-silica system for the phenomenon observed using molecular dynamics. More specifically, amorphous SiO_2 was obtained using the melt-quench technique and ReaxFF potentials and the final structure was then further relaxed with density functional theory calculations. However, due to its inherently complex and ill-defined nature, amorphous silica structures with identical Si−O composition can have varying energy levels, subject to both the long-range and short-range disorders. The large degree of freedom in this system (including the previously mentioned factors possibly contributing to the energetic stability of Cu in the local coordination environment identified in this work) makes thermodynamic assessment of Cu diffusion from a nanoparticle into silica challenging and error-prone, and assessing the kinetics of this process is certainly not feasible at this time. However, from the EXAFS study, we could show that the supported copper nanoparticles vanished into the silica support by the dynamic movement of copper atoms, eventually stabilizing in a coordination environment surrounded by shells of oxygen and silicon atoms. Together with the quantitative study of the phenomenon, we can conclude that the driving force for copper atom diffusion into silica is the favorable local configuration within the matrix identified through EXAFS in comparison to the relatively high energy state in small nanoparticle form. Also, this leads to the possibility that supported Cu nanoparticles may actually be in a state of nanoparticles together with single atom species within the supporting matrix.

4.1.3. Conclusions

Supported metal nanoparticles have been used for various applications where the supporting substrate is typically used to stably hold the nanoparticles and to create a nanoscale junction. The fact that copper nanoparticles can interact with the underlying amorphous silica support by the movement of copper atoms even under ambient conditions opens up many fundamental questions regarding the nature of supported metal nanoparticles and the resulting chemical and physical properties.[165] For example, the observed catalytic activities of supported copper nanocatalysts may not be from the particles alone, but in addition or even alternatively the copper sites located within the matrix could in principle contribute synergistically.[166,167]

4.2. Structural transformation of copper nanoparticles for selective electroreduction of CO_2 to C_2–C_3 products

Electrochemical conversion of CO_2 to carbon-based products, which can be used directly as fuels or indirectly as fuel pre-cursors, is suggested as one of the promising solutions for sustainability. Not only does this process allow using renewables such as solar electricity as energy input, but CO_2 emitted from the consumption process can be recycled back into fuels. The success of this technology depends on the value added to the product that forms from CO_2. However, major progress has been limited to two-electron reduced products of CO and formate. Still, the formation of multicarbon products involving multiple proton and electron transfers remains as one of the biggest scientific challenges to be addressed.

Here, we show that an ensemble of densely packed copper nanoparticles could enable selective conversion of CO_2 to multicarbon products, while significantly suppressing C_1 formation. Catalytically active cube-like structures, capable of forming ethylene, ethanol, and *n*-propanol, are formed during electrolysis by the structural transformation of the Cu NP ensemble. These structures can selectively generate C_2 and C_3 products together at low overpotentials in neutral pH aqueous media and exhibit good stability for extended periods of operation. The discovery of this catalyst illustrates the importance of *in situ* structural dynamics of materials in CO_2 electrocatalysis.

4.2.1. Structural transformation of copper nanoparticles in CO_2 electrochemical conditions

Monodisperse Cu NPs (size 6.7 nm) prepared were directly deposited onto carbon paper support (1 cm^2_{geo}) to form densely packed NP ensembles. Cu NP loading was systematically increased starting from the lowest loading of ～2 μg of Cu (×1). Most of the NPs are isolated at the lowest loading condition, and increased loadings resulted in densely packed arrangements of Cu NPs (Fig. 4.7a). In the case of ×22.5 loading, the surface was mostly covered with closely packed Cu NPs.

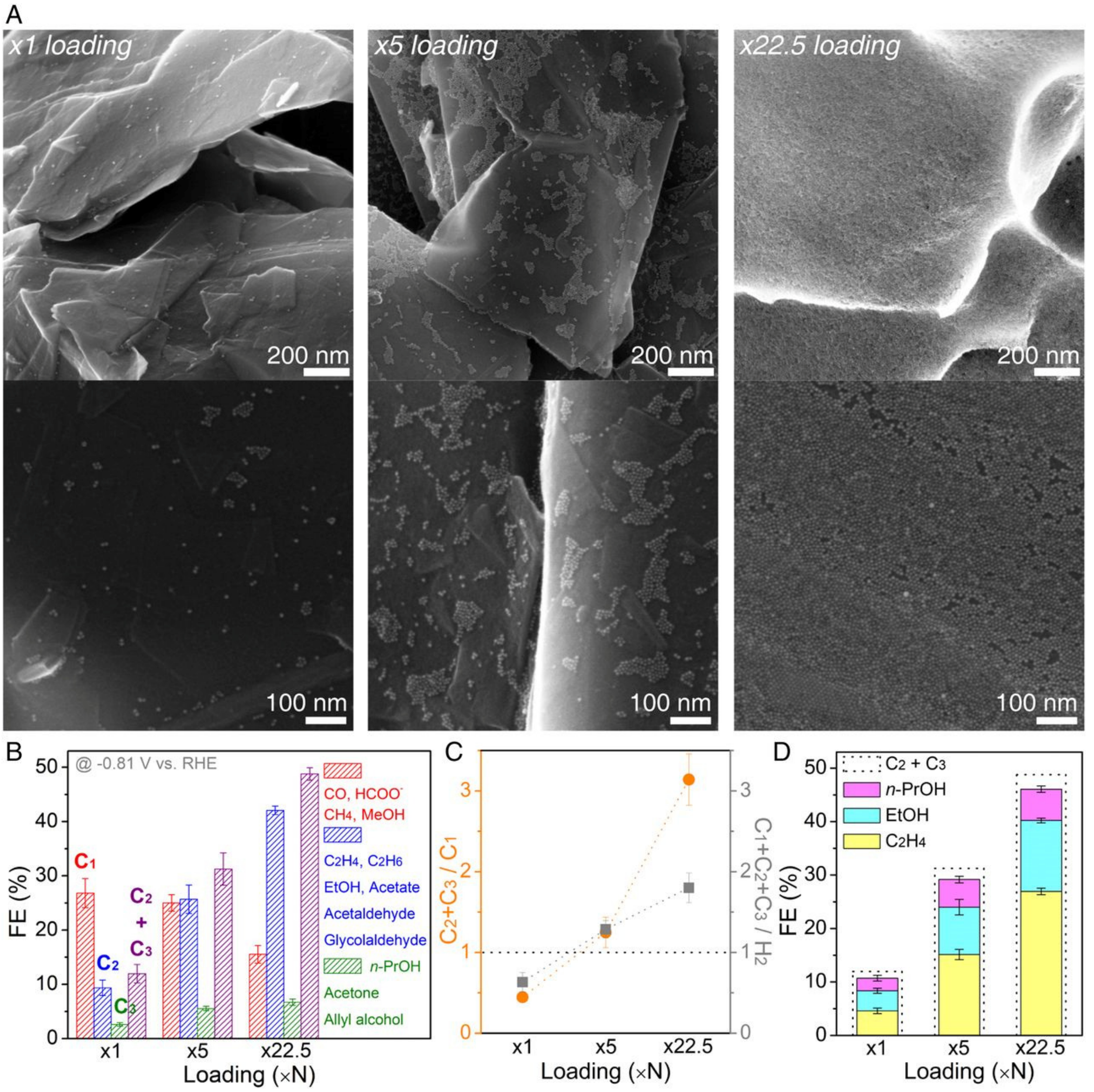

Figure 4.7. Varied density of Cu NP ensembles and their electrocatalytic activity. (a) SEM images of Cu NPs loaded on carbon-paper support at ×1 loading, ×5 loading, and ×22.5 loading. (b) FEs (%) for C_1, C_2, and C_3 products. (c) Relative ratio of the FEs. (d) Ethylene, ethanol, and *n*-propanol FE with the dotted line showing the overall C_2–C_3 FE. Activity measured at −0.81 V vs. RHE, using 0.1 M $KHCO_3$ saturated under 1 atm CO_2. Error bars shown in b–d are 1 SD from three independent measurements.

Cu NP ensembles with varied loading densities were tested for their electrocatalytic CO_2 reduction activity, under identical conditions of 0.1 M $KHCO_3$ at 1 atm CO_2. From product analysis, we found that increased loadings resulted in a drastic rise of the C_2–C_3 faradaic efficiency (FE) (Fig. 4.7b). This trend is consistent with the observed loss of C_1 products, indicating that carbon-based intermediates could be effectively coupled to yield multicarbon products. When plotting the relative ratio of the C_2–C_3 FE to C_1 FE (Fig. 4.7c), charge consumed to reduce CO_2 was mainly from the reaction pathways to C_2–C_3 products at increased loading conditions, reaching up to 76% out of the total CO_2 reduction products. Similar trends can be seen with CO_2 reduction dominating over the competing H_2 evolution (Fig. 4.7c). Among various C_2–C_3 products, ethylene (C_2H_4), ethanol (EtOH), and *n*-propanol (*n*-PrOH) were the majority, constituting 94% out of the total C_2–C_3 products generated (Fig. 4.7d).

When probing the product distribution over time for the ×22.5 loading condition, an abrupt change occurred during the initial period (Fig. 4.8b). Hydrogen was the dominant product when gas products were measured 3 min after the start of electrolysis. Selectivity for C_2H_4 increased afterward. A similar trend was found for the liquid products as well, where liquids analyzed for the first 7 min had less multicarbon products relative to formate. Visual inspection of the electrode also supported the fact that product distribution was shifting during its initial electrochemical testing, as more gas bubbles were observed at the beginning of electrolysis, probably due to the majority of charge being consumed for two-electron transfer products, such as hydrogen.

This observation indicated that the NP ensemble may go through a structural transformation process during initial electrolysis. Instead of the starting densely packed Cu NPs (×22.5 loading, Fig. 4.7a), cube-like particles (10 - 40 nm) mixed together with smaller NPs were observed on the carbon support after electrolysis (Fig. 4.9). Carbon-paper supports with lower loading were also checked after electrolysis and a trend could be observed: the more densely packed the Cu NPs, the more likely the formation of cube-like particles (Fig. 4.9). When Cu NPs were sparsely covering the support, random aggregates of NPs together with the pristine NPs could be found after electrolysis. Surface-area analysis of Cu NP ensembles after electrolysis also showed that the densely packed NPs transformed to larger particles. Structural transformation of the NP ensemble (Fig. 4.8a) occurred during the initial stage of electrolysis. This was confirmed from observation of the electrode 7min after the start of electrolysis (Fig. 4.8c), which coincided with the shift in catalytic activity (Fig. 4.8b). Negligible catalytic activity of the underlying carbon paper further supports that the structure derived from Cu NP ensembles is responsible for enhanced C_2–C_3 formation. This catalytically active structure formed starting from densely packed Cu NP ensembles (×22.5 loading on carbon-paper support in 0.1 M $KHCO_3$), hereafter referred to as trans-CuEn, was further investigated.

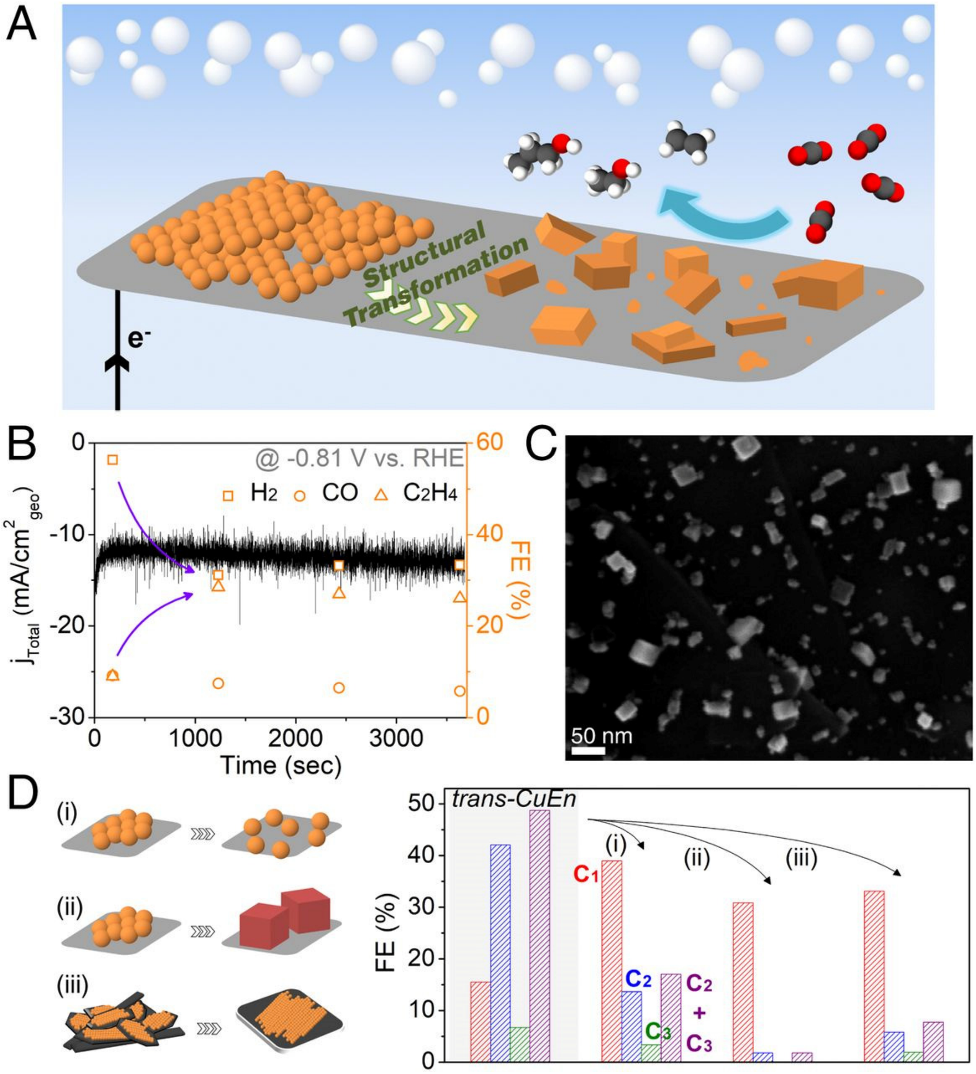

Figure 4.8. Structural transformation of Cu NP ensembles. (a) Schematic illustrating the transformation process of Cu NP ensembles to an active catalyst for C_2–C_3 product formation. (b) Total current density (based on geometric area) versus time plot for ×22.5 loading condition at −0.81 V vs. RHE. FE of gas products are shown at the time point of measurement. FE of CH_4 and C_2H_6 are omitted because of their low values. (c) SEM image of ×22.5 loaded carbon-paper support electrode after 7 min of electrolysis at −0.81 V vs. RHE. (d) Investigation of the parameters affecting structural transformation of Cu NP ensembles and their catalytic activity. Three different conditions have been tested: (i) separation of the NPs from their initial densely packed assembly, (ii) use of Cu nanocubes as starting materials, and (iii) change of support to a low surface area carbon plate. FE of C_1, C_2, and C_3 products obtained from trans-CuEn (left column, shaded, at −0.81 V vs. RHE) are compared with the activity measured for three different conditions [at (i) −0.84 V, (ii) −0.86 V, and (iii) −0.81 V vs. RHE, respectively]. Electrochemical tests were conducted using 0.1 M $KHCO_3$ solution at 1 atm CO_2.

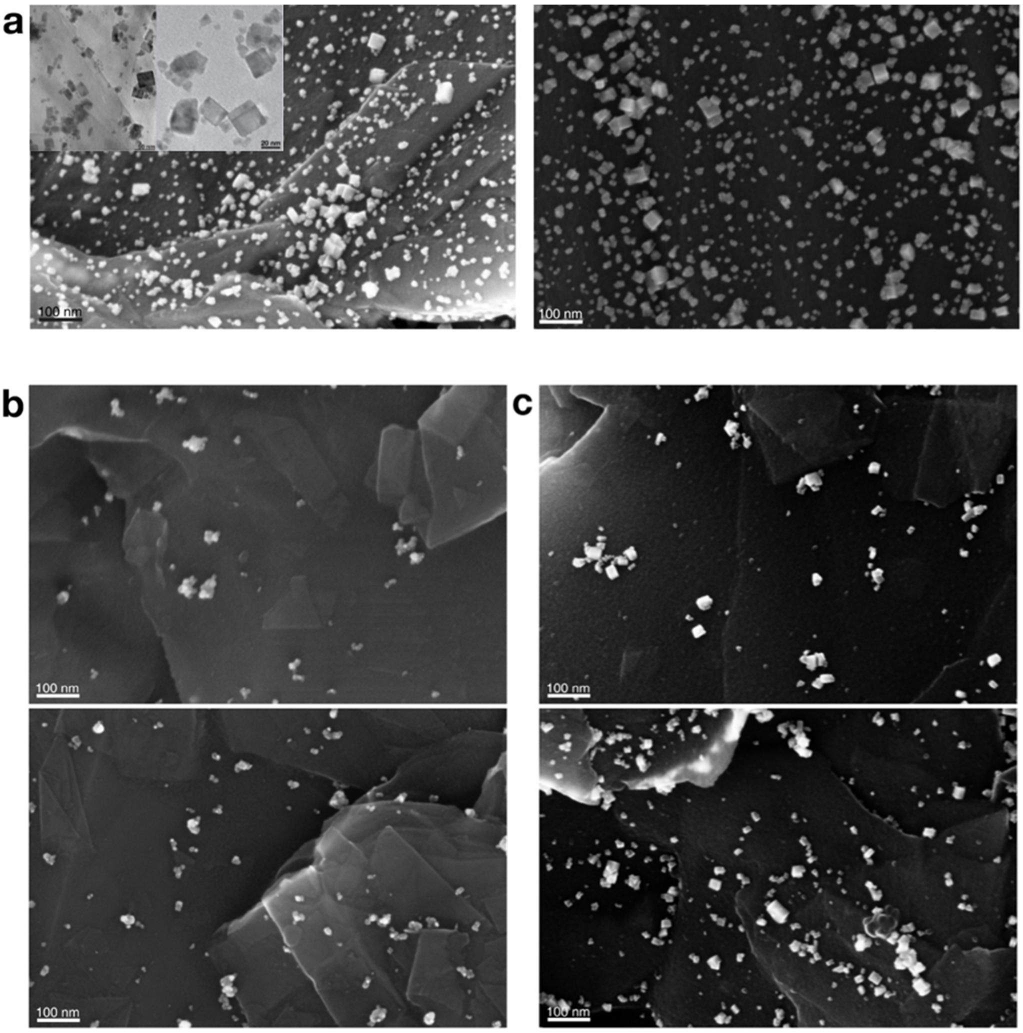

Figure 4.9. Morphological changes of copper nanoparticle after electrolysis. (a) SEM images of the Cu NP ensemble (×22.5 loading) on carbon paper support after 1hr electrolysis. TEM images shown as insets. SEM images of ×1 loaded (b) and ×5 loaded (c) carbon paper support after 1hr electrolysis.

As the initial loading density of Cu NP ensembles (and their densely "packed-ness") tends to govern their structural transformation during electrolysis and resulting electrochemical activity, we tried to intentionally separate the Cu NPs in the precursor state to trans-CuEn. We expected the transformation process to cube-like structures to be disrupted, leading to diminished C_2–C_3 selectivity. Cu NPs (×22.5 loading) were mixed with carbon black before depositing on carbon-paper support, which led to NPs being spatially separated from each other. Under this condition, substantial loss of C_2–C_3 product selectivity (FE from 49 to 17%) was observed (Fig. 4.8d), while CO and $HCOO^-$ became major products. When particles were examined after electrolysis, the structure more resembled what would be observed for low-density conditions. Cu NPs have been observed to electrically fuse into irregularly shaped large crystals under strong bias conditions (<−1.25 V vs. RHE), reaching a similar state irrespective of the initial conditions.[168] Here, we find that structural transformation can be caused not only under low bias conditions, but controlled by the initial arrangement of NPs, and consequently catalytic behavior for multicarbon products can be significantly improved.

As trans-CuEn displays cubic-shaped particles, copper nanocubes loaded onto carbon paper support were tested under identical conditions for comparison. We used Cu nanocubes that have been previously studied for CO_2 reduction.[169] Specifically, cubes with edge length 25 nm were used (with copper loading mass identical to trans-CuEn) to approximately match the cubic-shaped particles that vary in size (10 ～ 40 nm) for trans-CuEn. In contrast to trans-CuEn, observed structural changes were minimal where the cubes seem to have sintered or roughened. Furthermore, only small amounts of multicarbon products were detected (Fig. 4.8d). The result is consistent with the earlier report of Cu nanocubes, which claims multicarbon product formation at high overpotentials (<−1 V vs. RHE).[169] Therefore, we find that simple reproduction of the key morphological feature present in trans-CuEn is insufficient to reach high multicarbon selectivity.

This leads to the possibility of cube-like particles derived *in situ* during electrolysis featuring unique active sites for C_2–C_3 formation. Recently, scanning tunneling microscopy investigation of copper for carbon monoxide reduction has shown not only the reconstruction of a polycrystalline surface to a (100) surface, but also the additional structural transformation unique to the (100) reconstructed copper, leading to stepped surfaces which selectively generate ethanol.[170,171] While this observation may have been for reducing CO, together with the findings here, it brings into attention the importance of *in situ* structural transformation for multicarbon product formation in copper-based catalysts. In addition, we would like to point out that while the vast majority of research has been to use oxide-derived structures, with even some reports claiming the importance of remaining oxidized copper,[172,173] the catalytically active structure derived here is from pristine Cu NPs (with a thin layer of surface oxide naturally present). Furthermore, we find that the structural transformation observed is unique to the original Cu NPs. Therefore, it would be important to understand how this structural transformation proceeds and what type of active site motifs are present under working conditions. This is especially the case for copper, which may oxidize after electrolysis, possibly leading to the loss of surface atomic information. However, we also cannot rule out the possibility that high multicarbon selectivity stems from having a mixture of particles,[174] which are the cube-like ones together with smaller particles. With all of these taken into consideration, further investigation into the structural origin of high multicarbon selectivity from Cu NP ensembles is needed.

Furthermore, we investigated the role of the catalyst support by depositing Cu NPs onto a highly polished graphite plate (1 cm^2_{real}, roughness factor ~1), while keeping the NP density(/cm^2_{real}) identical to that of trans-CuEn. Structural transformation occurred in a similar way resulting in cubic-shaped particles. However, H_2 and C_1 products were the major products (Fig. 4.8d). We speculate that this difference is due to local pH effects discussed in earlier reports,[63,71] as the loss in the real surface area of the underlying support led to a sharp decrease of the geometric current density (lowered to ≈1/5 of the original). The increased local pH by large current density of trans-CuEn (on carbon-paper support) could play a role in determining its catalytic behavior. Therefore, it seems that it is important to not only start from a high density of closely packed Cu NPs to facilitate the structural transformation, but also have the underlying support provide sufficient surface area. This shows why high C_2–C_3 selectivity was not observed from the previous report of Cu NP monolayers.[103]

4.2.2. CO_2 electroreduction activity of structurally transformed Cu NPs

Catalytic activity of trans-CuEn was further probed at various potentials (Fig. 4.10) in 0.1 M $KHCO_3$. The onset of C_2–C_3 formation was observed at only −0.57 V vs. RHE, with products mainly comprising C_2H_4, EtOH, and *n*-PrOH. Compared with that of the pristine copper foil,[9] overpotentials were lowered by 180 mV for C_2H_4 and 390 mV for EtOH and *n*-PrOH, respectively. Beyond this potential, a substantial rise in C_2–C_3 FE was observed, with the highest selectivity toward C_2–C_3 products (55%) achieved at −0.86 V vs. RHE. The high selectivity for C_2–C_3 products, including oxygenates, is quite significant, compared with previously reported catalysts for C_2–C_3 product formation around similar overpotentials applied in neutral pH aqueous media. So far, catalysts for multicarbon products have been Cu-based (mostly derived from oxides or halides) and require bias applied close to and beyond −1 V vs. RHE, where even only some of them reach product distributions dominated by C_2–C_3 products (C_2–C_3 > C_1 + H_2). Furthermore, with major efforts in the field toward using oxidized Cu as a starting template, the discovery of this catalyst presents an approach to achieving high C_2–C_3 selectivity for electrochemical CO_2 reduction. In contrast, FE for two-electron reduced products (CO and formate) could be lowered to ~1%, implying that almost all of the CO_2 interacting with the catalyst could undergo C–C coupling to yield more complex products (Fig. 4.10b). In assessing catalytic performance for multicarbon product formation, earlier reports have been using C_2H_4/CH_4 FE ratio as a figure of merit and trans-CuEn exhibits significantly high values at low overpotentials (~252 at −0.78 V vs. RHE) that are comparable or better than previous catalysts reported for selective formation of C_2H_4. More negative bias applied leads to increase in CH_4 formation and C_1 FE.

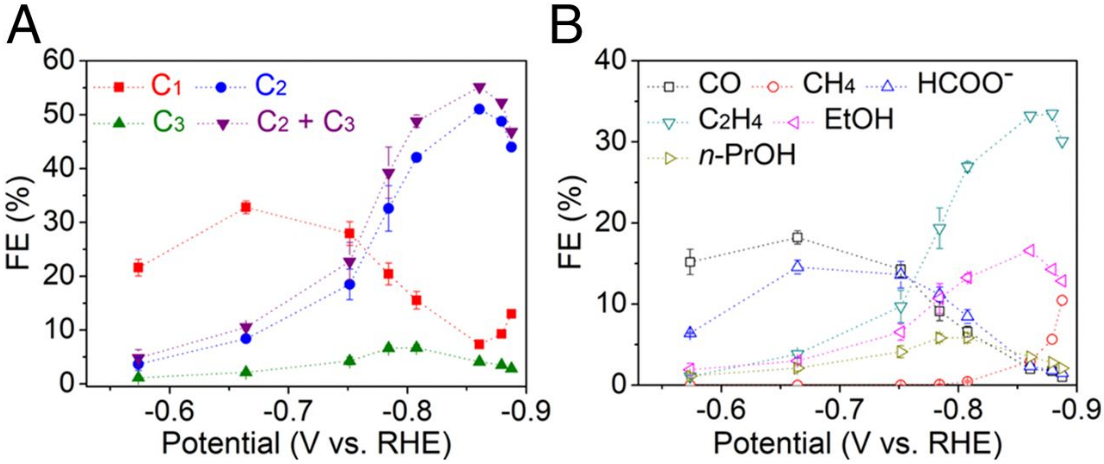

Figure 4.10. Electrochemical CO_2 reduction activity of trans-CuEn. (a) FE of C_1, C_2, and C_3 products at various potentials for trans-CuEn. (b) FE of major products at various potentials for trans-CuEn. Electrochemical tests were conducted using 0.1 M $KHCO_3$ solution at 1 atm CO_2. Error bars shown are 1 SD from three independent measurements.

It has been suggested that larger cations promote higher concentrations of CO_2 near the catalyst surface, leading to increased activity.[66] For further optimization, Cu NP ensembles were tested in 0.1 M $CsHCO_3$ aqueous electrolyte saturated with 1 atm CO_2 and a similar trend was observed where increased loading densities resulted in higher C_2–C_3 selectivity. Transformation of Cu NP ensembles (at optimized condition of ×32.5 loading in 0.1 M $CsHCO_3$) consistently resulted in cube-shaped particles mixed together with smaller NPs (Fig. 4.11), hereafter referred to as trans-CuEn 2. Activity of trans-CuEn 2 was measured at various potentials (Fig. 4.12) and high C_2–C_3 selectivity was observed at more positive potentials with the onset of C_2–C_3 formation at only −0.53 V vs. RHE, which is 40 mV less of applied overpotential compared with that observed in 0.1 M $KHCO_3$. Highest C_2–C_3 selectivity (～50%) was observed at −0.75 V vs. RHE, shifting the potential 110 mV more positive relative to the point of maximum C_2–C_3 FE in 0.1 M $KHCO_3$. Therefore, with this catalytic structure, selective electrocatalytic conversion CO_2 to C_2–C_3 hydrocarbons and oxygenates could be achieved at significantly reduced overpotentials, compared with what have been demonstrated up to now. Similarly, the main products were C_2H_4, EtOH, and *n*-PrOH (Fig. 4.12b) constituting up to 95% of total C_2–C_3 products. In addition, not only were FEs of CO and formate decreased to very low levels (1 ～ 2%), but CH_4 formation could also be suppressed (< 1%) across the entire potential region, resulting in a significantly high C_2H_4/CH_4 ratio (～2,133 at −0.73 V vs. RHE) at low overpotentials. Owing to its high C_2–C_3 selectivity in 0.1M $CsHCO_3$, the proportion of C_2–C_3 products among the total CO_2 reduced products reached up to 90% (Fig. 4.12c).

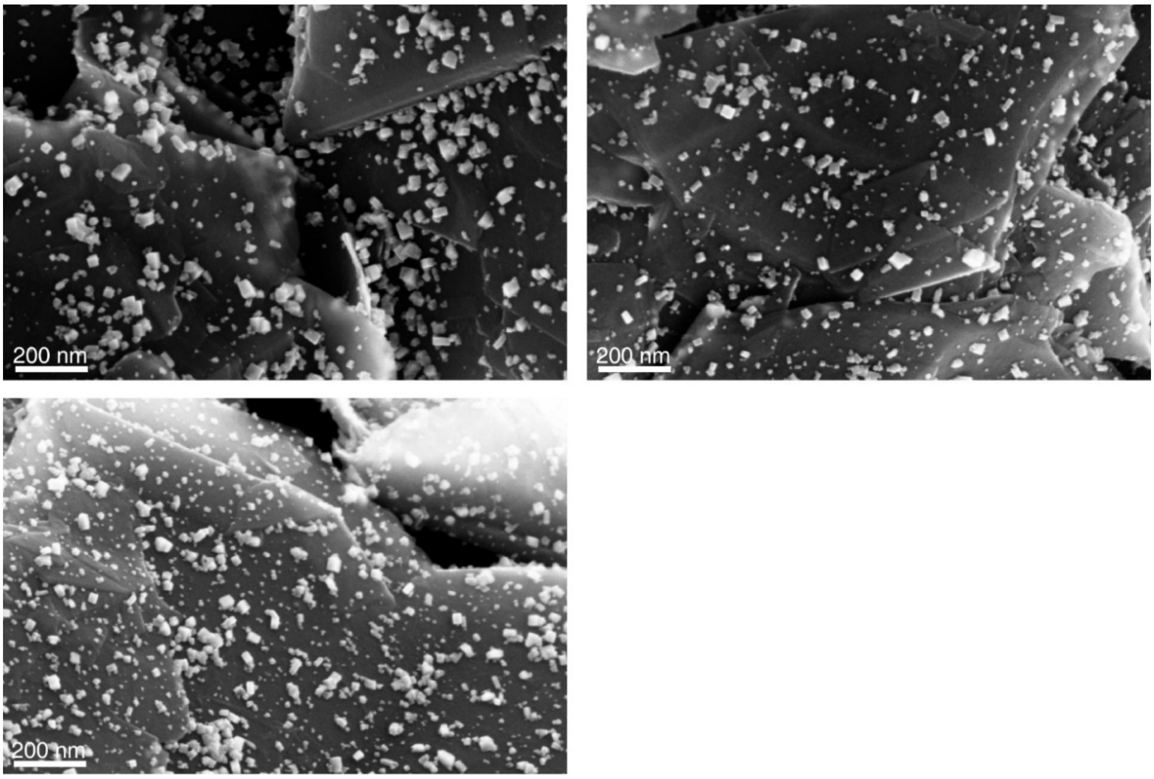

Figure 4.11. Structural transformation observed of Cu NP ensembles (×32.5 loading) after electrolysis in 0.1M $CsHCO_3$ at -0.75 V vs. RHE.

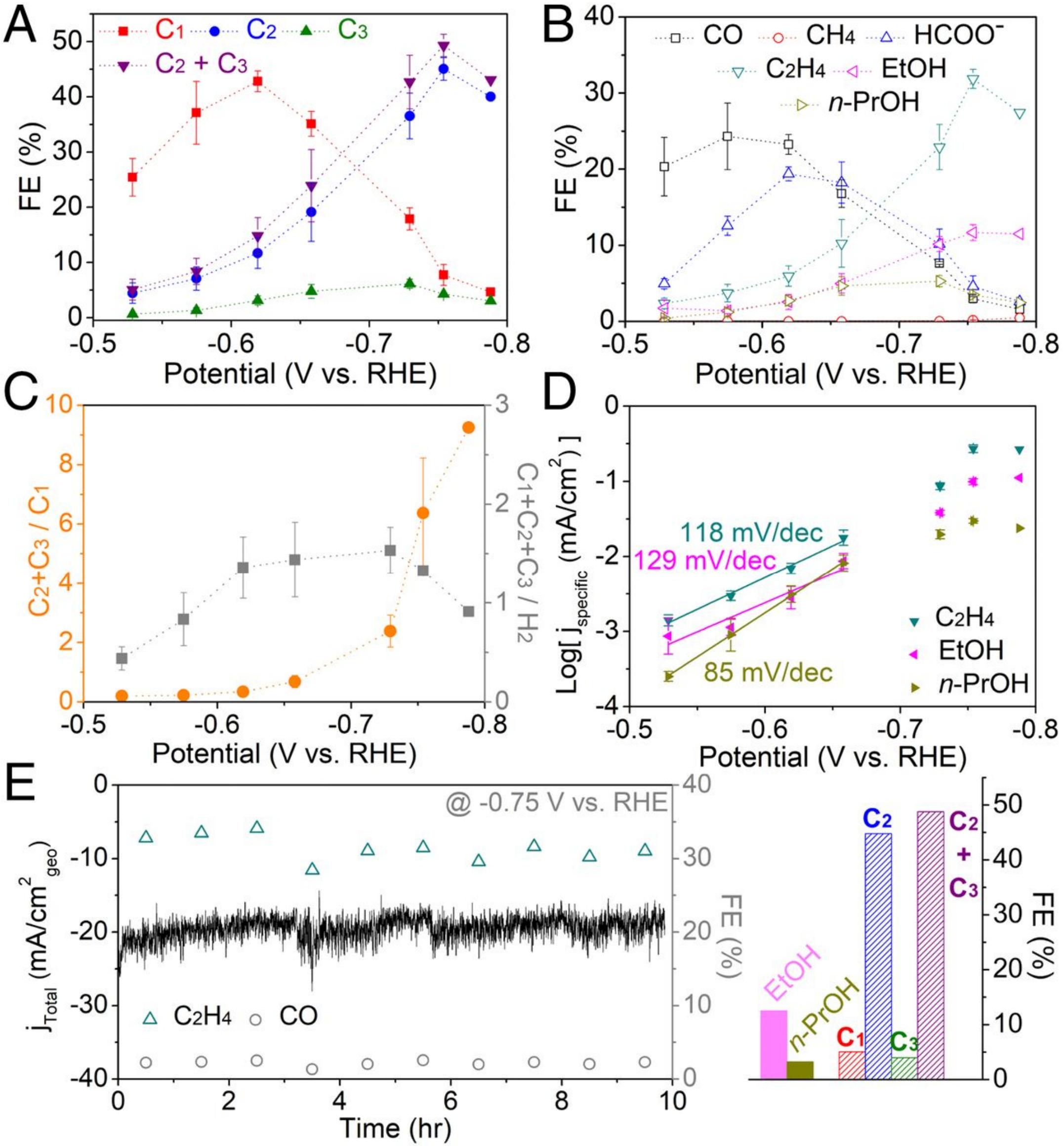

Figure 4.12. Electrocatalytic behavior of trans-CuEn 2 (×32.5 loading in 0.1 M $CsHCO_3$). (a) FE of C_1, C_2, and C_3 products at various potentials. (b) FE of major products at various potentials. (c) Relative ratio of the FE. (d) Logarithmic specific current density (corrected by the real surface area of the catalyst) plots for C_2H_4, EtOH, and *n*-PrOH. Electrochemical tests were conducted in 0.1 M $CsHCO_3$ solution at 1 atm CO_2. Error bars shown are 1 SD from three independent measurements. (e) Long-term electrolysis at −0.75 V vs. RHE with gas products measured every hour. Column graph on the right shows FE of EtOH and *n*-PrOH measured after electrolysis and C_1, C_2, and C_3 product FEs for the overall run.

With the real surface area of trans-CuEn 2 measured, specific current density plots and Tafel slopes of the three major products could be obtained (Fig. 4.12d). Both C_2H_4 and EtOH exhibit similar slopes (～120 mV/dec), indicative of a rate-determining step with a common intermediate. Furthermore, C_2H_4 and EtOH start forming in the potential region where CO evolution is dominant and increase while CO diminishes (Figs. 4.10b and 4.12b), suggesting that formation of these C_2 products is essentially limited by the coupling of major C_1 intermediates. It has been also shown that higher coverages of *CO can be expected in the region where CO formation is majorly observed.[175] Therefore, with a slope close to 120 mV/dec suggesting a single electron transfer step, we expect the rate-determining step to be a reductive coupling (*i.e.*, dimerization) step of adsorbed CO intermediates, predicted from theory and carbon monoxide reduction experiments on copper[13,52,56] :

$$*CO + *CO + e^- \rightarrow *C_2O_2{}^-$$

On the other hand, *n*-PrOH exhibits a different slope, suggesting a distinct rate-determining step from that of C_2 products. Estimated value is rather close to that observed for CH_4 on copper foil (86 mV/dec).[168] In addition, it has been reported that *n*-PrOH formation only occurs when reactants include both CO (carbon monoxide) and C_2H_4, while CO reduction solely leads to EtOH.[176] If C_3 products followed the same pathway as C_2 products, *n*-PrOH should have been observed upon CO reduction. Instead, it may be that *n*-PrOH formation requires coupling between CO and hydrogenated carbon [*e.g.*, carbene ($*CH_2$)], which is a major intermediate in the pathway to CH_4.[13] CH_4 formation activity of trans-CuEn and -CuEn 2 supports this idea as well (Figs. 4.10b and 4.12b). In contrast to C_2H_4 and EtOH, *n*-PrOH reaches peak selectivity at a more positive potential and the potential in which *n*-PrOH FE drops coincides well with the point where CH_4 FE starts to rise. However, it is still unclear how formation of C_3 products occur and an in-depth study of the mechanistic pathways to these products is needed.

Long-term stability was demonstrated by 10 h electrolysis of trans-CuEn 2 at −0.75 V vs. RHE (Fig. 4.12e). Average C_2–C_3 FE reached ～50% for the overall run and structural features of trans-CuEn 2 were maintained as well. Furthermore, stable C_2–C_3 product current density of 10 mA/cm^2_{geo} was achieved, which is potentially attractive for solar-to-fuel applications. As long-term electrolysis accumulates significant amounts of liquid products, propionaldehyde, likely to be the precursor to *n*-PrOH, was detected.

Stable and selective C_2–C_3 product generation achieved by the structurally transformed Cu NP ensembles presents a promising future direction to renewables-powered artificial carbon cycle. Projected solar-to-fuel efficiencies of multicarbon products (Fig. 4.13), assuming combination of commercial Si photovoltaic devices and electrolysis configurations recently demonstrated for effective syngas formation,[177,178] are comparable or better than natural photosynthesis (*e.g.*, 2.8% for C_2H_4). Significant mass activities can be achieved as well, desirable in terms of cost-effectiveness, due to extremely low mass (g_{Cu}) used compared with other methods that rely on bulk Cu oxidation.

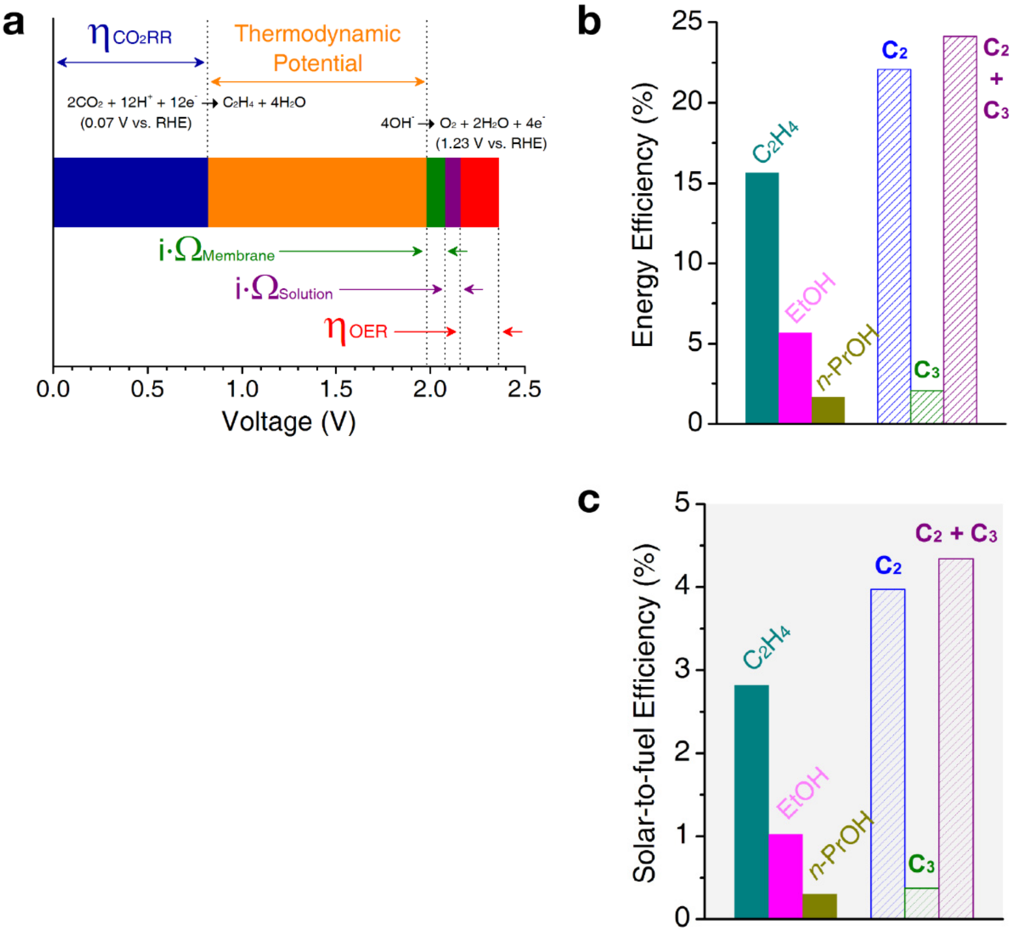

Figure 4.13. Performance estimates in electrolyzer configurations. (a) Voltage distributions (2.36 V applied) in an electrolyzer incorporating NiFe hydroxide anode and bipolar membrane. Overpotential at the anode (η_{OER}) and voltage losses from the solution and the membrane are from ref. [178], which describes a system operating at ~16 mA (close to the operating condition of the catalyst described in this work at -0.75 V vs. RHE). Overpotential at the cathode (η_{CO2RR}) shown is for ethylene and it will vary depending on the product. (b) Energy efficiency estimated for major C_2-C_3 products. (c) Solar-to-fuel efficiency estimated for major C_2-C_3 products, assuming 18% solar-to-electricity efficiency provided from commercial Si solar cells.

4.2.3. Conclusions

We have shown how an ensemble of Cu NPs can enable selective electrocatalytic conversion of CO_2 to C_2–C_3 hydrocarbons and oxygenates at significantly reduced overpotentials. Structural evolution of densely arranged Cu NPs resulted in C_2–C_3 active nanostructures and experimental investigation of the parameters affecting structural transformation and their catalytic behavior was performed. With the discovery of this active catalytic structure formed *in situ*, efforts in deepening the understanding of how NPs and atoms within evolve under electrically biased and chemically relevant conditions seem necessary, which will shed light on the key structural features for CO_2 conversion to multicarbon products. Furthermore, we anticipate that the unique approach of using NPs as precursors to an active nanostructured material will lead to a wide expansion of the materials library for various catalytic applications.

Chapter 5

Summary and Perspectives

Chemical valorization of carbon dioxide using electrochemical methods has great potentials in various sectors of our society by fundamentally changing the way we use energy and resources. Products electrochemically converted from CO_2 can be utilized directly as fuels and chemicals or used as chemical precursors to more advanced products, such as plastics and pharmaceuticals. Carbon-based products attained in this manner are desirable as the process is less energy intensive, compared to the traditional methods, and can be coupled to renewable electricity sources. More importantly, the technology targets the uses of atmospheric carbon dioxide which will allow closing up of the carbon cycle which has been disturbed by the latest human activities leading to the threats of uninhabitability.

The key to the success of this technology lies in the performance of the catalyst materials in efficiently converting the carbon dioxide to useful products. In this regard, nanoparticles have provided great advances in being able to be used as efficient electrocatalysts and to provide the fundamental understandings behind the processes involved. Furthermore, the synthetic advances that have preceded have given us the tools to study deeply into the catalytic effects of various structural factors of nanoparticles spanning over large length scales. A number of works discussed here illustrate the structural diversity of nanoparticles as CO_2 electrocatalysts and hints at their potential where there is much more room to be explored.

In addition, the latest discoveries of the structural dynamics involved with nanoparticles, especially during catalytic transformation reactions, offer new perspectives in catalyst development. In order to understand the catalytic origin of materials, critical to establishing design principles of catalysts, their dynamic nature should be taken into account. Furthermore, synthesis of nanoparticles as catalysts should be able to accommodate the possible structural changes in relevant chemical environments, so that the most optimized catalytic structure can be obtained during real-time operation. With all of these factors considered, we would be able to achieve unprecedented improvements in CO_2 electroconversion using nanoparticle catalysts.

Of course, for the technology to be introduced into society and succeed in replacing the conventional ways of harnessing energy and chemicals, scientific and technological developments in the closely related areas are needed. These areas include CO_2 capture, product separations, and renewable energy. Not only developments are needed in each individual area, but concerted efforts to interface multiple functional parts at a systems level should be pursued. With all the combined efforts, we can foresee a future in which electroconversion of CO_2 to value-added products leads the era of sustainability.

References

(1) U.S. Energy Information Administration. *International Energy Outlook 2013*; 2013.

(2) Licht, S.; Cui, B.; Wang, B.; Li, F.-F.; Lau, J.; Liu, S. Ammonia Synthesis by N_2 and Steam Electrolysis in Molten Hydroxide Suspensions of Nanoscale Fe_2O_3. *Science* **2014**, *345* (6197), 637–640.

(3) Liu, C.; Dasgupta, N. P.; Yang, P. Semiconductor Nanowires for Artificial Photosynthesis. *Chem. Mater.* **2014**, *26* (1), 415–422.

(4) Fujishima, A.; Honda, K. Electrochemical Photolysis of Water at a Semiconductor Electrode. *Nature* **1972**, *238* (5358), 37–38.

(5) Qiao, J.; Liu, Y.; Hong, F.; Zhang, J. A Review of Catalysts for the Electroreduction of Carbon Dioxide to Produce Low-Carbon Fuels. *Chem. Soc. Rev.* **2014**, *43* (2), 631–675.

(6) Aresta, M.; Dibenedetto, A.; Angelini, A. Catalysis for the Valorization of Exhaust Carbon: From CO_2 to Chemicals, Materials, and Fuels. Technological Use of CO_2. *Chem. Rev.* **2014**, *114* (3), 1709–1742.

(7) Gattrell, M.; Gupta, N.; Co, A. A Review of the Aqueous Electrochemical Reduction of CO_2 to Hydrocarbons at Copper. *J. Electroanal. Chem.* **2006**, *594* (1), 1–19.

(8) Hori, Y. Electrochemical CO_2 Reduction on Metal Electrodes. In *Modern Aspects of Electrochemistry*; Springer New York: New York, NY, 2008; pp 89–189.

(9) Kuhl, K. P.; Cave, E. R.; Abram, D. N.; Jaramillo, T. F. New Insights into the Electrochemical Reduction of Carbon Dioxide on Metallic Copper Surfaces. *Energy Environ. Sci.* **2012**, *5* (5), 7050.

(10) Mistry, H.; Varela, A. S.; Kühl, S.; Strasser, P.; Cuenya, B. R. Nanostructured Electrocatalysts with Tunable Activity and Selectivity. *Nat. Rev. Mater.* **2016**, *1* (4), 16009.

(11) Koper, M. T. M. Thermodynamic Theory of Multi-Electron Transfer Reactions: Implications for Electrocatalysis. *J. Electroanal. Chem.* **2011**, *660* (2), 254.

(12) Schouten, K. J. P.; Calle-Vallejo, F.; Koper, M. T. M. A Step Closer to the Electrochemical Production of Liquid Fuels. *Angew. Chemie Int. Ed.* **2014**, *53* (41), 10858–10860.

(13) Kortlever, R.; Shen, J.; Schouten, K. J. P.; Calle-Vallejo, F.; Koper, M. T. M. Catalysts and Reaction Pathways for the Electrochemical Reduction of Carbon Dioxide. *J. Phys. Chem. Lett.* **2015**, *6* (20), 4073–4082.

(14) Li, X.; Hao, X.; Abudula, A.; Guan, G. Nanostructured Catalysts for Electrochemical Water Splitting: Current State and Prospects. *J. Mater. Chem. A* **2016**, *4* (31), 11973–12000.

(15) Chen, Y.; Li, C. W.; Kanan, M. W. Aqueous CO_2 Reduction at Very Low Overpotential on Oxide-Derived Au Nanoparticles. *J. Am. Chem. Soc.* **2012**, *134* (49), 19969–19972.

(16) Lu, Q.; Rosen, J.; Zhou, Y.; Hutchings, G. S.; Kimmel, Y. C.; Chen, J. G.; Jiao, F. A Selective and Efficient Electrocatalyst for Carbon Dioxide Reduction. *Nat. Commun.* **2014**, *5*, 3242.

(17) Hori, Y.; Murata, A.; Kikuchi, K.; Suzuki, S. Electrochemical Reduction of Carbon Dioxides to Carbon Monoxide at a Gold Electrode in Aqueous Potassium Hydrogen Carbonate. *J. Chem. Soc. Chem. Commun.* **1987**, No. 10, 728.

(18) Noda, H.; Ikeda, S.; Yamamoto, A.; Einaga, H.; Ito, K. Kinetics of Electrochemical Reduction of Carbon Dioxide on a Gold Electrode in Phosphate Buffer Solutions. *Bull. Chem. Soc. Jpn.* **1995**, *68* (7), 1889–1895.

(19) Hatsukade, T.; Kuhl, K. P.; Cave, E. R.; Abram, D. N.; Jaramillo, T. F. Insights into the Electrocatalytic Reduction of CO_2 on Metallic Silver Surfaces. *Phys. Chem. Chem. Phys.* **2014**, *16* (27), 13814–13819.

(20) Rosen, J.; Hutchings, G. S.; Lu, Q.; Rivera, S.; Zhou, Y.; Vlachos, D. G.; Jiao, F. Mechanistic Insights into the Electrochemical Reduction of CO_2 to CO on Nanostructured Ag Surfaces. *ACS Catal.* **2015**, *5* (7), 4293–4299.

(21) Firet, N. J.; Smith, W. A. Probing the Reaction Mechanism of CO_2 Electroreduction over Ag Films via Operando Infrared Spectroscopy. *ACS Catal.* **2017**, *7* (1), 606–612.

(22) Wuttig, A.; Yoon, Y.; Ryu, J.; Surendranath, Y. Bicarbonate Is Not a General Acid in Au-Catalyzed CO_2 Electroreduction. *J. Am. Chem. Soc.* **2017**, *139* (47), 17109–17113.

(23) Wuttig, A.; Yaguchi, M.; Motobayashi, K.; Osawa, M.; Surendranath, Y. Inhibited Proton Transfer Enhances Au-Catalyzed CO_2-to-Fuels Selectivity. *Proc. Natl. Acad. Sci. U. S. A.* **2016**, *113* (32), E4585-93.

(24) Lee, C. W.; Cho, N. H.; Yang, K. D.; Nam, K. T. Reaction Mechanisms of the Electrochemical Conversion of Carbon Dioxide to Formic Acid on Tin Oxide Electrodes. *ChemElectroChem* **2017**, *4* (9), 2130–2136.

(25) Feaster, J. T.; Shi, C.; Cave, E. R.; Hatsukade, T.; Abram, D. N.; Kuhl, K. P.; Hahn, C.; Nørskov, J. K.; Jaramillo, T. F. Understanding Selectivity for the Electrochemical Reduction of Carbon Dioxide to Formic Acid and Carbon Monoxide on Metal Electrodes. *ACS Catal.* **2017**, *7* (7), 4822–4827.

(26) Yoo, J. S.; Christensen, R.; Vegge, T.; Nørskov, J. K.; Studt, F. Theoretical Insight into the Trends That Guide the Electrochemical Reduction of Carbon Dioxide to Formic Acid. *ChemSusChem* **2016**, *9* (4), 358–363.

(27) Chen, Y.; Kanan, M. W. Tin Oxide Dependence of the CO_2 Reduction Efficiency on

Tin Electrodes and Enhanced Activity for Tin/tin Oxide Thin-Film Catalysts. *J. Am. Chem. Soc.* **2012**, *134* (4), 1986–1989.

(28) Dutta, A.; Kuzume, A.; Rahaman, M.; Vesztergom, S.; Broekmann, P. Monitoring the Chemical State of Catalysts for CO_2 Electroreduction: An In Operando Study. *ACS Catal.* **2015**, *5* (12), 7498–7502.

(29) Baruch, M. F.; Pander, J. E.; White, J. L.; Bocarsly, A. B. Mechanistic Insights into the Reduction of CO_2 on Tin Electrodes Using in Situ ATR-IR Spectroscopy. *ACS Catal.* **2015**, *5* (5), 3148–3156.

(30) Detweiler, Z. M.; White, J. L.; Bernasek, S. L.; Bocarsly, A. B. Anodized Indium Metal Electrodes for Enhanced Carbon Dioxide Reduction in Aqueous Electrolyte. *Langmuir* **2014**, *30* (25), 7593–7600.

(31) Pander, J. E.; Baruch, M. F.; Bocarsly, A. B. Probing the Mechanism of Aqueous CO_2 Reduction on Post-Transition-Metal Electrodes Using ATR-IR Spectroelectrochemistry. *ACS Catal.* **2016**, *6* (11), 7824–7833.

(32) Lee, C. H.; Kanan, M. W. Controlling H^+ vs CO_2 Reduction Selectivity on Pb Electrodes. *ACS Catal.* **2015**, *5* (1), 465–469.

(33) Adams, B. D.; Chen, A. The Role of Palladium in a Hydrogen Economy. *Mater. Today* **2011**, *14* (6), 282–289.

(34) Min, X.; Kanan, M. W. Pd-Catalyzed Electrohydrogenation of Carbon Dioxide to Formate: High Mass Activity at Low Overpotential and Identification of the Deactivation Pathway. *J. Am. Chem. Soc.* **2015**, *137* (14), 4701–4708.

(35) Cheng, T.; Xiao, H.; Goddard, W. A. Full Atomistic Reaction Mechanism with Kinetics for CO Reduction on Cu(100) from Ab Initio Molecular Dynamics Free-Energy Calculations at 298 K. *Proc. Natl. Acad. Sci.* **2017**, *114* (8), 1795–1800.

(36) Cheng, T.; Xiao, H.; Goddard, W. A. Free-Energy Barriers and Reaction Mechanisms for the Electrochemical Reduction of CO on the Cu(100) Surface, Including Multiple Layers of Explicit Solvent at pH 0. *J. Phys. Chem. Lett.* **2015**, *6* (23), 4767–4773.

(37) Nie, X.; Esopi, M. R.; Janik, M. J.; Asthagiri, A. Selectivity of CO_2 Reduction on Copper Electrodes: The Role of the Kinetics of Elementary Steps. *Angew. Chemie Int. Ed.* **2013**, *52* (9), 2459–2462.

(38) Schouten, K. J. P.; Kwon, Y.; van der Ham, C. J. M.; Qin, Z.; Koper, M. T. M. A New Mechanism for the Selectivity to C1 and C2 Species in the Electrochemical Reduction of Carbon Dioxide on Copper Electrodes. *Chem. Sci.* **2011**, *2* (10), 1902.

(39) Peterson, A. A.; Abild-Pedersen, F.; Studt, F.; Rossmeisl, J.; Nørskov, J. K. How Copper Catalyzes the Electroreduction of Carbon Dioxide into Hydrocarbon Fuels. *Energy Environ. Sci.* **2010**, *3* (9), 1311.

(40) Kuhl, K. P.; Hatsukade, T.; Cave, E. R.; Abram, D. N.; Kibsgaard, J.; Jaramillo, T. F. Electrocatalytic Conversion of Carbon Dioxide to Methane and Methanol on Transition Metal Surfaces. *J. Am. Chem. Soc.* **2014**, *136* (40), 14107–14113.

(41) Hori, Y.; Kikuchi, K.; Suzuki, S. Production of CO and CH_4 in Electrochemical Reduction of CO_2 at Metal Electrodes in Aqueous Hydrogen Carbonate Solution. *Chem. Lett.* **1985**, *14* (11), 1695–1698.

(42) Cook, R. L. Evidence for Formaldehyde, Formic Acid, and Acetaldehyde as Possible Intermediates during Electrochemical Carbon Dioxide Reduction at Copper. *J. Electrochem. Soc.* **1989**, *136* (7), 1982.

(43) DeWulf, D. W. Electrochemical and Surface Studies of Carbon Dioxide Reduction to Methane and Ethylene at Copper Electrodes in Aqueous Solutions. *J. Electrochem. Soc.* **1989**, *136* (6), 1686.

(44) Gao, D.; Zegkinoglou, I.; Divins, N. J.; Scholten, F.; Sinev, I.; Grosse, P.; Roldan Cuenya, B. Plasma-Activated Copper Nanocube Catalysts for Efficient Carbon Dioxide Electroreduction to Hydrocarbons and Alcohols. *ACS Nano* **2017**, *11* (5), 4825–4831.

(45) Kim, D.; Kley, C. S.; Li, Y.; Yang, P. Copper Nanoparticle Ensembles for Selective Electroreduction of CO_2 to C_2–C_3 Products. *Proc. Natl. Acad. Sci.* **2017**, *114* (40), 10560–10565.

(46) Han, Z.; Kortlever, R.; Chen, H.-Y.; Peters, J. C.; Agapie, T. CO_2 Reduction Selective for $C \geq 2$ Products on Polycrystalline Copper with N-Substituted Pyridinium Additives. *ACS Cent. Sci.* **2017**, *3* (8), 853–859.

(47) Cook, R. L. On the Electrochemical Reduction of Carbon Dioxide at In Situ Electrodeposited Copper. *J. Electrochem. Soc.* **1988**, *135* (6), 1320.

(48) Friebe, P.; Bogdanoff, P.; Alonso-Vante, N.; Tributsch, H. A Real-Time Mass Spectroscopy Study of the (Electro)chemical Factors Affecting CO_2 Reduction at Copper. *J. Catal.* **1997**, *168* (2), 374–385.

(49) Hori, Y.; Takahashi, R.; Yoshinami, Y.; Murata, A. Electrochemical Reduction of CO at a Copper Electrode. *J. Phys. Chem. B* **1997**, *101* (36), 7075–7081.

(50) Schouten, K. J. P.; Qin, Z.; Pérez Gallent, E.; Koper, M. T. M. Two Pathways for the Formation of Ethylene in CO Reduction on Single-Crystal Copper Electrodes. *J. Am. Chem. Soc.* **2012**, *134* (24), 9864–9867.

(51) Schouten, K. J. P.; Pérez Gallent, E.; Koper, M. T. M. Structure Sensitivity of the Electrochemical Reduction of Carbon Monoxide on Copper Single Crystals. *ACS Catal.* **2013**, *3* (6), 1292–1295.

(52) Calle-Vallejo, F.; Koper, M. T. M. Theoretical Considerations on the Electroreduction of CO to C2 Species on Cu(100) Electrodes. *Angew. Chemie Int. Ed.* **2013**, *52* (28), 7282–7285.

(53) Ou, L.; Long, W.; Chen, Y.; Jin, J. New Reduction Mechanism of CO Dimer by Hydrogenation to C_2H_4 on a Cu(100) Surface: Theoretical Insight into the Kinetics of the Elementary Steps. *RSC Adv.* **2015**, *5* (117), 96281–96289.

(54) Goodpaster, J. D.; Bell, A. T.; Head-Gordon, M. Identification of Possible Pathways for C-C Bond Formation during Electrochemical Reduction of CO_2: New Theoretical Insights from an Improved Electrochemical Model. *J. Phys. Chem. Lett.* **2016**, *7* (8), 1471–1477.

(55) Garza, A. J.; Bell, A. T.; Head-Gordon, M. Mechanism of CO_2 Reduction at Copper Surfaces: Pathways to C_2 Products. *ACS Catal.* **2018**, *8* (2), 1490–1499.

(56) Pérez-Gallent, E.; Figueiredo, M. C.; Calle-Vallejo, F.; Koper, M. T. M. Spectroscopic Observation of a Hydrogenated CO Dimer Intermediate During CO Reduction on Cu(100) Electrodes. *Angew. Chemie Int. Ed.* **2017**, *56* (13), 3621–3624.

(57) Francke, R.; Schille, B.; Roemelt, M. Homogeneously Catalyzed Electroreduction of Carbon Dioxide—Methods, Mechanisms, and Catalysts. *Chem. Rev.* **2018**, acs.chemrev.7b00459.

(58) Jitaru, M.; Lowy, D. A.; Toma, M.; Toma, B. C.; Oniciu, L. Electrochemical Reduction of Carbon Dioxide on Flat Metallic Cathodes. *J. Appl. Electrochem.* **1997**, *27* (8), 875–889.

(59) Peterson, A. A.; Nørskov, J. K. Activity Descriptors for CO_2 Electroreduction to Methane on Transition-Metal Catalysts. *J. Phys. Chem. Lett.* **2012**, *3* (2), 251–258.

(60) Hansen, H. A.; Varley, J. B.; Peterson, A. A.; Nørskov, J. K. Understanding Trends in the Electrocatalytic Activity of Metals and Enzymes for CO_2 Reduction to CO. *J. Phys. Chem. Lett.* **2013**, *4* (3), 388–392.

(61) Shi, C.; Hansen, H. a; Lausche, A. C.; Nørskov, J. K. Trends in Electrochemical CO_2 Reduction Activity for Open and Close-Packed Metal Surfaces. *Phys. Chem. Chem. Phys.* **2014**, *16* (10), 4720–4727.

(62) Gupta, N.; Gattrell, M.; MacDougall, B. Calculation for the Cathode Surface Concentrations in the Electrochemical Reduction of CO_2 in $KHCO_3$ solutions. *J. Appl. Electrochem.* **2006**, *36* (2), 161–172.

(63) Varela, A. S.; Kroschel, M.; Reier, T.; Strasser, P. Controlling the Selectivity of CO_2 Electroreduction on Copper: The Effect of the Electrolyte Concentration and the Importance of the Local pH. *Catal. Today* **2016**, *260*, 8–13.

(64) Kyriacou, G. Z.; Anagnostopoulos, A. K. Influence CO_2 Partial Pressure and the Supporting Electrolyte Cation on the Product Distribution in CO_2 Electroreduction. *J. Appl. Electrochem.* **1993**, *23* (5), 483–486.

(65) Murata, A.; Hori, Y. Product Selectivity Affected by Cationic Species in Electrochemical Reduction of CO_2 and CO at a Cu Electrode. *Bulletin of the Chemical Society of Japan*. 1991, pp 123–127.

(66) Singh, M. R.; Kwon, Y.; Lum, Y.; Ager, J. W.; Bell, A. T. Hydrolysis of Electrolyte Cations Enhances the Electrochemical Reduction of CO_2 over Ag and Cu. *J. Am. Chem. Soc.* **2016**, *138* (39), 13006–13012.

(67) Ayemoba, O.; Cuesta, A. Spectroscopic Evidence of Size-Dependent Buffering of Interfacial pH by Cation Hydrolysis during CO_2 Electroreduction. *ACS Appl. Mater. Interfaces* **2017**, *9* (33), 27377–27382.

(68) Akhade, S. A.; McCrum, I. T.; Janik, M. J. The Impact of Specifically Adsorbed Ions on the Copper-Catalyzed Electroreduction of CO_2. *J. Electrochem. Soc.* **2016**, *163* (6), F477–F484.

(69) Resasco, J.; Chen, L. D.; Clark, E.; Tsai, C.; Hahn, C.; Jaramillo, T. F.; Chan, K.; Bell, A. T. Promoter Effects of Alkali Metal Cations on the Electrochemical Reduction of Carbon Dioxide. *J. Am. Chem. Soc.* **2017**, *139* (32), 11277–11287.

(70) Chen, L. D.; Urushihara, M.; Chan, K.; Nørskov, J. K. Electric Field Effects in Electrochemical CO_2 Reduction. *ACS Catal.* **2016**, *6* (10), 7133–7139.

(71) Kas, R.; Kortlever, R.; Yılmaz, H.; Koper, M. T. M.; Mul, G. Manipulating the Hydrocarbon Selectivity of Copper Nanoparticles in CO_2 Electroreduction by Process Conditions. *ChemElectroChem* **2015**, *2* (3), 354–358.

(72) Lobaccaro, P.; Singh, M. R.; Clark, E. L.; Kwon, Y.; Bell, A. T.; Ager, J. W. Effects of Temperature and Gas–liquid Mass Transfer on the Operation of Small Electrochemical Cells for the Quantitative Evaluation of CO_2 Reduction Electrocatalysts. *Phys. Chem. Chem. Phys.* **2016**.

(73) Hori, Y.; Konishi, H.; Futamura, T.; Murata, A.; Koga, O.; Sakurai, H.; Oguma, K. “Deactivation of Copper Electrode” in Electrochemical Reduction of CO_2. *Electrochim. Acta* **2005**, *50* (27), 5354–5369.

(74) Wuttig, A.; Surendranath, Y. Impurity Ion Complexation Enhances Carbon Dioxide Reduction Catalysis. *ACS Catal.* **2015**, *5* (7), 4479–4484.

(75) Lum, Y.; Kwon, Y.; Lobaccaro, P.; Chen, L.; Clark, E. L.; Bell, A. T.; Ager, J. W. Trace Levels of Copper in Carbon Materials Show Significant Electrochemical CO_2 Reduction Activity. *ACS Catal.* **2016**, *6* (1), 202–209.

(76) Kyriacou, G.; Anagnostopoulos, A. Electroreduction of CO_2 on Differently Prepared Copper Electrodes. *J. Electroanal. Chem.* **1992**, *322* (1–2), 233–246.

(77) Xu, Z.; Lai, E.; Shao-Horn, Y.; Hamad-Schifferli, K. Compositional Dependence of the Stability of AuCu Alloy Nanoparticles. *Chem Commun* **2012**, *48* (111), 5626–5628.

(78) Xie, J.; Peng, S.; Brower, N.; Pourmand, N.; Wang, S. X.; Sun, S. One-Pot Synthesis of Monodisperse Iron Oxide Nanoparticles for Potential Biomedical Applications. *Pure Appl. Chem.* **2006**, *78* (5), 1003–1014.

(79) Sra, A. K.; Ewers, T. D.; Schaak, R. E. Direct Solution Synthesis of Intermetallic AuCu and $AuCu_3$ Nanocrystals and Nanowire Networks. *Chem. Mater.* **2005**, *17* (4), 758–766.

(80) Rice, K. P.; Walker, E. J.; Stoykovich, M. P.; Saunders, A. E. Solvent-Dependent Surface Plasmon Response and Oxidation of Copper Nanocrystals. *J. Phys. Chem. C* **2011**, *115* (5), 1793–1799.

(81) Motl, N. E.; Ewusi-Annan, E.; Sines, I. T.; Jensen, L.; Schaak, R. E. Au-Cu Alloy Nanoparticles with Tunable Compositions and Plasmonic Properties: Experimental Determination of Composition and Correlation with Theory. *J. Phys. Chem. C* **2010**, *114* (45), 19263–19269.

(82) Yamada, Y.; Tsung, C.-K.; Huang, W.; Huo, Z.; Habas, S. E.; Soejima, T.; Aliaga, C. E.; Somorjai, G. A.; Yang, P. Nanocrystal Bilayer for Tandem Catalysis. *Nat. Chem.* **2011**, *3* (5), 372–376.

(83) Liu, S.; Tang, Z. Nanoparticle assemblies for Biological and Chemical Sensing. *J. Mater. Chem.* **2010**, *20* (1), 24–35.

(84) Wen, T.; Majetich, S. A. Ultra-Large-Area Self-Assembled Monolayers of Nanoparticles. *ACS Nano* **2011**, *5* (11), 8868–8876.

(85) Zhu, W.; Michalsky, R.; Metin, Ö.; Lv, H.; Guo, S.; Wright, C. J.; Sun, X.; Peterson, A. A; Sun, S. Monodisperse Au Nanoparticles for Selective Electrocatalytic Reduction of CO_2 to CO. *J. Am. Chem. Soc.* **2013**, *135* (45), 16833–16836.

(86) Nørskov, J. K.; Bligaard, T.; Rossmeisl, J.; Christensen, C. H. Towards the Computational Design of Solid Catalysts. *Nat. Chem.* **2009**, *1* (1), 37–46.

(87) Nemoshkalenko, V. V.; Chuistov, K. V.; Aleshin, V. G.; Senkevich, A. I. Changes in Energy Structure of Cu_3Au and $CuAu_3$ Alloy Studied by the Method of X-Ray Photoelectron Spectroscopy. *J. Electron Spectros. Relat. Phenomena* **1976**, *9*, 169–173.

(88) Siahrostami, S.; Verdaguer-Casadevall, A.; Karamad, M.; Deiana, D.; Malacrida, P.; Wickman, B.; Escudero-Escribano, M.; Paoli, E. A.; Frydendal, R.; Hansen, T. W.; et al. Enabling Direct H_2O_2 production through Rational Electrocatalyst Design. *Nat. Mater.* **2013**, *12* (12), 1137–1143.

(89) Nørskov, J. K.; Bligaard, T.; Logadottir, A.; Kitchin, J. R.; Chen, J. G.; Pandelov, S.; Stimming, U. Trends in the Exchange Current for Hydrogen Evolution. *J. Electrochem. Soc.* **2005**, *152* (3), J23.

(90) Tornow, C. E.; Thorson, M. R.; Ma, S.; Gewirth, A. A.; Kenis, P. J. A. Nitrogen-Based Catalysts for the Electrochemical Reduction of CO_2 to CO. *J. Am. Chem. Soc.* **2012**, *134* (48), 19520–19523.

(91) Porter, D. A.; Easterling, K. E.; Sherif, M. Y. *Phase Transformations in Metals and Alloys*, 3rd ed.; CRC Press, 2009.

(92) Chen, W.; Yu, R.; Li, L.; Wang, A.; Peng, Q.; Li, Y. A Seed-Based Diffusion Route to Monodisperse Intermetallic CuAu Nanocrystals. *Angew. Chemie Int. Ed.* **2010**, *49* (16), 2917–2921.

(93) Jia, Q.; Caldwell, K.; Ramaker, D. E.; Ziegelbauer, J. M.; Liu, Z.; Yu, Z.; Trahan, M.; Mukerjee, S. In Situ Spectroscopic Evidence for Ordered Core–Ultrathin Shell Pt_1Co_1 Nanoparticles with Enhanced Activity and Stability as Oxygen Reduction Electrocatalysts. *J. Phys. Chem. C* **2014**, *118* (35), 20496–20503.

(94) Kim, J.; Lee, Y.; Sun, S. Structurally Ordered FePt Nanoparticles and Their Enhanced Catalysis for Oxygen Reduction Reaction. *J. Am. Chem. Soc.* **2010**, *132* (14), 4996–4997.

(95) Li, Q.; Wu, L.; Wu, G.; Su, D.; Lv, H.; Zhang, S.; Zhu, W.; Casimir, A.; Zhu, H.; Mendoza-Garcia, A.; et al. New Approach to Fully Ordered Fct-FePt Nanoparticles for Much Enhanced Electrocatalysis in Acid. *Nano Lett.* **2015**, *15* (4), 2468–2473.

(96) Prabhudev, S.; Bugnet, M.; Bock, C.; Botton, G. a. Strained Lattice with Persistent Atomic Order in Pt_3Fe_2 Intermetallic Core–Shell Nanocatalysts. *ACS Nano* **2013**, *7* (7), 6103–6110.

(97) Sra, A. K.; Ewers, T. D.; Schaak, R. E. Direct Solution Synthesis of Intermetallic AuCu and $AuCu_3$ Nanocrystals and Nanowire Networks. *Chem. Mater.* **2005**, *17* (4), 758–766.

(98) Sra, A. K.; Schaak, R. E. Synthesis of Atomically Ordered AuCu and $AuCu_3$ Nanocrystals from Bimetallic Nanoparticle Precursors. *J. Am. Chem. Soc.* **2004**, *126* (21), 6667–6672.

(99) Wang, D.; Xin, H. L.; Hovden, R.; Wang, H.; Yu, Y.; Muller, D. A.; DiSalvo, F. J.; Abruña, H. D. Structurally Ordered Intermetallic Platinum–cobalt Core–shell Nanoparticles with Enhanced Activity and Stability as Oxygen Reduction Electrocatalysts. *Nat. Mater.* **2012**, *12* (1), 81–87.

(100) Wang, G.; Xiao, L.; Huang, B.; Ren, Z.; Tang, X.; Zhuang, L.; Lu, J. AuCu Intermetallic Nanoparticles: Surfactant-Free Synthesis and Novel Electrochemistry. *J. Mater. Chem.* **2012**, *22* (31), 15769.

(101) Zhang, N.; Chen, X.; Lu, Y.; An, L.; Li, X.; Xia, D.; Zhang, Z.; Li, J. Nano-Intermetallic $AuCu_3$ Catalyst for Oxygen Reduction Reaction: Performance and Mechanism. *Small* **2014**, *10* (13), 2662–2669.

(102) Cullity, B. D.; Stock, S. R. *Elements of X-Ray Diffraction*, 3rd ed.; Pearson, 2001.

(103) Kim, D.; Resasco, J.; Yu, Y.; Asiri, A. M.; Yang, P. Synergistic Geometric and Electronic Effects for Electrochemical Reduction of Carbon Dioxide Using Gold–copper Bimetallic Nanoparticles. *Nat. Commun.* **2014**, *5* (May), 4948.

(104) Sinfelt, J. H.; Via, G. H.; Lytle, F. W. Structure of Bimetallic Clusters. Extended X-ray Absorption Fine Structure (EXAFS) Studies of Ru–Cu Clusters. *J. Chem. Phys.*

1980, *72* (9), 4832–4844.

(105) Knauer, A.; Eisenhardt, A.; Krischok, S.; Koehler, J. M. Nanometer Precise Adjustment of the Silver Shell Thickness during Automated Au–Ag Core–shell Nanoparticle Synthesis in Micro Fluid Segment Sequences. *Nanoscale* **2014**, *6* (10), 5230.

(106) Ma, S.; Sadakiyo, M.; Heima, M.; Luo, R.; Haasch, R. T.; Gold, J. I.; Yamauchi, M.; Kenis, P. J. A. Electroreduction of Carbon Dioxide to Hydrocarbons Using Bimetallic Cu–Pd Catalysts with Different Mixing Patterns. *J. Am. Chem. Soc.* **2017**, *139* (1), 47–50.

(107) Verma, S.; Kim, B.; Jhong, H. R. M.; Ma, S.; Kenis, P. J. A. A Gross-Margin Model for Defining Technoeconomic Benchmarks in the Electroreduction of CO_2. *ChemSusChem* **2016**, No. 2, 1972–1979.

(108) Zhu, W.; Zhang, Y.-J.; Zhang, H.; Lv, H.; Li, Q.; Michalsky, R.; Peterson, A. A.; Sun, S. Active and Selective Conversion of CO_2 to CO on Ultrathin Au Nanowires. *J. Am. Chem. Soc.* **2014**, *136* (46), 16132–16135.

(109) Feng, X.; Jiang, K.; Fan, S.; Kanan, M. W. Grain-Boundary-Dependent CO_2 Electroreduction Activity. *J. Am. Chem. Soc.* **2015**, *137* (14), 4606–4609.

(110) Kauffman, D. R.; Alfonso, D.; Matranga, C.; Qian, H.; Jin, R. Experimental and Computational Investigation of Au_{25} Clusters and CO_2: A Unique Interaction and Enhanced Electrocatalytic Activity. *J. Am. Chem. Soc.* **2012**, *134* (24), 10237–10243.

(111) Liu, M.; Pang, Y.; Zhang, B.; De Luna, P.; Voznyy, O.; Xu, J.; Zheng, X.; Dinh, C. T.; Fan, F.; Cao, C.; et al. Enhanced Electrocatalytic CO_2 Reduction via Field-Induced Reagent Concentration. *Nature* **2016**, *537* (7620), 382–386.

(112) Escudero-Escribano, M.; Verdaguer-Casadevall, A.; Malacrida, P.; Grønbjerg, U.; Knudsen, B. P.; Jepsen, A. K.; Rossmeisl, J.; Stephens, I. E. L.; Chorkendorff, I. Pt_5Gd as a Highly Active and Stable Catalyst for Oxygen Electroreduction. *J. Am. Chem. Soc.* **2012**, *134* (40), 16476–16479.

(113) Stephens, I. E. L.; Bondarenko, A. S.; Grønbjerg, U.; Rossmeisl, J.; Chorkendorff, I. Understanding the Electrocatalysis of Oxygen Reduction on Platinum and Its Alloys. *Energy Environ. Sci.* **2012**, *5* (5), 6744.

(114) Strasser, P.; Koh, S.; Anniyev, T.; Greeley, J.; More, K.; Yu, C.; Liu, Z.; Kaya, S.; Nordlund, D.; Ogasawara, H.; et al. Lattice-Strain Control of the Activity in Dealloyed Core–shell Fuel Cell Catalysts. *Nat. Chem.* **2010**, *2* (6), 454–460.

(115) Kitchin, J. R.; Nørskov, J. K.; Barteau, M. A.; Chen, J. G. Modification of the Surface Electronic and Chemical Properties of Pt(111) by Subsurface 3d Transition Metals. *J. Chem. Phys.* **2004**, *120* (21), 10240–10246.

(116) Greeley, J.; Nørskov, J. K.; Kibler, L. A.; El-Aziz, A. M.; Kolb, D. M. Hydrogen Evolution over Bimetallic Systems: Understanding the Trends. *ChemPhysChem*

2006, *7* (5), 1032–1035.

(117) Greeley, J.; Jaramillo, T. F.; Bonde, J.; Chorkendorff, I. B.; Nørskov, J. K. Computational High-Throughput Screening of Electrocatalytic Materials for Hydrogen Evolution. *Nat. Mater.* **2006**, *5* (11), 909–913.

(118) Wang, S.; Petzold, V.; Tripkovic, V.; Kleis, J.; Howalt, J. G.; Skúlason, E.; Fernández, E. M.; Hvolbæk, B.; Jones, G.; Toftelund, A.; et al. Universal Transition State Scaling Relations for (De)hydrogenation over Transition Metals. *Phys. Chem. Chem. Phys.* **2011**, *13* (46), 20760.

(119) Choi, S. K.; Kang, U.; Lee, S.; Ham, D. J.; Ji, S. M.; Park, H. Sn-Coupled p-Si Nanowire Arrays for Solar Formate Production from CO_2. *Adv. Energy Mater.* **2014**, *4* (11), 1–7.

(120) Qiu, J.; Zeng, G.; Ha, M.-A.; Ge, M.; Lin, Y.; Hettick, M.; Hou, B.; Alexandrova, A. N.; Javey, A.; Cronin, S. B. Artificial Photosynthesis on TiO_2-Passivated InP Nanopillars. *Nano Lett.* **2015**, *15* (9), 6177-6181.

(121) Schreier, M.; Luo, J.; Gao, P.; Moehl, T.; Mayer, M. T.; Grätzel, M. Covalent Immobilization of a Molecular Catalyst on Cu_2O Photocathodes for CO_2 Reduction. *J. Am. Chem. Soc.* **2016**, *138* (6), 1938–1946.

(122) Torralba-Peñalver, E.; Luo, Y.; Compain, J.-D.; Chardon-Noblat, S.; Fabre, B. Selective Catalytic Electroreduction of CO_2 at Silicon Nanowires (SiNWs) Photocathodes Using Non-Noble Metal-Based Manganese Carbonyl Bipyridyl Molecular Catalysts in Solution and Grafted onto SiNWs. *ACS Catal.* **2015**, 6138–6147.

(123) Gao, D.; Zhou, H.; Wang, J.; Miao, S.; Yang, F.; Wang, G.; Wang, J.; Bao, X. Size-Dependent Electrocatalytic Reduction of CO_2 over Pd Nanoparticles. *J. Am. Chem. Soc.* **2015**, *137* (13), 4288–4291.

(124) Yunker, P. J.; Still, T.; Lohr, M. A.; Yodh, A. G. Suppression of the Coffee-Ring Effect by Shape-Dependent Capillary Interactions. *Nature* **2011**, *476* (7360), 308–311.

(125) Huang, J.; Kim, F.; Tao, A. R.; Connor, S.; Yang, P. Spontaneous Formation of Nanoparticle Stripe Patterns through Dewetting. *Nat. Mater.* **2005**, *4* (12), 896–900.

(126) Glelche, M.; Chi, L. F.; Fuchs, H. Nanoscopic Channel Lattices with Controlled Anisotropic Wetting. *Nature* **2000**, *403* (6766), 173–175.

(127) Zheng, N.; Stucky, G. D. A General Synthetic Strategy for Oxide-Supported Metal Nanoparticle Catalysts. *J. Am. Chem. Soc.* **2006**, *128* (44), 14278–14280.

(128) Rabani, E.; Reichman, D. R.; Geissler, P. L.; Brus, L. E. Drying-Mediated Self-Assembly of Nanoparticles. *Nature* **2003**, *426* (6964), 271–274.

(129) Su, Y.; Liu, C.; Brittman, S.; Tang, J.; Fu, A.; Kornienko, N.; Kong, Q.; Yang, P.

Single-Nanowire Photoelectrochemistry. *Nat. Nanotechnol.* **2016**, *11* (7), 609–612.

(130) Walter, M. G.; Warren, E. L.; McKone, J. R.; Boettcher, S. W.; Mi, Q.; Santori, E. A.; Lewis, N. S. Solar Water Splitting Cells. *Chem. Rev.* **2010**, *110* (11), 6446–6473.

(131) Cavka, J. H.; Olsbye, U.; Guillou, N.; Bordiga, S.; Lillerud, K. P. A New Zirconium Inorganic Building Brick Forming Metal Organic Frameworks with Exceptional Stability. *J. Am. Chem. Soc.* **2008**, *6*, 1–19.

(132) Sato, S.; Morimoto, T.; Ishitani, O. Photochemical Synthesis of Mer -[Re(bpy)$(CO)_3$ Cl]. *Inorg. Chem.* **2007**, *46* (22), 9051–9053.

(133) Blake, A. J.; Champness, N. R.; Easun, T. L.; Allan, D. R.; Nowell, H.; George, M. W.; Jia, J.; Sun, X.-Z. Photoreactivity Examined through Incorporation in Metal−organic Frameworks. *Nat. Chem.* **2010**, *2* (8), 688–694.

(134) Wang, C.; Xie, Z.; Dekrafft, K. E.; Lin, W. Doping Metal-Organic Frameworks for Water Oxidation, Carbon Dioxide Reduction, and Organic Photocatalysis. *J. Am. Chem. Soc.* **2011**, *133* (34), 13445–13454.

(135) Benson, E. E.; Kubiak, C. P. Structural Investigations into the Deactivation Pathway of the CO_2 Reduction Electrocatalyst Re(bpy)$(CO)_3$Cl. *Chem. Commun.* **2012**, *48* (59), 7374.

(136) Zhao, H. C.; Mello, B.; Fu, B. L.; Chowdhury, H.; Szalda, D. J.; Tsai, M. K.; Grills, D. C.; Rochford, J. Investigation of Monomeric versus Dimeric Fac-rhenium(I) Tricarbonyl Systems Containing the Noninnocent 8-Oxyquinolate Ligand. *Organometallics* **2013**, *32* (6), 1832–1841.

(137) Hayashi, Y.; Kita, S.; Brunschwig, B. S.; Fujita, E. Involvement of a Binuclear Species with the Re−C(O)O−Re Moiety in CO_2 Reduction Catalyzed by Tricarbonyl Rhenium(I) Complexes with Diimine Ligands: Strikingly Slow Formation of the Re−Re and Re−C(O)O−Re Species from Re(dmb)$(CO)_3$S (Dmb = 4,4‘-Dimethyl-2. *J. Am. Chem. Soc.* **2003**, *125* (39), 11976–11987.

(138) Gibson, D. H.; Yin, X.; He, H.; Mashuta, M. S. Synthesis and Reactions of Fac-[Re(dmbpy)$(CO)_3$X] (Dmbpy = 4,4′-Dimethyl-2,2′-Bipyridine; X = COOH, CHO) and Their Derivatives. *Organometallics* **2003**, *22* (2), 337–346.

(139) Meister, S.; Reithmeier, R. O.; Tschurl, M.; Heiz, U.; Rieger, B. Unraveling Side Reactions in the Photocatalytic Reduction of CO_2 : Evidence for Light-Induced Deactivation Processes in Homogeneous Photocatalysis. *ChemCatChem* **2015**, *7* (4), 690–697.

(140) Takeda, H.; Koike, K.; Inoue, H.; Ishitani, O. Development of an Efficient Photocatalytic System for CO_2 Reduction Using Rhenium(I) Complexes Based on Mechanistic Studies. *J. Am. Chem. Soc.* **2008**, *130* (6), 2023–2031.

(141) Gibson, D. H.; Yin, X. Synthesis and Reactions of Fac-Re(dmbpy)$(CO)_3$X (Dmbpy = 4,4’-dimethyl- 2,2’-bipyridyl; X = COOH, COOMe, H, OH, and OCHO). *J. Am.*

Chem. Soc. **1998**, *120* (43), 11200–11201.

(142) Linic, S.; Christopher, P.; Ingram, D. B. Plasmonic-Metal Nanostructures for Efficient Conversion of Solar to Chemical Energy. *Nat. Mater.* **2011**, *10* (12), 911–921.

(143) Tao, A.; Sinsermsuksakul, P.; Yang, P. Polyhedral Silver Nanocrystals with Distinct Scattering Signatures. *Angew. Chemie Int. Ed.* **2006**, *45* (28), 4597–4601.

(144) Wu, H.-J.; Henzie, J.; Lin, W.-C.; Rhodes, C.; Li, Z.; Sartorel, E.; Thorner, J.; Yang, P.; Groves, J. T. Membrane-Protein Binding Measured with Solution-Phase Plasmonic Nanocube Sensors. *Nat. Methods* **2012**, *9* (12), 1189–1191.

(145) Yuan, Y.-P.; Ruan, L.-W.; Barber, J.; Joachim Loo, S. C.; Xue, C. Hetero-Nanostructured Suspended Photocatalysts for Solar-to-Fuel Conversion. *Energy Environ. Sci.* **2014**, *7* (12), 3934–3951.

(146) Bell, A. T. The Impact of Nanoscience on Heterogeneous Catalysis. *Science* **2003**, *299* (5613), 1688–1691.

(147) Cargnello, M.; Doan-Nguyen, V. V. T.; Gordon, T. R.; Diaz, R. E.; Stach, E. A.; Gorte, R. J.; Fornasiero, P.; Murray, C. B. Control of Metal Nanocrystal Size Reveals Metal-Support Interface Role for Ceria Catalysts. *Science* **2013**, *341* (6147), 771–773.

(148) Fu, Q.; Li, W.-X.; Yao, Y.; Liu, H.; Su, H.-Y.; Ma, D.; Gu, X.-K.; Chen, L.; Wang, Z.; Zhang, H.; et al. Interface-Confined Ferrous Centers for Catalytic Oxidation. *Science* **2010**, *328* (5982), 1141–1144.

(149) Comotti, M.; Li, W. C.; Spliethoff, B.; Schüth, F. Support Effect in High Activity Gold Catalysts for CO Oxidation. *J. Am. Chem. Soc.* **2006**, *128* (3), 917–924.

(150) Farmer, J. A.; Campbell, C. T. Ceria Maintains Smaller Metal Catalyst Particles by Strong Metal-Support Bonding. *Science* **2010**, *329* (5994), 933–936.

(151) Schwab, G.-M. Electronics of Supported Catalysts. In *Advances in Catalysis*; 1979; Vol. 27, pp 1–22.

(152) Campbell, C. T.; Sellers, J. R. V. Anchored Metal Nanoparticles: Effects of Support and Size on Their Energy, Sintering Resistance and Reactivity. *Faraday Discuss.* **2013**, *162*, 9.

(153) Liu, J. J. Advanced Electron Microscopy of Metal-Support Interactions in Supported Metal Catalysts. *ChemCatChem* **2011**, *3* (6), 934–948.

(154) Duriez, C.; Henry, C. R.; Chapon, C. Molecular Beam Study of the Chemisorption of CO on Well Shaped Palladium Particles Epitaxially Oriented on MgO(100). *Surf. Sci.* **1991**, *253* (1–3), 190–204.

(155) Henry, C. R. Surface Studies of Supported Model Catalysts. *Surf. Sci. Rep.* **1998**, *31*,

231–325.

(156) James, T. E.; Hemmingson, S. L.; Campbell, C. T. Energy of Supported Metal Catalysts: From Single Atoms to Large Metal Nanoparticles. *ACS Catal.* **2015**, *5* (10), 5673–5678.

(157) Campbell, C. T. The Effect of Size-Dependent Nanoparticle Energetics on Catalyst Sintering. *Science* **2002**, *298* (5594), 811–814.

(158) Wettergren, K.; Schweinberger, F. F.; Deiana, D.; Ridge, C. J.; Crampton, A. S.; Rötzer, M. D.; Hansen, T. W.; Zhdanov, V. P.; Heiz, U.; Langhammer, C. High Sintering Resistance of Size-Selected Platinum Cluster Catalysts by Suppressed Ostwald Ripening. *Nano Lett.* **2014**, *14* (10), 5803–5809.

(159) Johnson, S. L.; Heimann, P. A.; Lindenberg, A. M.; Jeschke, H. O.; Garcia, M. E.; Chang, Z.; Lee, R. W.; Rehr, J. J.; Falcone, R. W. Properties of Liquid Silicon Observed by Time-Resolved X-Ray Absorption Spectroscopy. *Phys. Rev. Lett.* **2003**, *91* (15), 157403.

(160) Farges, F.; Benzerara, K.; Brown, G. E. Chrysocolla Redefined as Spertiniite. *AIP Conf. Proc.* **2007**, *882*, 223–225.

(161) Toupance, T.; Kermarec, M.; Lambert, J.-F. F.; Louis, C. Conditions of Formation of Copper Phyllosilicates in Silica-Supported Copper Catalysts Prepared by Selective Adsorption. *J. Phys. Chem. B* **2002**, *106* (9), 2277–2286.

(162) Fukumi, K.; Chayahara, A.; Kadono, K.; Kageyama, H.; Akai, T.; Mizoguchi, H.; Kitamura, N.; Makihara, M.; Horino, Y.; Fujii, K. Coordination Structures of Implanted Fe, Co, and Ni Ions in Silica Glass by X-Ray Absorption Fine Structure Spectroscopy. *J. Mater. Res.* **2001**, *16* (1), 155–162.

(163) Maurizio, C.; D'Acapito, F.; Benfatto, M.; Mobilio, S.; Cattaruzza, E.; Gonella, F. Local Coordination Geometry around Cu^+ and Cu^{2+} Ions in Silicate Glasses: An X-Ray Absorption near Edge Structure Investigation. *Eur. Phys. J. B* **2000**, *14* (2), 211–216.

(164) van den Oetelaar, L. C. A.; Partridge, A.; Toussaint, S. L. G.; Flipse, C. F. J.; Brongersma, H. H. A Surface Science Study of Model Catalysts. 2. Metal−Support Interactions in Cu/SiO_2 Model Catalysts. *J. Phys. Chem. B* **1998**, *102* (47), 9541–9549.

(165) Liu, P.; Zhao, Y.; Qin, R.; Mo, S.; Chen, G.; Gu, L.; Chevrier, D. M.; Zhang, P.; Guo, Q.; Zang, D.; et al. Photochemical Route for Synthesizing Atomically Dispersed Palladium Catalysts. *Science* **2016**, *352* (6287), 797–800.

(166) Wang, Z.-Q.; Xu, Z.-N.; Peng, S.-Y.; Zhang, M.-J.; Lu, G.; Chen, Q.-S.; Chen, Y.; Guo, G.-C. High-Performance and Long-Lived Cu/SiO_2 Nanocatalyst for CO_2 Hydrogenation. *ACS Catal.* **2015**, *5* (7), 4255–4259.

(167) Gong, J.; Yue, H.; Zhao, Y.; Zhao, S.; Zhao, L.; Lv, J.; Wang, S.; Ma, X. Synthesis

of Ethanol via Syngas on Cu/SiO 2 Catalysts with Balanced Cu^0–Cu^+ Sites. *J. Am. Chem. Soc.* **2012**, *134* (34), 13922–13925.

(168) Manthiram, K.; Beberwyck, B. J.; Alivisatos, A. P. Enhanced Electrochemical Methanation of Carbon Dioxide with a Dispersible Nanoscale Copper Catalyst. *J. Am. Chem. Soc.* **2014**, *136* (38), 13319–13325.

(169) Loiudice, A.; Lobaccaro, P.; Kamali, E. A.; Thao, T.; Huang, B. H.; Ager, J. W.; Buonsanti, R. Tailoring Copper Nanocrystals towards C_2 Products in Electrochemical CO_2 Reduction. *Angew. Chemie Int. Ed.* **2016**, *55* (19), 5789–5792.

(170) Kim, Y.-G.; Javier, A.; Baricuatro, J. H.; Torelli, D.; Cummins, K. D.; Tsang, C. F.; Hemminger, J. C.; Soriaga, M. P. Surface Reconstruction of Pure-Cu Single-Crystal Electrodes under CO-Reduction Potentials in Alkaline Solutions: A Study by Seriatim ECSTM-DEMS. *J. Electroanal. Chem.* **2016**, *780*, 290–295.

(171) Kim, Y.-G.; Javier, A.; Baricuatro, J. H.; Soriaga, M. P. Regulating the Product Distribution of CO Reduction by the Atomic-Level Structural Modification of the Cu Electrode Surface. *Electrocatalysis* **2016**, *7* (5), 391–399.

(172) Eilert, A.; Cavalca, F.; Roberts, F. S.; Osterwalder, J.; Liu, C.; Favaro, M.; Crumlin, E. J.; Ogasawara, H.; Friebel, D.; Pettersson, L. G. M.; et al. Subsurface Oxygen in Oxide-Derived Copper Electrocatalysts for Carbon Dioxide Reduction. *J. Phys. Chem. Lett.* **2017**, *8* (1), 285–290.

(173) Mistry, H.; Varela, A. S.; Bonifacio, C. S.; Zegkinoglou, I.; Sinev, I.; Choi, Y.-W.; Kisslinger, K.; Stach, E. A.; Yang, J. C.; Strasser, P.; et al. Highly Selective Plasma-Activated Copper Catalysts for Carbon Dioxide Reduction to Ethylene. *Nat. Commun.* **2016**, *7*, 12123.

(174) Mistry, H.; Behafarid, F.; Reske, R.; Varela, A. S.; Strasser, P.; Roldan Cuenya, B. Tuning Catalytic Selectivity at the Mesoscale via Interparticle Interactions. *ACS Catal.* **2016**, *6* (2), 1075–1080.

(175) Huang, Y.; Handoko, A. D.; Hirunsit, P.; Yeo, B. S. Electrochemical Reduction of CO_2 Using Copper Single-Crystal Surfaces: Effects of CO* Coverage on the Selective Formation of Ethylene. *ACS Catal.* **2017**, *7* (3), 1749–1756.

(176) Ren, D.; Wong, N. T.; Handoko, A. D.; Huang, Y.; Yeo, B. S. Mechanistic Insights into the Enhanced Activity and Stability of Agglomerated Cu Nanocrystals for the Electrochemical Reduction of Carbon Dioxide to N-Propanol. *J. Phys. Chem. Lett.* **2016**, *7* (1), 20–24.

(177) Li, Y. C.; Zhou, D.; Yan, Z.; Gonçalves, R. H.; Salvatore, D. A.; Berlinguette, C. P.; Mallouk, T. E. Electrolysis of CO_2 to Syngas in Bipolar Membrane-Based Electrochemical Cells. *ACS Energy Lett.* **2016**, *1* (6), 1149–1153.

(178) Vermaas, D. A.; Smith, W. A. Synergistic Electrochemical CO_2 Reduction and Water Oxidation with a Bipolar Membrane. *ACS Energy Lett.* **2016**, *1* (6), 1143–

1148.

Appendix : Publication list

18. Ross, M. B., Li, Y., De Luna, P., Dinh, C. T., **Kim, D.**, Yang, P. & Sargent, E. H. Electrocatalytic Challenges on the Path to Renewable CO_2 Valorization. *Submitted* (2018).

17. Wong, A. B.*, Bekenstein, Y.*, Kang, J., Kley, C. S., **Kim, D.**, Gibson, N. A., Zhang, D., Yu, Y., Leone, S. R., Wang, L., Alivisatos, A. P. & Yang, P. Strongly Quantum Confined Colloidal Cesium Tin Iodide Perovskite Nanoplates: Lessons for Reducing Defect Density and Improving Stability. *Nano Lett.* **18,** 2060–2066 (2018).
doi:10.1021/acs.nanolett.8b00077

16. Becknell, N.*, Son, Y.*, **Kim, D.**, Li, D., Yu, Y., Niu, Z., Lei, T., Sneed, B. T., More, K. L., Markovic, N. M., Stamenkovic, V. R. & Yang, P. Control of Architecture in Rhombic Dodecahedral Pt–Ni Nanoframe Electrocatalysts. *J. Am. Chem. Soc.* **139,** 11678-11681 (2017). doi:10.1021/jacs.7b05584

15. **Kim, D.**, Kley, C. S., Li, Y., & Yang, P. Copper Nanoparticle Ensembles for Selective Electroreduction of CO_2 to C_2-C_3 products. *Proc. Natl. Acad. Sci. U. S. A.* **114,** 10560-10565 (2017). doi:10.1073/pnas.1711493114

14. Ross, M. B., Dinh, C. T., Li, Y., **Kim, D.**, De Luna, P., Sargent, E. H. & Yang, P. Tunable Cu Enrichment Enables Designer Syngas Electrosynthesis from CO_2. *J. Am. Chem. Soc.* **139,** 9359–9363 (2017). doi:10.1021/jacs.7b04892

13. **Kim, D.***, Xie, C.*, Becknell, N., Yu, Y., Karamad, M., Chan, K., Crumlin, E. J., Norskov, J. K. & Yang, P. Electrochemical Activation of CO_2 through Atomic Ordering Transformations of AuCu Nanoparticles. *J. Am. Chem. Soc.* **139,** 8329–8336 (2017).
doi:10.1021/jacs.7b03516

12. Niu, Z.*, Cui, F.*, Yu, Y., Becknell, N., Sun, Y., Khanarian, G., **Kim, D.**, Dou, L., Dehestani, A., Schierle-Arndt, K. & Yang, P. Ultrathin Epitaxial Cu@Au Core–Shell Nanowires for Stable Transparent Conductors. *J. Am. Chem. Soc.* **139,** 7348–7354 (2017).
doi:10.1021/jacs.7b02884

11. **Kim, D.**, Becknell, N., Yu, Y. & Yang, P. Room-Temperature Dynamics of Vanishing Copper Nanoparticles Supported on Silica. *Nano Lett.* **17,** 2732–2737 (2017).
doi:10.1021/acs.nanolett.7b00942

10. Li, Y.*, Cui, F.*, Ross, M. B., **Kim, D.**, Sun, Y. & Yang, P. Structure-Sensitive CO_2 Electroreduction to Hydrocarbons on Ultrathin 5-fold Twinned Copper Nanowires. *Nano Lett.* **17,** 1312–1317 (2017). doi:10.1021/acs.nanolett.6b05287

9. Choi, K. M.*, **Kim, D.***, Rungtaweevoranit, B., Trickett, C. A., Barmanbek, J. T. D.,

Alshammari, A. S., Yang, P. & Yaghi, O. M. Plasmon-Enhanced Photocatalytic CO_2 Conversion within Metal–Organic Frameworks under Visible Light. *J. Am. Chem. Soc.* **139**, 356–362 (2017). doi:10.1021/jacs.6b11027

8. Kong, Q.*, **Kim, D.***, Liu, C., Yu, Y., Su, Y., Li, Y. & Yang, P. Directed Assembly of Nanoparticle Catalysts on Nanowire Photoelectrodes for Photoelectrochemical CO_2 Reduction. *Nano Lett.* **16,** 5675–5680 (2016). doi:10.1021/acs.nanolett.6b02321

7. Niu, Z.*, Becknell, N.*, Yu, Y., **Kim, D.**, Chen, C., Kornienko, N., Somorjai, G. A. & Yang, P. Anisotropic phase segregation and migration of Pt in nanocrystals en route to nanoframe catalysts. *Nat. Mater.* **15,** 1188–1194 (2016). doi:10.1038/nmat4724

6. Cao, Z.*, **Kim, D.***, Hong, D., Yu, Y., Xu, J., Lin, S., Wen, X., Nichols, E. M., Jeong, K., Reimer, J. A., Yang, P. & Chang, C. J. A Molecular Surface Functionalization Approach to Tuning Nanoparticle Electrocatalysts for Carbon Dioxide Reduction. *J. Am. Chem. Soc.* **138,** 8120–8125 (2016). doi:10.1021/jacs.6b02878

5. Kornienko, N.*, Zhao, Y.*, Kley, C. S., Zhu, C., **Kim, D.**, Lin, S., Chang, C. J., Yaghi, O. M. & Yang, P. Metal–Organic Frameworks for Electrocatalytic Reduction of Carbon Dioxide. *J. Am. Chem. Soc.* **137,** 14129–14135 (2015). doi:10.1021/jacs.5b08212

4. Lin, S.*, Diercks, C. S.*, Zhang, Y. B.*, Kornienko, N., Nichols, E. M., Zhao, Y., Paris, A. R., **Kim, D.**, Yang, P., Yaghi, O. M. & Chang, C. J. Covalent organic frameworks comprising cobalt porphyrins for catalytic CO_2 reduction in water. *Science* **349,** 1208–1213 (2015). doi:10.1126/science.aac8343

3. **Kim, D.**, Sakimoto, K. K., Hong, D. & Yang, P. Artificial Photosynthesis for Sustainable Fuel and Chemical Production. *Angew. Chemie Int. Ed.* **54,** 3259–3266 (2015). doi:10.1002/anie.201409116

2. **Kim, D.**, Resasco, J., Yu, Y., Asiri, A. M. & Yang, P. Synergistic geometric and electronic effects for electrochemical reduction of carbon dioxide using gold–copper bimetallic nanoparticles. *Nat. Commun.* **5,** 4948 (2014). doi:10.1038/ncomms5948

1. **Kim, D.**, Yang, S. J., Kim, Y. S., Jung, H. & Park, C. R. Simple and cost-effective reduction of graphite oxide by sulfuric acid. *Carbon* **50,** 3229–3232 (2012). doi:10.1016/j.carbon.2011.11.014